The characterization and carbothermic reduction of furnace dust from the TKZN heavy mineral sands operation

by

Makhale Elia Khesa

Thesis presented in partial fulfilment
of the requirements for the Degree

of

MASTER OF ENGINEERING
(EXTRACTIVE METALLURGICAL ENGINEERING)

in the Faculty of Engineering
at Stellenbosch University

Supervisors

Prof. G. Akdogan, Prof. S.M. Bradshaw

December 2016

Declaration

By submitting this thesis electronically, I declare that the entirety of the work contained therein is my own, original work, that I am the sole author thereof (save to the extent explicitly otherwise stated), that reproduction and publication thereof by Stellenbosch University will not infringe any third party rights and that I have not previously in its entirety or in part submitted it for obtaining any qualification.

Date: December 2016

Abstract

Titaniferous ores serve as a major feedstock for the production of a white titanium dioxide pigment, a titanium metal and several other titanium-based products. Such ores exist mainly as heavy mineral sands. Ilmenite, which is a subset of those ores, is often upgraded to intermediate products namely synthetic rutile and titania slag through the synthetic rutile route and the reductive smelting route respectively.

Like in most mineral sands operations, Tronox KwaZulu Natal Sands (Pty) Ltd recovers and disposes of a furnace dust, which is produced from the reductive smelting route, as a waste material. However, previous investigations have shown that such furnace dust can contain significant amount of titanium-bearing minerals. This study was therefore initiated to better understand the characteristics of this furnace dust and subsequently to investigate the potential of transforming such a metallurgical waste stream into a valuable stream through the production of a titania slag within the context of ilmenite smelting.

The specific objectives of the study were to study the chemical and mineralogical characteristics of the furnace dust that was obtained from Tronox KwaZulu Natal Sands, to simulate the carbothermic reduction process of the furnace dust and to experimentally investigate the potential of producing a titania slag and a metallic iron from the furnace dust.

The characteristics of the furnace dust were examined by several analytical techniques including x-ray fluorescence, x-ray diffraction, microscopy and laser-diffraction size analyses. The observations from the characterization work showed that the furnace dust was rich in the oxides of titanium and iron (49.39wt% TiO_2 and 29.51wt% Fe_2O_3). However, these oxides were associated with significant amount of impurities, with silica being the largest of such impurities.

In order to understand the thermodynamic feasibility of producing a titania slag and a metallic iron from the furnace dust, a series of thermodynamic simulations were performed using FactSage between 1500˚C and 1700˚C and at different carbon additions. The FactSage simulations showed that more than 85wt% of the equivalent titanium dioxide content within the slag could be obtained under relatively high carbon additions and at temperatures between 1650˚C and 1700˚C. However, such strongly reducing conditions favoured a significant

reduction of the oxides of titanium to metallic titanium without significantly reducing the impurity oxides from the slag phase. On the other hand, the degree of iron metallization was found to be above 90wt% at carbon additions that favoured less titanium loss from the slag phase. The simulation work also showed that the extent of reduction of FeO from the slag phase was mainly influenced by the carbon addition, but less influenced by temperature.

An experimental production of a titania slag and a metallic iron was investigated on a laboratory scale, PVT 18/75/350 Carbolite® vertical tube furnace at 1500˚C, 1600˚C and 1650˚C with the reduction times up to 10 minutes. From these experimental reduction tests, the slag samples with the equivalent titanium dioxide content ranging within 70.87-76.87wt% at 1600˚C and 1650˚C were obtained. Such equivalent titanium dioxide content was slightly lower than the 79wt% that was calculated in thermodynamic simulations. The Fe content of the metallic iron samples that were produced ranged within 93.03-97.13wt%. However, a titania slag sample that was produced at 1500˚C for 10 minutes exhibited the equivalent titanium dioxide content of only 65.87wt%. That relatively lower content of the equivalent titanium dioxide was attributed to an insignificant removal of the impurity oxides and further insignificant removal of iron oxide from the slag as the slag was partially molten. The metallic iron sample that was produced at 1500˚C showed the Fe content of 98.47wt%.

The overall experimental reduction tests were in good agreement with the simulation results and both test works evidenced the potential of producing a titania slag and a metallic iron from the furnace dust. The production of both titania slag and metallic iron from this furnace dust demonstrated the potential of such material to supplement the natural titaniferous ores in order to meet the ever-increasing market demands in the white titanium dioxide pigment industry and to substantiate the feedstock into the foundry market.

Opsomming

Titaanhoudende erts dien as ‘n belangrike grondstof vir die vervaardiging van ‘n wit titaandioksied pigment, ‘n titanium metaal en verskeie ander titanium gebaseerde produkte. Hierdie tipe erts kom hoofsaaklik voor as swaar minerale sand. ‘n Onderafdeling van hierdie tipe erts, Ilmeniet, word dikwels opgegradeer tot intermediêre produkte; naamlik sintetiese rutiel en titania slakmeel deur onderskeidelik die sintetiese rutiel en reduktiewe smelting roetes.

Soos in meeste sand mineraal bedrywighede, herwin en verwyder Tronox KwaZulul Natal (Pty) Ltd oond stof, wat geproduseer word van die reduktiewe smelting roete, as ‘n afval materiaal. Vorige ondersoeke het egter getoon dat hierdie oond stof ‘n beduidende hoeveelheid titanium-draende minerale kan bevat. Hierdie studie was dus onderneem om die eienskappe van hierdie oond stof beter te verstaan en om die potentiaal van die transformasie van so ‘n afval stroom na ‘n waardevolle stroom deur middle van die produksie van ‘n titania slakmeel en metaal yster van die oond stof.

Die spesifieke doelwitte van hierdie studie was om die chemiese en mineralogiese eienskappe van die oond stof van Tronox Kwazulu Natal Sands te ondersoek, die karbotermiese reduksie van die oond stof te simuleer en om die potentiaal vir die produksie van ‘n titania slakmeel en metaal yster van die oond stof eksperimenteel te ondersoek.

Die eienskappe van die oond stof is ondersoek deur verskeie analitiese tegnieke, insluitend x-straal-fluoressensie, x-straaldiffraksie, mikroskopie en laser-diffraksie grootte analise. Die waarnemings van die karakterisering werk het getoon dat die oond stof ryk was in die oksiede van titanium en yster (49.39 massa% TiO_2 en 29.51 massa% Fe_2O_3). Alhoewel, onsuiwerhede was geassosieer met hierdie oksiede, met silika as die grootste van die sodanige onsuiwerhede.

Met die oog op die termodinamiese haalbaarheid van die vervaardiging van 'n Titania slag en 'n metaal yster uit die oond stof, is 'n reeks van termodinamiese simulasies uitgevoer met behulp van FactSage tussen 1500 ˚C en 1700˚C asook by verskillende koolstof toevoegings. Die FactSage simulasies het getoon dat meer as 85 massa% van die ekwivalent titaandioksied inhoud binne die slakmeel verkry kan word, onder relatiewe hoë koolstof toevoegings en by temperature

tussen 1650˚C en 1700˚C. Die sterk reduksie toestand het 'n aansienlike vermindering van die oksiede van titanium tot metaal titanium bevoordeel, sonder die reduksie van die onsuiwerhede in die slakmeel. Aan die ander kant, die graad van yster metallisatie was gevind om bo 90 massa% te wees by laer koolstof toevoegings, wat die verlies van titanium in die slakmeel verminder het. Die simulasie werk het ook getoon dat die omvang van 'n verlaging van FeO uit die slag fase hoofsaaklik beïnvloed was deur die koolstof toevoeging maar minder beïnvloed was deur die temperatuur.

Die eksperimentele produksie van ‘n titania slakmeel en yster was onderoek op ‘n laboratorium skaal, PVT 18/75/350 Carbolite® vertikale buisoond, by 1500˚C, 1600˚C en 1650˚C met reduksie tye tot 10 minute. Van hierdie eksperimentele reduksie toetse, was die slakmeel monsters met die wissellende ekwivalente titaandioksied inhoud binne 70.87-76.87 massa% by 1600˚C en 1650˚C gekry. Sulke ekwivalent titaandioksied inhoud was effens laer as die 79 massa% wat bereken is deur die termodinamiese simulasies. Die Fe inhoud van die metaal yster monsters wat geproduseer was het gewissel binne 93.03-97.13 massa%, maar die titania slakmeel monster wat geproduseer was in 1500˚C vir 10 minute het ‘n ekwivalente titaandioksied inhoud van slegs 65.87wt% getoon. Die relatiewe laer inhoud van die ekwivalente titaandioksied is toegeskryf aan die onbeduidende verwydering van die onreinheid oksiede en die onbeduidende afname van ysteroksied, want die slakmeel was slegs gedeeltelik gesmelt. Die metaal yster monster wat geproduseer was by 1500 ˚C het ‘n Fe inhoud van 98.47 massa%.

Die algehele eksperimentele reduksie toetse het ooreengestem met die simulasie resultate en beide toets werke bewys die potensiaal van die vervaardiging van 'n titania slakmeel en 'n metaal yster uit die oond stof. Die produksie van beide titania slakmeel en 'n metaal yster uit hierdie oond stof het die potensiaal gedemonstreer om as aanvulling te dien vir die natuurlike titaanhoudende yster erts, om ten einde die toenemende vereistes van die mark in die wit titaandioksied pigment bedryf te ontmoet en om die roumateriaal in die gietery mark te staaf.

Acknowledgements

I would like to express my greatest gratitude to people who guided, helped and supported me through this study.

- I am indebted to my supervisors Prof. G. Akdogan and Prof. S.M. Bradshaw for their valuable guidance, insights, encouragement and enrichment with knowledge in order to bring this study to completion. Furthermore, I would like to thank Dr. N. Snyders for some insights during the progress of this study.

- Lets'eng Diamonds (Pty) Ltd provided an invaluable financial support while I have been far from home and working hard during my studies. I wish to pass my thankfulness to the company for risking such large amounts of money to finance my studies.

- Tronox KwaZulu Natal Sands (Pty) Ltd made a helpful contribution in this study by providing the bulk feed samples. I am grateful to such company.

- I am further grateful to the facility managers and personnel of the laboratories and pilot-scale plants at the Stellenbosch University for ensuring the availability of resources and providing assistance during commissioning and operation of several pieces of equipment.

- The family members, close relatives and friends never ceased to encourage and to give me motivation as the going went tough. I am very thankful for all the words of encouragement they provided.

Above all, I would like to thank The Almighty for providing health, strength, perseverance and dedication through this challenging study. Without Him, much could had not been done.

Table of contents

List of Tables

List of Figures

List of Abbreviations

AAN	Average atomic number
BSE	Backscattered electrons
DC	Direct current
DIM	Degree of iron metallization
EAF	Electric arc furnace
EDS	Energy dispersive spectroscopy
FACT	Facility for the Analysis of Chemical Thermodynamics
HMC	Heavy mineral concentrate
L.O.I.	Loss on ignition
N.I.S.T.	National Institute of Standards and Technology
PSB	Pseudobrookite
PSD	Particle size distribution
ROM	Run-of-mine
SEM	Scanning electron microscopy
STDEV	Sample standard deviation
TEM	Transmission electron microscopy
TGA	Thermogravimetric analysis
TKZNS	Tronox KwaZulu Natal Sands
UGS	Upgraded slag

XRD	X-ray diffraction
XRF	X-ray fluorescence
$TiO_2{}^{eq}$	Equivalent titanium dioxide

1. Introduction

1.1. Titaniferous ores

1.1.1. Occurrence

Titanium is the ninth most abundant element among the elements that are found within the earth's crust (Pesl, 1997; Samal et al., 2010; Stadler, 2012). Within the earth's crust, titanium is bound with other elements to form titaniferous minerals and some of those minerals are presented in Table 1.1. These minerals occur mainly as heavy mineral sands in the placer deposits (Force, 1991). However, in some cases such minerals can occur as hardrock deposits (Pesl, 1997; Zietsman, 2004). In the hardrock deposits, ilmenite is dominant while other minerals are very scarce or completely absent (Zietsman, 2004).

Table 1.1: Some titaniferous minerals and their properties (Force, 1991; Koroznikova et al., 2008; Walklate and Jeram, 2007; Gazquez et al., 2014).

Ore body	Mineral sand	Nominal formula	Specific gravity	TiO_2 (wt%)	Crystal form
Placer or hardrock deposits	Ilmenite	$FeTiO_3$ or $FeO.TiO_2$	4.70 - 4.79	35-65	Hexagonal
	Rutile	TiO_2	4.20 - 4.30	>95	tetragonal
	Leucoxene	$Fe_2O_3.nTiO_2$	3.90 - 4.20	70-90	-
	Anatase	TiO_2	3.80 - 3.90	>90	Tetragonal
	Brookite	TiO_2	3.80 - 4.00	>90	Orthorhombic
	Perovskite	$CaTiO_3$	4.00	58	Monoclinic
	Pyrophanite	$MnTiO_3$	4.5-4.53	53	Trigonal
	Armalcolite	$(Mg^{2+}, Fe^{2+})Ti_2O_5$	4.60	71-76	Orthorhombic
	Sphene	$CaTiSiO_5$	3.40 - 3.60	41	Monoclinic

Among the titaniferous minerals that are presented in Table 1.1, only ilmenite, rutile and leucoxene can guarantee an economical exploitation because of their relatively higher content of titanium dioxide, lesser inclusion of impure elements and high abundance (Force, 1991; Pesl, 1997). Rutile and leucoxene are superior to ilmenite in terms of the titanium dioxide content, but ilmenite is found to be more abundant than any of those titaniferous minerals. It has been shown that rutile reserves are only one tenth as abundant as the reserves of ilmenite (Sunde, 2012). Such relatively high abundance of ilmenite explains why ilmenite serves as the major feedstock for the

production of titanium end-products (Elstad et al., 2007).

1.1.2. Mining and ore-dressing

The titaniferous ores are mined by invariably three methods namely hydraulic mining, dredging and classical mechanical methods (Pesl, 1997; Zietsman, 2004; Stadler, 2012). The hydraulic mining is applied to sand deposits that exist in dry land. The deposit face is washed out with high pressure water after which the slurried ore is collected for further processing. Dredging involves collection of the mineral sands from deposits that are underwater. Finally, the classical mechanical methods that involve blasting and excavation are used in the case of hardrock deposits or when a sand deposit co-exist with a hardrock deposit (Pesl, 1997; Zietsman, 2004). This last method is often followed by size reduction stages.

The run-of-mine (ROM) ore (including the ore from the hardrock deposits after size reduction) is concentrated in the wet gravity circuits that can consist of only or a combination of spiral concentrators, pinched sluices or floatation cells. A product from these circuits is made up of two streams namely a heavy minerals concentrate (HMC) and tailings. The tailings stream, which consists of mainly sand and slimes, is often used as a backfill to rehabilitate the mined-out areas while the HMC is processed further to separate the individual minerals. This separation is accomplished by an integration of gravity concentration methods, electrostatic and magnetic separation techniques (Pesl, 1997; Zietsman, 2004).

After separation of individual minerals, leucoxene, rutile and zircon are often sold to the end-users while ilmenite is processed further (Gous, 2006; Stadler, 2012). Depending on the levels of gangue minerals in such ilmenite stream, this stream can be further enriched to lower such impurity levels. An enriched ilmenite stream is subsequently processed to high titania intermediates (Zietsman, 2004).

1.1.3. Upgrading of titaniferous ores to high titania intermediates

An upgrading of ilmenite to high titania intermediates is of crucial importance because it minimizes volumes of reagents that would be used and waste that would otherwise be generated in the downstream processes if such mineral was directly used as a feedstock. An enriched ilmenite stream is often upgraded to high titania intermediates by two process routes namely a

synthetic rutile route and a reductive smelting route (Pesl, 1997; Pesl and Eric, 1999; Pistorius, 2008). In 2005, these routes contributed almost equal amounts of high titania intermediates into the world productions (Elstad et al., 2007). However, the reductive smelting route is currently being favoured over the synthetic rutile route because of some reasons that are highlighted in the subsequent paragraphs.

The synthetic rutile route includes a number of processes such as a direct chlorination and a solid-state thermal reduction that is carried out at around 1200˚C (Brent, 1987; Pesl and Eric, 1999; Pesl and Eric, 2002; Gazquez et al., 2014). A product from such route contains a titanium dioxide content in the orders of 90wt% or more. The direct chlorination process, which is currently getting obsolete because of the large quantities of waste generated, involves direct reaction of ilmenite with chlorine to produce synthetic rutile and ferric chloride (Brent, 1987). The solid-state thermal reduction, on the other hand, involves reduction of solid ilmenite with carbon, carbon monoxide or natural gas to produce synthetic rutile and sulphates or chlorides of iron. The solid-state thermal reduction is widely achieved through the Becher and the Murso processes, which are based on the reactions that are provided in Equations 1.1 to 1.3 (Pesl, 1997; Welham and Williams, 1999; Sunde, 2012). However, the resulting iron is often removed as a waste through acid leaching processes.

$$FeTiO_3(s) + C(s) \rightleftharpoons Fe(s) + TiO_2(s) + CO(g) \quad \text{..... (1.1)}$$

$$FeTiO_3(s) + CO(g) \rightleftharpoons Fe(s) + TiO_2(s) + CO_2(g) \quad \text{..... (1.2)}$$

$$Fe_2O_3(s) + 3CO(g) \rightleftharpoons 2Fe(s) + 3CO_2(g) \quad \text{..... (1.3)}$$

The generation of large quantities of iron in the form of chlorides and sulphates from the synthetic rutile route does not only impose serious challenges during disposal, but it also causes loss of the valuable iron. As such, most of the high titania intermediates producers are gradually moving and adopting the reductive smelting route (Brent, 1987; Samal et al., 2010).

The reductive smelting route is carried out at 1600-1700˚C where ilmenite (melting point ≈ 1397˚C) titania slag (melting point ≈ 1600) and metallic iron (melting point ≈ 1500˚C) are fully in the molten form (Pesl, 1997; Pesl and Eric, 1999; Zietsman, 2004). This process involves reduction of ilmenite with anthracite in an electric arc furnace (EAF) to produce a titania slag as

a primary product and a metallic iron as a secondary product (Brent, 1987; Pesl and Eric, 2002; Pistorius and Coetzee, 2003). A slag is a liquid phase that consists of mainly metallic oxides and silicates (Woollacott and Eric, 1994) and a titania slag with an equivalent titanium dioxide ($TiO_2{}^{eq}$) content of 85wt% or more is highly desirable (Pistorius, 2002; Pistorius and Coetzee, 2003). The $TiO_2{}^{eq}$ content is defined here as the amount of total titanium, at different oxidation states within the slag, expressed as an equivalent of TiO_2 (Pistorius, 2002).

In addition to the titania slag and metallic iron, a carbon monoxide dominant off-gas is produced as a by-product. This off-gas stream is laden with very fine particles whose concentration can lie within 50-200 g/Nm^3 (Gottschling, 2009). A source of these fine particles can be fine feed that by-passed the furnace and oxidic together with metallic fumes from a reduction process. These fine particles form the basis of this current study and hereafter they will be referred to as furnace dust. Currently, there is limited literature regarding this furnace dust, but an available literature is presented in section 2.2.

An integration of both the solid-state thermal reduction and the reductive smelting routes has been observed to be advantageous because the energy consumptions in the smelting sections are significantly lowered (Samal et al., 2010). The more than 70% degree of iron metallization (DIM), which is defined in Equation 1.4 after Park et al. (2002), can be achieved during the solid-state thermal reduction (Zietsman, 2004; Sunde, 2012). Such pre-reduction stage can be followed by complete reduction in the smelting sections. Tizir Titanium and Iron in Tyssedal has successfully implemented such integrated processing route (Sunde, 2012).

$$\text{DIM} = \frac{Amount\ of\ metallic\ iron\ after\ reduction}{Amount\ of\ total\ iron\ after\ reduction} \quad \ldots\ldots\ldots (1.4)$$

1.2. End use of titaniferous materials

A large fraction of titanium that is present within the earth's crust is finally used in the pigment industry for the production of a white titanium dioxide pigment. Pesl (1997) and Sunde (2012) showed that almost 90% of such titanium is used for the production of the titanium dioxide pigment while a barely 10% is used for the production of metallic titanium. The white titanium dioxide pigment is produced through two processes namely the chloride and the sulphate processes. A feedstock to those pigment-producing processes can include rutile or its

polymorphs, leucoxene and high titania intermediates (synthetic rutile and titania slag).

In the chloride process, the raw material is reacted with gaseous chlorine and coke in a fluidized bed reactor at 900˚C to form gaseous chloride species including titanium tetrachloride ($TiCl_4$) (Zietsman, 2004; Cong et al., 2006; Gazquez et al., 2014). The gaseous species are subsequently separated by selective rectification after which the pure $TiCl_4$ is processed further to produce a titanium dioxide pigment and a titanium metal (Pesl, 1997; Zietsman, 2004; Cong et al., 2006; Gazquez et al., 2014).

This process requires the feedstock that contains as minimum impurities as possible. A typical composition of titania slags that serve as a feedstock to this process is summarised in Table 1.2. The amount of CaO and MgO are strictly controlled in such slags because the chlorides of calcium and magnesium have higher boiling points than the typical operating temperature that is

Table 1.2: Specifications of titania slags that serve as a feedstock to the chloride process (Pesl, 1997; Pistorius, 2008).

Species	$TiO_2{}^{eq}$	Ti_2O_3	FeO	SiO_2	Al_2O_3	CaO	MgO	MnO	Cr_2O_3	V_2O_5
Abundance (wt%)	≥85.00	<35.00	<12.00	<4.00	<2.00	<0.25	<1.20	<2.00	<0.25	<0.60

employed in the process. Silica is also unreactive during the chloridization process. These chlorides together with significant amount of silica accumulate in the reactor thereby reducing the chloridization efficiency (Pesl, 1997; Steenkamp, 2003; Cong et al., 2006; Gazquez et al., 2014). The set upper limit for the Ti_2O_3 is to control the heat of reaction that is evolved from the oxidation of this species to a tetravalent titanium (Pistorius, 2002). The excessively evolved heat from such oxidation is often associated with destabilization of the chloridization process.

In the sulphate process, the feedstock is reacted with a concentrated sulphuric acid. The chemical reaction results in the formation of a titanyl sulphate ($TiOSO_4$), ferrous sulphate heptahydrate (copperas) and other insoluble materials (Chernet, 1999; Zietsman, 2004; Gazquez et al., 2014). The titanyl sulphate is processed further to produce a titanium dioxide pigment while copperas and other insoluble solids are removed. The sulphate process can treat low-grade titania slags (lower than 85wt% TiO_2^{eq}), but large quantities of waste materials that require a proper

management are generated (Lasheen, 2008; Dong et al., 2012). It is on this account that much attention is currently being focused towards the more environmentally friendly chloride process (Samal et al., 2010; Dong et al., 2012).

The white titanium dioxide pigment finds wide applications in fabrics, paints, paper and plastics, inks, pharmaceutics and food industry (Cyr et al., 2000; Gazquez et al., 2014). This is because of the high refractive index of this pigment that imparts good brilliance to the end-products. Furthermore, the pigment is inherently benign and this makes it to stand out among other pigments. Apart from use in the production of a white titanium dioxide pigment, a small fraction of such titanium dioxide can also be used in the manufacture of welding rods (Pesl, 1997). As a metal, titanium is widely used in applications that require high resistance to corrosion and high strength-to-weight ratio such as in desalination systems and aircraft industry.

1.3. Context of the research statement

1.3.1. Background of the study

The commercial ilmenite smelting operations in the Republic of South Africa are Richards Bay Minerals in KwaZulu Natal, Namakwa Sands in Western Cape and Tronox KwaZulu Natal Sands (TKZNS) in KwaZulu Natal (Pistorius and Coetzee, 2003; Pistorius, 2008). This present study is focused on the TKZNS operations.

At its inception in the year 2001, the KwaZulu Natal Sands operations were run by ISCOR Ltd and Ticor Ltd under the name Ticor SA. Later in 2005, the KwaZulu Natal Sands operations were acquired by the Exxaro Resources Ltd. It was not later than 2012 when the Exxaro Resources Ltd amalgamated with the Tronox Ltd to form Tronox KwaZulu Natal Sands (Kotźe et al., 2006; Tronox, 2011).

The TKZNS mines the mineral sands at a Hillendale mine using a hydraulic mining method. The ROM ore is processed in the primary wet plant that is located close to the mine to produce the HMC. This HMC is separated into individual minerals within the central processing complex that is located just outside Empangeni (Stadler, 2012). Such central processing complex is depicted in Figure 1.1. Zircon, rutile and leucoxene are sold to the market while ilmenite is processed further for an ultimate production of a titania slag and a metallic iron.

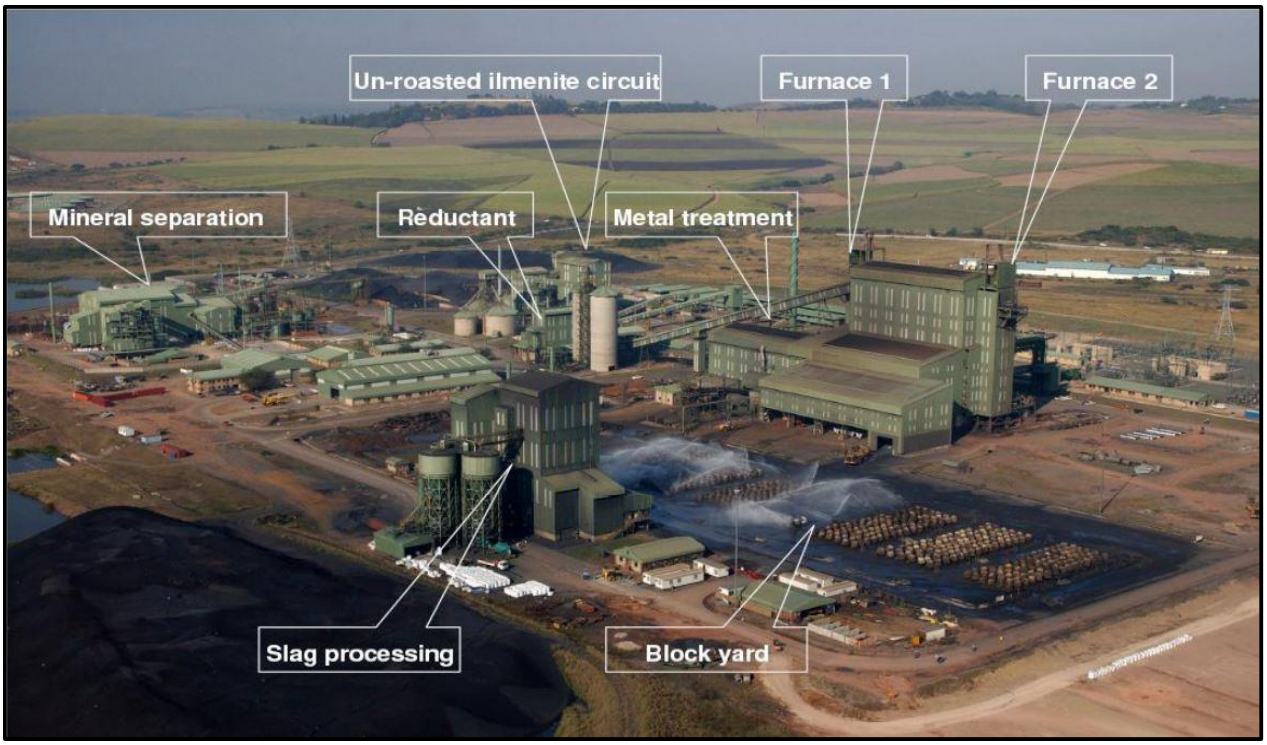

Figure 1.1: The TKZNS central processing complex that is located outside Empangeni (Stadler, 2012).

A titania slag that is produced from the two 36 MW direct current (DC) arc furnaces is cooled, crushed and classified to produce the finer (typically 75-106 μm), sulphatable fraction and the coarser (typically 106-850 μm), chloridizable fraction prior to sale to the pigment industry (Bessinger et al., 2007). The metallic iron, which is produced along with the titania slag, is further treated in the metal treatment plant prior to sale to the foundry market (Gous, 2006; Kotźe et al., 2006; Stadler, 2012).

The furnace dust that is generated from the two furnaces is collected and fed into the Theisen disintegrator off-gas cleaning plant (Gottschling, 2009; Rughubir and Bessinger, 2007). This gas cleaning system is specified to lower the solids loading within the off-gas down to below 20 mg/Nm^3, which is well below the set value of 50 mg/Nm^3 according to the South African Air Quality Act, Act 39 of 2004 (Gottschling, 2009; Schubert and Gottschling, 2011).

In this off-gas cleaning plant, the hot furnace off-gas is cooled and wet-scrubbed in multiple

stages to recover the furnace dust. A resultant slurry of the furnace dust and water is further concentrated in a thickener to about 50wt% solids. These concentrated solids are collected at the thickener underflow and they are disposed of as a waste material. It is at this thickener underflow where a bulk furnace dust sample was collected for an experimental work in this current study.

1.3.2. Research statement

A furnace dust from the TKZNS operation, and many other ilmenite smelting operations, is currently considered as a zero-value material that is disposed of in landfills or mined-out areas. However, a previous study on this furnace dust (Rughubir and Bessinger, 2007) and the findings from other similar studies (Cyr et al., 2000; Kudryavskii, 2004) showed that such furnace dust could contain a significant amount of the oxides of titanium and iron.

The currently diminishing good-grade ores will eventually impel towards reliance on waste materials such as this furnace dust in order to meet the ever-increasing market demands. Furthermore, the recent and currently emerging stringent environmental regulations (Habashi, 2012) compel the chemical and mineral processing industry to optimize an effective utilization of the waste streams. The loss of this furnace dust as a waste material may therefore not only cause the loss of the valuable oxides of titanium and iron, but also it may impose a burden of managing such a metallurgical waste stream in the long run.

This present study was therefore initiated to better understand the characteristics of this furnace dust and to investigate the potential of transforming such a metallurgical waste stream into a valuable stream through the production of a titania slag within the context of ilmenite smelting.

1.3.3. Research objectives

The specific objectives of this present study are:

(i) To investigate the chemical and mineralogical characteristics of the furnace dust.

(ii) To simulate the carbothermic reduction process of the furnace dust.

(iii) To experimentally investigate the potential of producing a titania slag and a metallic iron from the furnace dust.

1.3.4. Research limitations

The mineral phases that were present within the furnace dust might be of synthetic nature, but a nomenclature of natural minerals was used throughout this study. It would be of interest to investigate the possible production of an upgraded slag from the resultant slag samples, but such investigation was beyond the scope of the current study.

1.4. Outline of the thesis

The opening chapter of this thesis is aimed at providing an overall background of the heavy mineral sands industry. The mining and beneficiation of mineral sands are highlighted after which the process routes for production of high titania intermediates are provided. The end-use of the titaniferous materials is also provided. The chapter finally provides the research statement together with the specific objectives of the study.

The second chapter focuses on the available literature that is pertinent to the production of high titania slags. The factors that influence the products chemistry and an equilibrium within the slag-metal phase are further reviewed. The chapter finally provides an available body of knowledge that is pertinent to the furnace dust.

The third chapter provides sampling and preparation of materials for the subsequent experimental test work. The description of equipment and procedures that were used and carried out during experimentation are further provided.

The fourth chapter focuses on the results that were generated during the experimentation and the discussion of such results. The results are compared and contrasted with the currently existing body of knowledge and an implication of such results is provided. The fifth chapter finally states the conclusions that were drawn from the observed results. The recommendations for future work are further highlighted in that fifth chapter.

2. Literature review

2.1. Production of titania slags

2.1.1. General consideration

Smelting is a pyrometallurgical process that involves melting of a furnace charge after which the components within the melt are chemically separated into the slag and metallic or matte phases. In most smelting processes, a metallic phase is regarded as the major product while a slag phase is regarded as a discard. Slags often act as sinks for impurities and their compositions are carefully controlled by fluxes (typically silica, calcium oxide or alumina) in order to maximize their capacity to collect such impurities (Woollacott and Eric, 1994; Pesl, 1997). Basicity of slags is an important parameter that emanates from the composition and it is a measure of a ratio of the basic oxides (CaO and MgO) to acidic and amphoteric oxides (SiO_2 and Al_2O_3) (Woollacott and Eric, 1994; Galgali et al., 1998; Muller and Erwee, 2011). The higher the basicity, the higher the capacity to accommodate the impurities and the easier to tap a slag from the furnace (Pesl, 1997; Muller and Erwee, 2011). However, the high basicity sometimes results in the formation of solids within a slag and this may require an operating temperature to be relatively higher in order to keep such solids in a liquid state (Muller and Erwee, 2011).

Titania slags are produced mainly from ilmenite and such slags are considered as the main products while a metallic phase is considered as the secondary product (Brent, 1987; Pesl, 1997; Pistorius and Coetzee, 2003). The conventional use of fluxes is not employed during the production of titania slags (Pistorius and Coetzee, 2003). Such fluxes would otherwise increase the impurity content of the titania slags thereby rendering the process counterproductive.

The important carbothermic reduction reactions that take place during an upgrading of ilmenite to high titania slags involve reduction of iron oxides and partial reduction of tetravalent titanium to trivalent titanium to produce a titania slag and a liquid iron at 1600-1700˚C (Pesl, 1997; Zietsman, 2004). These reactions are highlighted in Equations 2.1 and 2.2 and an overall reduction reaction is further provided in Equation 2.3 (Pesl and Eric, 2002; Pistorius, 2002). The reduction of iron oxide is found to proceed faster than the reduction of tetravalent titanium (Zietsman and Pistorius, 2004).

$$FeO(\text{l}) + C(\text{s}) \rightleftharpoons Fe(\text{l}) + CO(\text{g}) \quad \ldots\ldots\ldots\ldots\ldots\ldots (2.1)$$

$$2TiO_2(\text{l}) + C(\text{s}) \rightleftharpoons Ti_2O_3(\text{l}) + CO(\text{g}) \quad \ldots\ldots\ldots\ldots (2.2)$$

$$FeO(\text{l}) + Ti_2O_3(\text{l}) \rightleftharpoons Fe(\text{l}) + 2TiO_2(\text{l}) \ldots\ldots\ldots\ldots (2.3)$$

Within the slag phase, there are other reactions that involve carbothermic reduction of the impurity oxides and reaction of such impurity oxides with one another together with the oxides of titanium and iron. Those other reactions are discussed later in this report. The impurity oxides are defined as any other oxides than the oxides of titanium and iron and they typically range within 3-5wt% in such titania slags (Pesl, 1997; Pistorius, 2008).

The titania slags solidify mainly as a pseudobrookite (PSB) or karrooite phase, which is characterised by the M_3O_5 stoichiometric composition. The cationic part of this phase is represented by M and this can include Fe^{2+}, $Mn^{2+}$and Mg^{2+}, Ti (both Ti^{3+} and Ti^{4+}), Al^{3+}, Cr^{3+} and V^{3+} depending on the impurities that constitute a furnace charge. The distribution of the cations within this structure follows that one divalent ion is associated with two tetravalent titanium ions $[M^{2+}(Ti^{4+})_2O_5]$ and two trivalent ions are associated with one tetravalent titanium ion $[(M^{3+})_2Ti^{4+}O_5]$ (Pistorius, 2002; Pistorius and Coetzee, 2003; Pistorius, 2008).

2.1.2. Factors affecting the production of titania slags

The reductant-to-ore ratio, temperature, arc length (when the open-arc configuration is used), feed particle size and reduction time are often carefully manipulated for the betterment of products' chemistry, recovery and stable operation of the process (Brent, 1987; Pesl and Eric, 2002; Gous, 2006).

The effects of the reductant-to-ore ratio and temperature on the composition of the titania slags and metallic iron were intensively studied by Pesl and Eric (2002). Those authors (Pesl and Eric, 2002) found that the extent of reduction is mainly determined by the reductant-to-ore ratio, but with less influence of temperature. The optimum amount of a reductant was found to lie between half of the stoichiometric amount and the stoichiometric amount according to the chemical reactions in Equations 2.1 and 2.2 (Pesl and Eric, 2002). This explains why most of the industrial ilmenite smelters are operated at 127-150 kg of anthracite per 1000 kg of ilmenite (Pesl and Eric, 2002; Thyse et al., 2007).

An increase of the amount of a reductant to more than the stoichiometric amount drastically enhances the reducing conditions. Such strongly reducing conditions cause a gradual disappearance of the titanium oxides, which corresponds to the formation of titanium carbides and oxycarbides. An ultimate product under such strongly reducing conditions is an elemental titanium (Pesl and Eric, 2002). Concurrently, a liquidus temperature of a slag phase increases. This in turn requires the operating temperature to be significantly high (Pesl and Eric, 2002).

Therefore, the amount of a reductant cannot be varied independently over a wide range without destabilizing the operation. The reductant input is often varied concurrently with the energy input at an approximate ratio of 1 kg of a reductant per 5 kWh (Pistorius, 2003; Pistorius, 2008). The possible instability when energy is more than the required ratio is the dissolution of a freeze lining and hence a rapid wear of the furnace walls (Pistorius, 2004). On the other hand, if the energy input is lower than the required ratio, the slag temperature falls to below such slag's liquidus temperature thereby resulting into the undesirable foaming or frothing incidents (Pistorius, 2003; Fourie et al., 2005; Pistorius, 2008).

The operating temperature not only plays a significant role in keeping the furnace charge in the molten state, but it also determines the thermodynamic feasibility of the carbothermic reduction reactions. The lower limit of temperature (1600ºC) ensures that the furnace charge is in the molten state while the upper limit (1700˚C) ensures that the process is more economical. When the operations are pursued at above 1700˚C, the wear of the refractory linings becomes very heavy and this translates to high costs of operating the process (Pesl, 1997). Even though temperature has been found to have an insignificant influence on the extent of reduction between 1600˚C and 1700˚C (Pesl and Eric, 2002), a positive change of this process variable largely increases the extent of reduction when the thermal reduction is carried out between 1200˚C and 1500˚C (Francis and El-Midany, 2008; Gou et al., 2015).

The recoveries of both iron and titanium and an overall efficiency of upgrading titania slags are further dependent on the particle size of the furnace charge. Because of their high specific gravity, ilmenite feed particles are not easily entrained into the off-gas stream. However, anthracite is characterized by low specific gravity (1.3-1.4) and its fine particles are prone to entrainment into such off-gas stream. Brent (1987) showed that the reductive effectiveness of

anthracite with a particle size below 1.68 mm is significantly low due to an entrainment of such particles into the off-gas stream. According to Brent (1987), the acceptable anthracite size range is 2.00-4.76 mm, with the upper limit being attributed to a slow rate of reaction of larger reductant particles.

The reduction time of slags in the furnace is also crucial because it allows both the reaction and phase equilibria to be achieved. In ilmenite smelting, there is currently lack of the reaction kinetics data (Pistorius, 2002; Zietsman and Pistorius, 2004) that can be used to determine the required reduction times. However, the reduction times of 60 minutes to 95 minutes are found to produce titania slags of satisfactory properties to serve as a feedstock to the downstream chloride processes (Brent, 1987). Some authors (Elstad et al., 2007; Seim and Kolbeinsen, 2009) investigated the smelting process at reduction times ranging from 15 minutes to 30 minutes and the high titania slags were also obtained. However, a significant fraction of an unreacted furnace charge was identified (Seim and Kolbeinsen, 2009). Generally, the extent of reduction in the production of titania slags has been found to increase with an increase in reduction time (Brent, 1987).

2.1.3. Equilibrium characteristics of the system

There are number of metal or metalloid oxides, mineral phases and elements that are partitioned between the slag and metallic phases within the titania slag-metallic iron system. The phase equilibria within such system has been observed to occur after approximately six hours of reduction (Pesl and Eric, 1999; Pesl and Eric, 2002; Francis and El-Midany, 2008), but in industrial processes such equilibria is hardly achieved, possibly due to the production throughput constraints. An understanding of the distribution of these different oxides, mineral phases and elements within the slag-metal system is therefore of utmost importance for an enhancement of the products quality.

The reaction in Equation 2.2 results in the formation of reduced rutile species within titania slags and these species are referred to as Magneli phases. These phases exist between the TiO_2 and an anosovite phase (Ti_3O_5) with a general formula Ti_nO_{2n-1} for n = 4 to 10 (Pesl and Eric, 1999; Pistorius and Coetzee, 2003). The other mineral phases within the titania slags emerge because of the interaction of the impurity oxides with one another and the oxides of both iron and

titanium at such high operating temperatures.

Pesl (1997) and Pesl and Eric (1999) generated data for the phase equilibria within the $FeO - TiO_2 - Ti_2O_3$ system and the findings from those authors (Pesl, 1997; Pesl and Eric, 1999) are illustrated in Figure 2.1. It is seen from Figure 2.1 that most Magneli phases except the Ti_8O_{15} (M8) are not in equilibrium with the liquid titania slag, but such phases are equilibrated among themselves and the M_3O_5 (ss) second solid phase towards the trivalent titanium-rich side. Furthermore, these Magneli phases occur on the more iron-deficient side of the composition

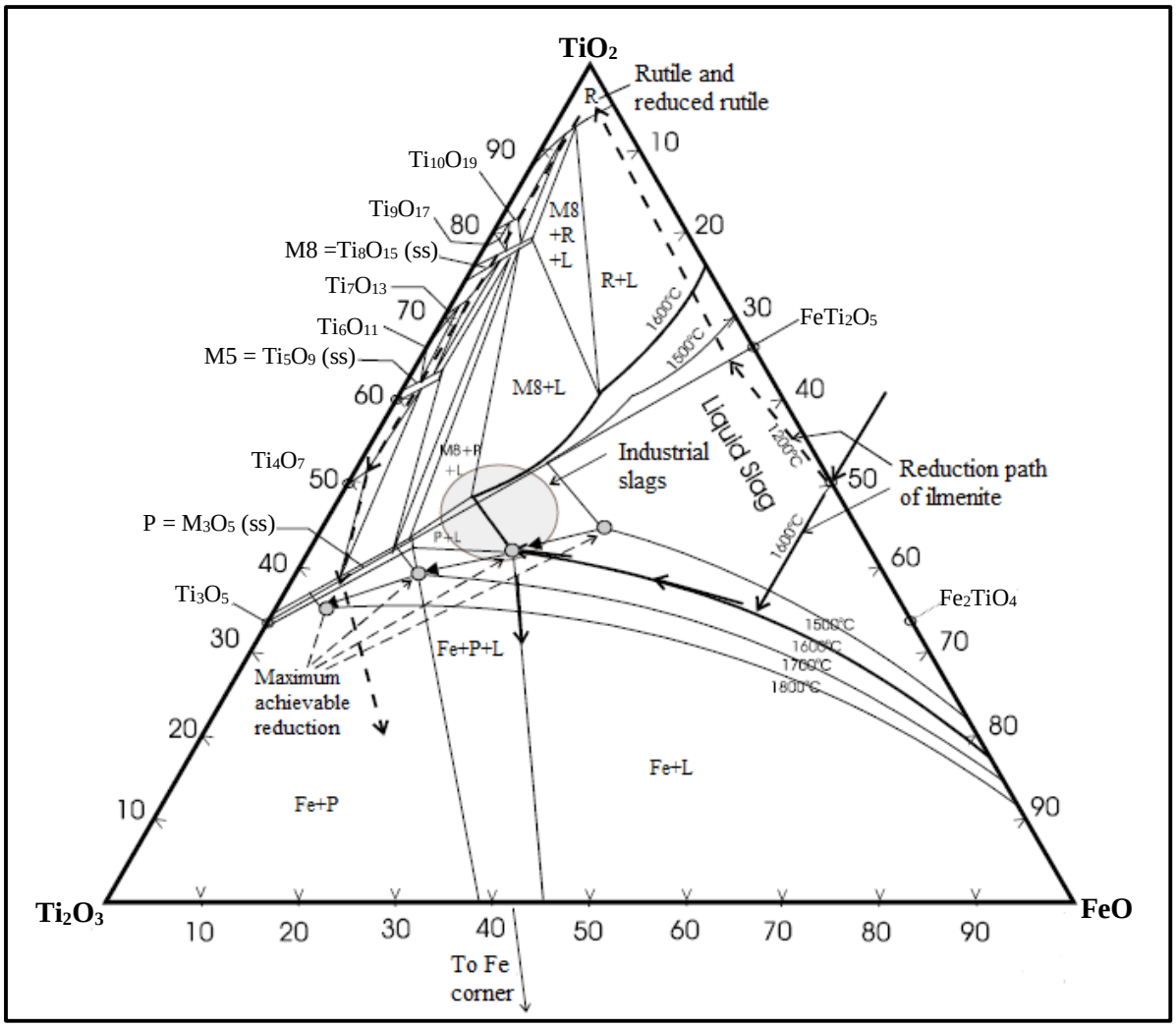

Figure 2.1: The phase relationships within the $FeO - TiO_2 - Ti_2O_3$ ternary system. The composition is in mole percent (Pesl, 1997; Pesl and Eric, 2002). Figure reused with permission of Elsevier and Copyright Clearance Center.

triangle than the industrial slags. These phenomena may provide an explanation to why the solidified industrial titania slags hardly contain such Magneli phases but such slags can contain some rutile phases (Pistorius, 2002; Pistorius and Coetzee, 2003; Pistorius, 2004; Zietsman, 2004).

Further observations from Figure 2.1 show that the liquid slag-metallic iron equilibrium boundary follows a curved line that approaches a double saturation point with the PSB phase (P) at a lower content of iron and close to the M_3O_5 stoichiometric composition. It is also observed that the liquid slag-rutile/Magneli phases equilibrium boundaries approach the double saturation point with the PSB phase close to the M_3O_5 stoichiometric composition. The compositions of industrial slags also lie close to these double saturation points and this can highlight the propensity of titania slags to solidify mainly as the M_3O_5 stoichiometric composition.

A mechanism behind the tendency of titania slags to solidify mainly as the PSB phase was first addressed by Pistorius and Coetzee (2003). The authors (Pistorius and Coetzee, 2003) proved that titania slags, which are produced from smelters that are operated without a freeze lining, tend to deviate from the M_3O_5 stoichiometric composition while slags that are obtained from the smelters with the freeze lining are confined to this stoichiometric composition. This led to a conclusion that the prevalence of the PSB phase in the solidified titania slags is solely due to the eutectic solidification equilibrium of the liquid slag with the freeze lining (Pistorius and Coetzee, 2003; Pistorius, 2003).

However, Zietsman and Pistorius (2004) proposed a mechanism that involves transient solidification and re-melting of the titania slags at the slag-metal interface. Such transient solidification and re-melting is possible because the metallic phase is almost 150˚C cooler than the liquid slag (Pistorius and Coetzee, 2003; Zietsman and Pistorius, 2004). This solidification of titania slags at the metal-slag interface further provided an explanation to the reported slow rate of metal transfer into the metallic phase (Pistorius et al., 2011). Solidification of titania slags is associated with decomposition of such slags due to an interaction of trivalent titanium and divalent iron according to the reaction in Equation 2.3 (Pesl and Eric, 1999; Bessinger et al., 2001; Pistorius and Coetzee, 2003; Zietsman and Pistorius, 2004). At the metal-slag interface, the slags therefore eject iron and become richer in TiO_2. This ultimately shifts their composition

close to the M_3O_5 stoichiometry. A combination of this transient solidification, which is followed by re-melting of the slag phase and the eutectic solidification equilibrium with the freeze lining was therefore found to explain the propensity of the slags to solidify mainly as the PSB phase (Zietsman and Pistorius, 2004; Pistorius, 2008).

The effect of temperature on increasing the stability region of the liquid slag is further observed in Figure 2.1. This observation is in mutual agreement with the previously highlighted effect of integrating energy input with the reductant-to-ore ratio. The amount of FeO in a titania slag, which is controlled by the amount of a reductant added, plays a very important role because of the fluxing effect of FeO (Pistorius and Coetzee, 2003). For this reason, the maximum achievable ${TiO_2}^{eq}$ content is only feasible at higher temperatures where the slag remains in the liquid state throughout a wide composition range (cf. Figure 2.1).

In addition to existing as FeO, iron can also exist within the titania slags as an ilmenite phase (Pistorius and Coetzee, 2003). For this reason, Pistorius and Coetzee (2003) described the compositions of titania slags within the $FeTiO_3 - TiO_2 - Ti_2O_3$ ternary system, which is illustrated in Figure 2.2.

Within this ternary system, the compositions of titania slags are predicted to lie along the eutectic groove, which is defined as an equilibrium boundary between the rutile phase and the PSB phase from point **d** to the TiO_2-Ti_2O_3 binary join (Pistorius and Coetzee, 2003; Pistorius, 2003; Pistorius, 2008). This eutectic groove is basically a set of minimum melting points (solidus) of the slag as a function of the content of FeO within such slags (Pistorius, 2003). However, in actual practice the compositions of such slags lie below this eutectic groove, but just above the M_3O_5 stoichiometric composition (dashed line **B** that is characterized by the Ti_3O_5-$FeTi_2O_5$ end members) (Pistorius, 2002; Pistorius and Coetzee, 2003; Pistorius, 2003; Pistorius, 2004).

The location of the compositions of industrial titania slags in Figure 2.2 shows that such slags contain a higher TiO_2 content and a lower Ti_2O_3 content than it is required by the slag-metal equilibrium (line **C**). This higher amount of TiO_2 in industrial titania slags than it is required by the slag-metal equilibrium composition dictates that the reaction in Equation 2.3 is out of equilibrium to the right (Pistorius, 2002), which is an indication that the reactions in Equations

2.1 and 2.2 favour the production of both metallic iron and tetravalent titanium.

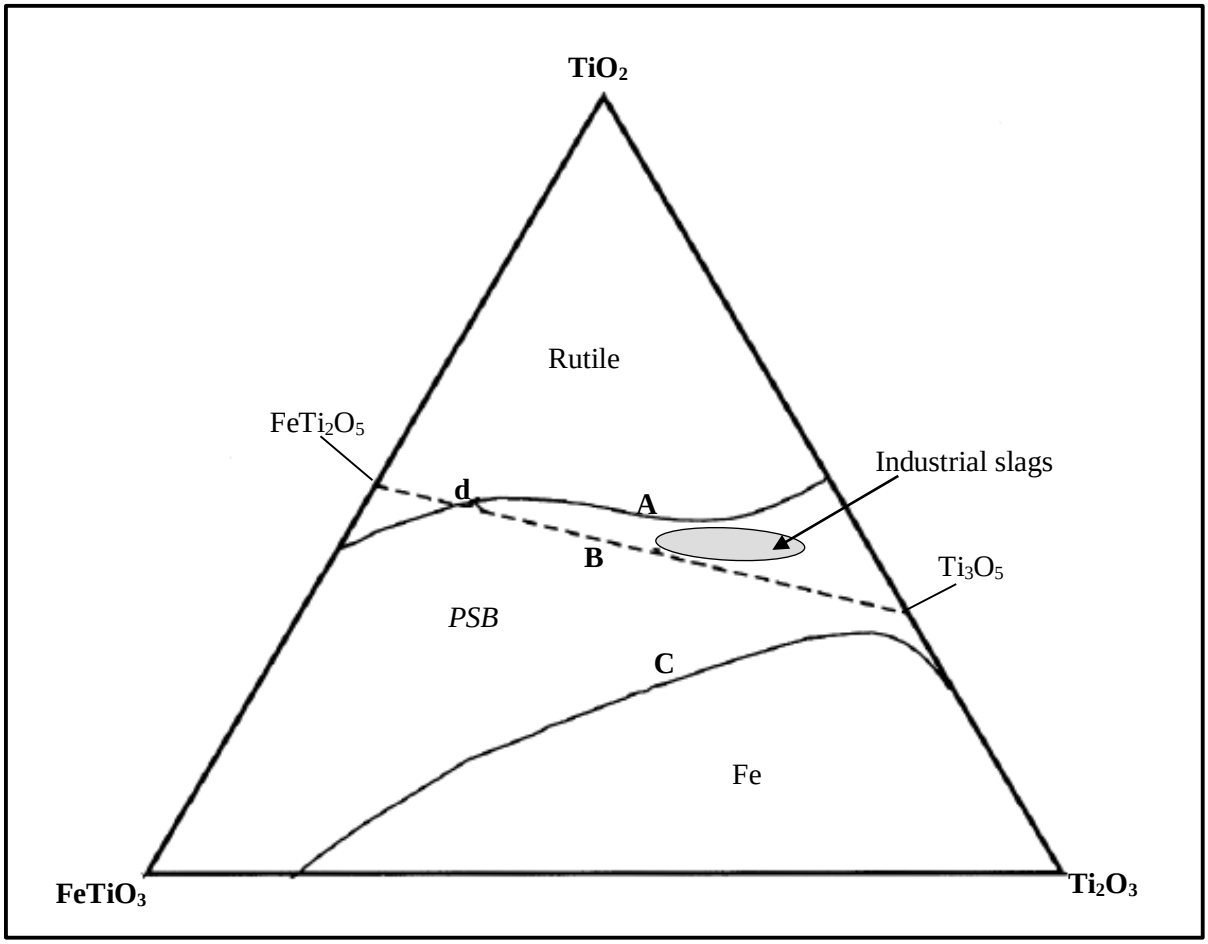

Figure 2.2: The primary phase regions within the $FeTiO_3 - TiO_2 - Ti_2O_3$ ternary system as calculated by FACT® (Pistorius and Coetzee, 2003). Figure reused with permission of Springer and Copyright Clearance Center.

Nevertheless, the departure of the reaction in Equation 2.3 from chemical equilibrium may not necessarily imply a departure from the M_3O_5stoichiometry (Pistorius, 2002). A slight deviation of the titania slags from the M_3O_5 stoichiometry has been attributed to the presence of the impurity oxides that displace the divalent iron, tetravalent and trivalent titanium from the *PSB* structure and such deviation is found to be more significant when the impurity oxides are present within the slag phase in large quantities (Pistorius, 2002).

A further observation in Figure 2.2 is that the calculated eutectic groove somehow overestimates the TiO_2 content within the industrial titania slags (Pistorius, 2003; Pistorius, 2004). In addition, the calculated slag-metal equilibrium boundary may put forward a doubt. Elstad et al. (2007) argued with the use of experimental observations that this equilibrium boundary between a titania slag and a metallic iron follows a curved line with its apex just above the M_3O_5 stoichiometric composition where the compositions of industrial slags lie. Seim and Kolbeinsen (2009) later substantiated these observations from Elstad et al. (2007).

A further observed discrepancy between the experimental and the calculated observations within the $FeTiO_3$-TiO_2-Ti_2O_3 system is with regard to the liquidus of such system. A comparison of the FactSage(merger of FACT® and ChemSage®)-calculated liquidus isotherms and experimentally measured liquidus isotherms at 1500˚C and 1600˚C showed that FactSage somehow overestimates the liquidus of the slags that are rich in FeO and it underestimates the liquidus of the slags that have low content of FeO (Zietsman, 2004). These inconsistencies between the calculated and the experimental observations within the $FeTiO_3 - TiO_2 - Ti_2O_3$ ternary system may therefore prompt a further critical thermodynamic assessment of such system in order to minimise such discrepancies.

2.1.4. Behaviour of the impurity oxides

Ideally, the ease with which the oxides can be carbothermically reduced is as follows according to Lee (1999).

$$FeO > Cr_2O_3 > MnO > SiO_2 > TiO_2 > Al_2O_3 > MgO > CaO$$

However, most impurity oxides are not significantly reduced during the production of a titania slag, but these impurity oxides remain in the slag phase (Pesl, 1997; Pistorius and Coetzee, 2003; Elstad et al., 2007; Pistorius, 2008). A challenge to reduce these impurity oxides from the titania slag-metallic iron system depends solely on the behavior of such oxides within that system. The equilibrium constants (K_{eq}) of the reactions were calculated by FactSage 6.4.

The reduction of silica is significant only at high carbon additions (Pesl and Eric, 2002). At such relatively strong reducing conditions, silica can undergo reduction according to a reaction in Equation 2.4 (Jones et al., 1993; Pesl and Eric, 2002). However, the conditions that favour this

considerable reduction of silica coincide with the conditions that favour a gradual reduction of the titanium oxides to titanium carbides and ultimately to metallic titanium. Operating the smelters at those conditions therefore leads to a significant loss of such titanium oxides from the slag phase.

$$SiO_2(l) + C(s) \rightleftharpoons SiO(g) + CO(g),\ K_{eq,\ 1650^{\circ}C} = 1.1x10^{-01} \quad \ldots\ldots\ldots\ldots\ldots\ldots \quad (2.4)$$

As the slag solidifies, silica forms separate silicate phases that exist intergranularly within the bulk solid slag (Elstad et al., 2007). The matrix of these silicate phases is dominant in the impurity oxides, but some amounts of the oxides of iron and titanium can also be present (Borowiec et al., 1998; Pesl and Eric, 2002; Pistorius and Coetzee, 2003; Elstad et al., 2007). It has further been found that titania slags that are rich in silica have a relatively higher content of Ti_2O_3 than the slags that are rich in either MgO or CaO for the same amount of FeO (Elstad et al., 2007).

The oxides of manganese and chromium are relatively easy to remove from the slag phase within the optimum reductant-to-ore ratio regime. Thermodynamically, MnO is more stable than Cr_2O_3 (Lee, 1999) and one can predict the preferable reduction of Cr_2O_3 over MnO in a mixture of these oxides. However, the higher vapour pressure of manganese metal, as Table 2.1 shows, renders MnO to be easily reduced from the slag than Cr_2O_3 (Pesl and Eric, 2002). While manganese is significantly collected into the off-gas stream, chromium reports mainly into the metallic phase (Jones et al., 1993; Pesl and Eric, 2002). The reactions in Equations 2.5 and 2.6 show the reduction of manganese oxide and chromium oxide respectively.

$$MnO(l) + C(s) \rightleftharpoons Mn(g) + CO(g),\ K_{eq,\ 1650^{\circ}C} = 1.34x10^{01} \quad \ldots\ldots\ldots\ldots\ldots \quad (2.5)$$

$$Cr_2O_3(l) + 3C(s) \rightleftharpoons 2Cr(l) + 3CO(g),\ K_{eq,\ 1650^{\circ}C} = 2.54x10^{05} \quad \ldots\ldots\ldots \quad (2.6)$$

A slag that is rich in MnO tends to form a pyrophanite phase ($MnTiO_3$). This phase forms stable solutions with unreacted ilmenite thereby reducing the FeO activity. A lesser extent of reduction is therefore encountered. However, the oxides of manganese are found to serve as an excellent fluxing agent in titania slags (Pesl, 1997).

Magnesia, alumina and calcium oxide are some of the oxides that require temperature to be

significantly high in order to achieve their carbothermic reduction (Lee, 1999). Magnesia and alumina further impose the greatest difficulty in their removal from the titania slag phase because they easily get accommodated within the PSB lattice structure and the silicate phases during the mildly reducing conditions (around half of the stoichiometric amount of carbon) (Pesl and Eric, 2002; Elstad et al., 2007; Seim and Kolbeinsen, 2009). In strongly reducing conditions, magnesia and alumina react with the oxides of titanium and iron to form $Al\text{-}Mg$ spinel (Sommerville and Bell, 1982; Pesl, 1997; Pesl and Eric, 2002). This in turn increases the liquidus temperature of titania slags because of the high melting points of magnesium titanates and aluminium titanates (Pesl, 1997; Elstad et al., 2007).

Table 2.1: Vapour pressures of some oxides and metals as calculated by FactSage® 6.4 at 1650˚C.

Reactants	Vapour pressure (atm)	
	Metal oxides	Metal
$FeO + C$	$2.60\text{x}10^{-10}$	$1.55\text{x}10^{-04}$
$Cr_2O_3 + C$	$CrO = 4.28\text{x}10^{-06}$, $CrO_2 = 3.12\text{x}10^{-08}$, $CrO_3 = 7.45\text{x}10^{-13}$	$4.47\text{x}10^{-04}$
$MnO + C$	0.00	$7.74\text{x}10^{-02}$
$SiO_2 + C$	$SiO = 1.40\text{x}10^{-01}$, $SiO_2 = 6.35\text{x}10^{-08}$	$1.69\text{x}10^{-05}$
$TiO_2 + C$	$TiO = 2.10\text{x}10^{-07}$, $TiO_2 = 2.11\text{x}10^{-09}$	$2.79\text{x}10^{-08}$
$Al_2O_3 + C$	$AlO = 2.71\text{x}10^{-08}$, $Al_2O = 3.99\text{x}10^{-03}$, $Al_2O_2 = 1.36\text{x}10^{-08}$, $Al_2O_3 = 2.01\text{x}10^{-17}$	$8.24\text{x}10^{-04}$
$MgO + C$	$2.52\text{x}10^{-08}$	$1.97\text{x}10^{01}$
$CaO + C$	$2.73\text{x}10^{-09}$	$1.52\text{x}10^{00}$

The presence of calcium oxide in the furnace charge leads to titania slags that solidify with a separate perovskite phase ($CaTiO_3$) within the bulk slag structure (Pesl, 1997). This is due to the fact that CaO is not readily incorporated within the PSB structure because of the relatively large radius of calcium atoms. The perovskite phase also remains stable even under strongly reducing conditions (Pesl, 1997). For this reason, the removal of CaO from a titania slag by reductive smelting is also a challenge. Nevertheless, Elstad et al. (2007) highlighted that the advantage of the presence of CaO in titania slags is to depress the eutectic point between the PSB and the rutile phases and this phenomenon increases the stability region of the liquid slag.

2.2. Ilmenite smelters furnace dust

As the furnace charge is fed, the fraction of such charge that has a lower terminal velocity than the upward velocity of the escaping gas is entrained into the furnace freeboard. Moreover, a slightly positive pressure within the electric arc furnaces tends to force some of the charge to the furnace freeboard (Kudryavskii, 2004; Zietsman, 2004). Because of the dependence of the particles terminal velocity on the particle size and density, the fraction of the charge, which is entrained into the furnace freeboard, is often the finely disseminated portion and lightweight particles.

The amount of this fine fraction within the furnace can be increased by a breakage of the feed particles due to thermal shock when such particles enter the hot electric arc attachment zone. The entrainment of this fine material together with volatilized species from the slag and metallic phases can explain a thick, dusty cloud that is often observed during the operation of the furnaces (Zietsman, 2004). The particulate concentration within this thick cloud can range from 50 g/Nm^3 to 200 g/Nm^3 (Gottschling, 2009). Although not accurately quantified, it has been estimated that 1000 ton of this furnace dust can be produced per 10000 ton of the titanium sponge that is produced per annum (Kudryavskii, 2004).

The chemical analysis of the furnace dust has revealed that such furnace dust can be rich in the oxides of titanium and iron, which can be associated with significant amounts of the impurity oxides. A typical chemical composition of such furnace dust is summarized in Table 2.2.

Table 2.2: A typical composition of the ilmenite smelters furnace dust (Cyr et al., 2000; Kudryavskii, 2004; Rughubir and Bessinger, 2007).

Species	TiO_2	Fe total	Al_2O_3	SiO_2	Cr_2O_3	V_2O_5	MnO	K_2O	$MgO + CaO$	C
Abundance (wt%)	20-52	21-25	1-3	6-17	4-5	0.2-0.3	3-3.7	0.6-0.7	2-10	2-3

Depending on the composition of the smelter-grade feed, such furnace dust can sometimes be enriched with some high vapour pressure species such as lead, zinc and arsenic. Sometimes the furnace dust can be associated with the α- and β-emitting radionuclides (Kudryavskii, 2004). The

concentration of these metal volatiles can go as high as 0.9wt% while that of the radionuclides can reach up to 20000 Bq/kg of the furnace dust (Kudryavskii, 2004). This possible maximum radioactivity of the furnace dust can exceed the specifications that are set by some of the radiation safety standards such as the NRB-99 and OSPORB-99 (Kudryavskii, 2004) and it may dictate the care with which the furnace dust may need to be handled.

An ilmenite furnace dust is a finely disseminated material with the mean particle size lying between 0.1 μm and 200 μm (Cyr et al., 2000; Kudryavskii, 2004; Rughubir and Bessinger, 2007). Furthermore, this furnace dust can be a very complex material that consists of polyphasic synthetic structures (Cyr et al., 2000). The titanium- and iron-bearing mineral phases within this material are mainly ilmenite, rutile, PSB phases and metallic iron (Rughubir and Bessinger, 2007). Such mineral phases are found to be intimately inter-grown with significant amounts of the impurity oxides (Cyr et al., 2000; Rughubir and Bessinger, 2007).

The possible utilization of this furnace dust in the cementitious materials has been investigated by Cyr et al. (2000). The authors (Cyr et al., 2000) showed that the use of the furnace dust either in the pure form or mixed with alkali component such as $Ca(OH)_2$, has marginal technical advantages because a paste of such mixtures remain friable even after several months. An enhancement of the mortars mechanical strength could however be observed when such furnace dust was added to a commercial cement at a rate less than 10wt% (Cyr et al., 2000).

Later in 2004, it was further suggested that an addition of such furnace dust to the titania slag prior to chloride or sulphate processing can be an alternative to managing this metallurgical waste stream (Kudryavskii, 2004). However, it is worth noting that the suggestion made by Kudryavskii (2004) increases the impurities burden on such downstream processes, which would ultimately render such processes inefficient.

The potential of recovering a titania slag from such furnace dust was investigated by Rughubir and Bessinger (2007). The authors (Rughubir and Bessinger, 2007) found that a titania slag that contains more than 75wt% of ${TiO_2}^{eq}$ was possible to obtain. Nevertheless, the impurity oxides that were present within the furnace dust could not be removed by reductive smelting and the resultant slag was associated with significant amount of such impurities. Rughubir and Bessinger

(2007) concluded by suggesting a further enrichment of such titania slag. A hydrometallurgical flowsheet that is illustrated in Figure 2.3 from the invention of Borowiec et al. (1998) has been found to effectively remove most of the impurity oxides together with any residual iron from the

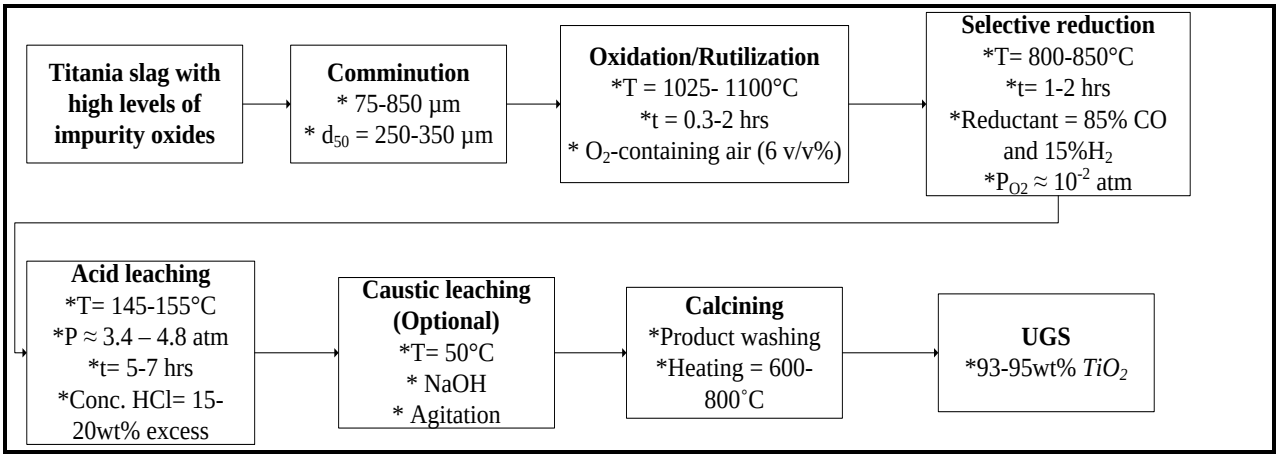

Figure 2.3: A flowsheet for the production of an upgraded slag. Developed from (Borowiec et al., 1998).

titania slags thereby resulting into an upgraded slag (UGS) containing 93-95wt% TiO_2. Lasheen (2008) and Dong et al. (2012) have further suggested a soda-ash roasting of slags in order substitute for the oxidative and reductive steps in Figure 2.3, which might be challenging to control.

Nevertheless, most ilmenite smelting operations are currently disposing of such furnace dust as a waste material in the lined residue facilities or mined-out areas (Cyr et al., 2000; Namakwa Sands, 2003; Gous, 2006; Rughubir and Bessinger, 2007; de Jong and Mitchell, 2010). Kudryavskii (2004) has further shown that such furnace dust can be combined with the residues from the downstream chloride and sulphate processes and further mixed with gypsum or magnesia binders to form stable solids that are safe for disposal in landfills.

2.3. Summary

The reductive smelting of titaniferous ores is different from the traditional reductive smelting processes in few ways. Firstly, the titania slag is considered as a primary product while in

traditional cases, the slag is often considered as a discard. Secondly, the use of fluxes during the production of titania slags is not employed because such use of fluxes can render the process counterproductive.

The carbothermic reduction of titaniferous ores to high titania slags at 1600-1700˚C results in the significant reduction of FeO to metallic Fe and such reduction is found to be more influenced by the carbon addition than the operating temperature. Most of the impurity oxides that may be present within the slag phase are not significantly removed, but they remain within such slag phase. For this reason, the feasibility of removing most impurity oxides from the titania slag through reductive smelting is minimal.

It was further found that the titania slags solidify mainly as the PSB phase with the M_3O_5 stoichiometric composition. The dominance of such PSB phase was found to emanate from a combination of the eutectic solidification equilibrium of the liquid slag with the freeze lining and the transient solidification and re-melting of such slags at the slag-metal interface. Such PSB phase tends to be immiscible with the silicate phases for slags that are rich in the impurity oxides. Furthermore, the industrial titania slags have more TiO_2 content than it is required by the slag-metal equilibrium composition and this translates that an upgrading of titania slags favour the production of both TiO_2 and Fe.

A review of current literature further showed that an ilmenite smelting furnace dust can be rich in titania and the oxides of iron. However, this furnace dust can be associated with impurity oxides. The fineness of this furnace dust could be comparable to that of commercial cement, but its application in cement-based materials was of minimal advantage. The recovery of titania and metallic iron from such furnace dust was therefore be of importance in order to minimise the loss of such valuables as waste.

3. Experimental study

This section provides sampling procedures and preparation of materials for subsequent analyses together with experimental test work. In this chapter and other subsequent chapters, ore will sometimes be used to refer to the furnace dust. The equipment that was used to achieve the experimental tests is described after which the operating procedures for sample characterization and the experimental tests are provided.

3.1. Materials

A bulk furnace dust sample was collected in a form of slurry from the thickener underflow within the Theisen disintegrator off-gas cleaning plant at the TKZNS industrial site. This slurried sample was filter-pressed within the industrial site after which it was transported from the industrial site to Stellenbosch University. Such slurried furnace dust sample is depicted in Figure 3.1(a).

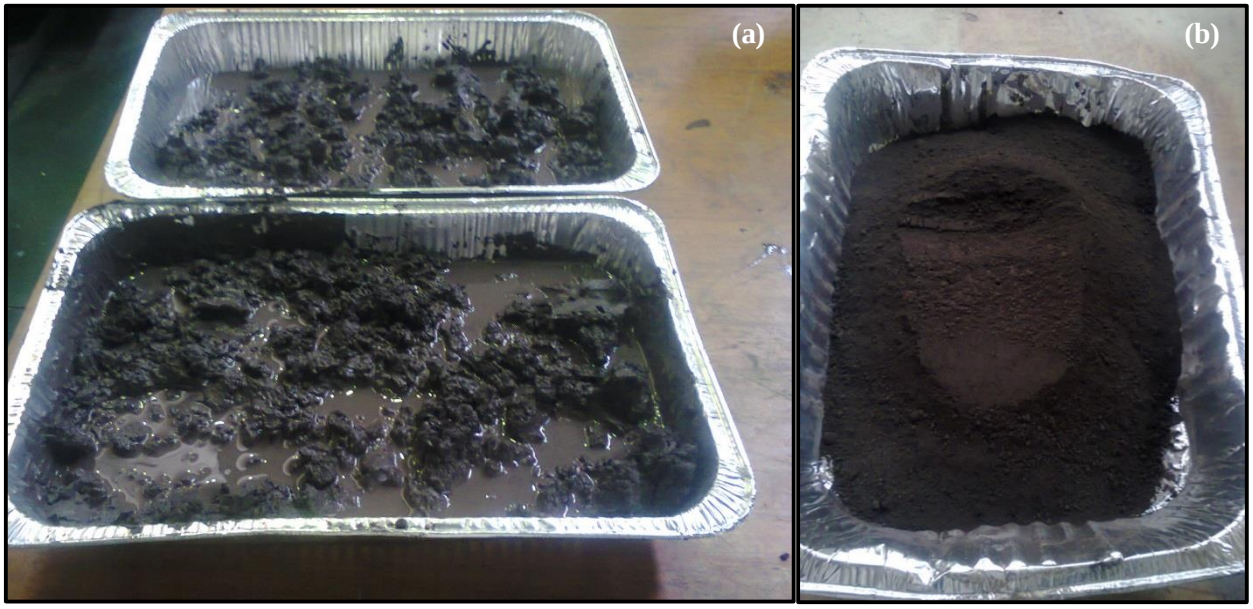

Figure 3.1: A pictorial view of the furnace dust sample as collected from the thickener underflow **(a)** and a portion of the dry, pulverised furnace dust sample **(b)**.

Upon arrival at Stellenbosch University, the filter-pressed sample was dried for two weeks in a

laboratory oven that was operated at 60˚C. The sample caked upon drying. The caked bulk furnace dust sample was therefore gently pulverized with the use of a motor and pestle and it was subsequently divided into representative samples through the use of a rotary splitter. An image of a dry, pulverized sample of the furnace dust is shown in Figure 3.1(b).

Anthracite, distilled water and AFROX high purity argon gas (99.998wt% argon) were additional materials that were used in this study. A bulk sample of crushed anthracite was sampled with the use of a rotary splitter and it was subjected to particle size distribution (PSD) analysis, proximate analysis and carbon, hydrogen and nitrogen (CHN) analysis. The PSD analysis was achieved by using a nest of test sieves with the ratio of adjacent sieves being approximately $\sqrt[4]{2}$. The CHN analysis was achieved with the use of x-ray fluorescence (XRF) spectroscopy while the proximate analysis was achieved through the use of a thermogravimetric analysis (TGA) technique. The PSD analysis data is summarized in Table A.1 and such data is further depicted in Figure A.1. The composition of such anthracite is presented in Table A.2 within the appendix section.

From the CHN analysis in Table A.2, such anthracite was found to contain 77.82wt% of fixed carbon. The PSD analyses also showed that 80% of this material was below 1.40 mm and particles in the size range +1.18-1.40 mm had the highest frequency. This anthracite was therefore relatively finer than the size that was recommended by Brent (1987).

The furnace dust and anthracite were therefore mixed at the required mass ratios after which such mixture was moistened by 17wt% of distilled water. The mixtures were subsequently compacted into briquettes of 16 mm in diameter and 10 mm in height in order to minimize the loss of the fine furnace dust and anthracite into the off-gas stream. To avoid or minimize any further breakage of such briquettes upon drying, the briquettes were finally hardened by firing at 1000˚C for 15 minutes inside a muffled furnace. A pictorial view of some of such hardened briquettes is shown in Figure 3.2 and these hardened briquettes were used during the experimental reduction tests for the production of a titania slag and a metallic iron.

Figure 3.2: A pictorial view of some of the furnace dust briquettes that were fired in a muffled furnace at 1000˚C for 15 minutes.

3.2. Equipment

A laboratory scale, PVT 18/75/350 Carbolite® vertical tube furnace that was located in the Department of Process Engineering at Stellenbosch University was used. Hereafter, this PVT 18/75/350 Carbolite® vertical tube furnace will be referred to simply as a vertical tube furnace. The schematic of such furnace is depicted in Figure 3.3 while its pictorial view is shown in Figure 3.4. In addition to this vertical tube furnace, an auxiliary furnace was used to de-moisturize and to de-oxidize the purge gas. A description of the vertical tube furnace is initially provided followed by the description of such auxiliary furnace. The crucibles that were used for this work are finally described.

The vertical tube furnace consisted of a vertical alumina tube with an internal diameter of 73 mm and a length of 1195 mm. Samples are loaded within this alumina tube. The top end of the alumina tube was covered with the airtight metal plates that were water-cooled. Through these metal plates, a residual purge gas and fumes that are generated from the reaction zone can flow

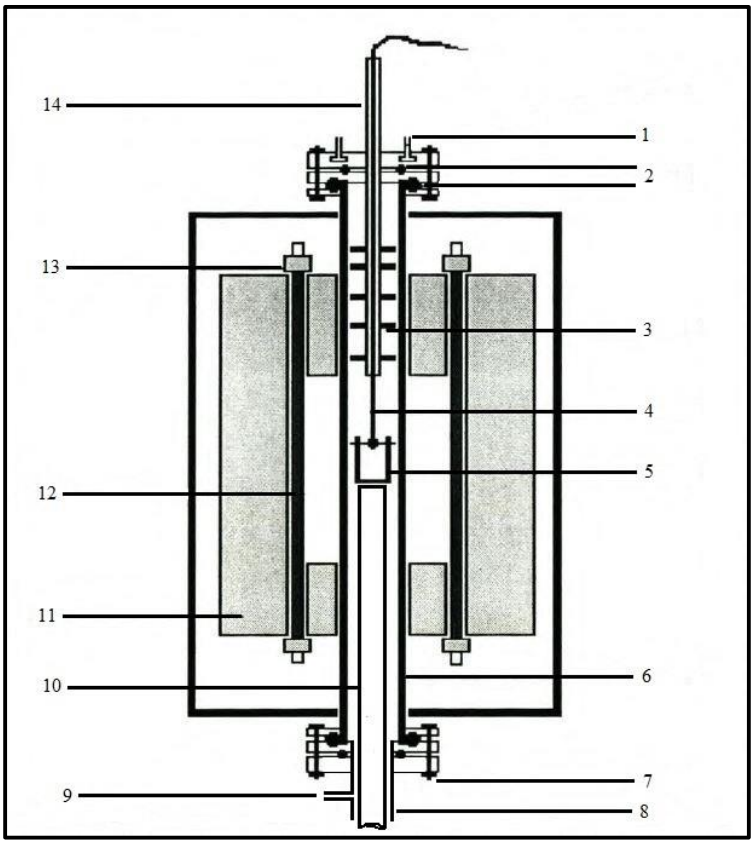

Figure 3.3: A schematic diagram of the vertical tube furnace. The diagram was modified after Banda (2001). 1. Cooling water system, 2. Rubber seals, 3. Radiation shield, 4. Sample holding wire, 5. Crucible, 6. Alumina tube, 7. Bolt and nut, 8. Aluminium tube, 9. Purge gas inlet, 10. Sample holding pedestal, 11. Insulation material, 12. Heating element, 13. Element support collar, 14. Gas outlet ceramic pipe.

out of the alumina tube. The top end of this tube was further fitted with a radiation shield in order to allow for an efficient heating at the reaction zone. The bottom of the alumina tube was fitted with a 100 mm long aluminium tube and it is through this aluminium tube the purge gas enters the alumina tube.

This vertical tube furnace was electrically heated by six elements that surrounded the alumina tube and it was specified to operate at a temperature not exceeding 1800˚C with a maximum wattage of 8.0 kW. Temperature inside the furnace was sensed by two thermocouples that were

Figure 3.4: A pictorial view of the vertical tube furnace. The furnace was supported on a hydraulic pallet lifter for ease of upward and downward movements.

calibrated to R-type on the external programmable Eurotherm 2416 temperature controller and the Eurotherm 2132 overtemperature controller. During an over-temperature condition inside the furnace, the Eurotherm 2132 overtemperature controller cuts power supply to the heating elements and power is not restored until such controller is reset.

A crucible that is filled with a furnace charge can be placed into a hot zone by pulling it up through the aluminum tube with the use of a high temperature-resistant wire. Alternatively, such crucible can be supported on a ceramic pedestal while the furnace is lowered by the hydraulic pallet lifter until the crucible is within the proximity of such hot zone.

The type TF furnace that was used to de-moisturize and to de-oxidize the purge gas consisted of

a tube in the middle that was packed with copper turnings. Hereafter, this furnace will be referred to as a copper tube furnace. The purge gas inlet pipe to this copper tube furnace was fitted with a glass tube that was filled with crystallized silica gel. This silica gel served to absorb moisture that would be present within argon gas while the copper turnings served to de-oxidize such gas.

A choice of the crucible material was very challenging in this present study because titania slags are corrosive to all known oxide refractories (Pistorius, 2003; Zietsman, 2004; Elstad et al., 2007). However, the graphite crucibles were ultimately selected and they were used. A pictorial view of one of such crucibles is shown in Figure 3.5. These crucibles were cylindrical and their bottom internals were slightly tapered in order to enhance the collection of a metallic phase. The crucibles measured an outer diameter of 50 mm, outer height of 40 mm and internal height of 30 mm.

Figure 3.5: One of the graphite crucibles that was used during the experimental reduction tests.

3.3. Method

3.3.1. Analytical techniques

(a) Particle size analysis

A particle size distribution of the furnace dust sample was determined with the use of the Saturn DigiSizer 5200 V1.10 that was located in the Process Engineering Department at Stellenbosch University. This instrument was based on a laser diffraction method to determine the particle size. The sample was dispersed in a water medium to form a suspension of 0.00139wt% solids. This suspension was drawn into the size analyser at a flow rate of 12.0 L/min and at a circulation time of 60 seconds. The Saturn DigiSizer 5200 V1.10 reported a particle size distribution by volume. It was therefore assumed that the density of particles within the furnace dust did not significantly vary from one size class to another and on that basis, the volume distribution could be regarded to be similar to the weight distribution (Rhodes, 2008).

(b) Chemical analysis

An elemental composition of the samples was determined by the XRF technique in the Central Analytical Facilities at Stellenbosch University. The slag samples were ground using a disc grinder with a hardened metal lining prior to analyses. All the powdered samples were prepared into fused beads by mixing them with lithium tetraborate flux after which the mixtures were fused at 1000˚C. During this oxidative fusion, some chemical species within the samples were oxidized to higher oxidation state. After the sample preparation, a PANalytical XRF instrument with a rhodium target tube that was operated at 3 kW was used to identify and quantify the elements. For calibration of the instrument and verification of results, the samples were analysed with the standard reference materials. The relative abundance of the major elements was reported as oxides while the relative abundance of the trace and light elements was reported directly as a concentration of such elements. The carbon content of the furnace dust was further determined by LECO analysis.

(c) Mineralogical analysis

The mineralogical characteristics of the samples were determined with the use of an x-ray diffraction (XRD), scanning electron microscopy (SEM) and transmission electron microscopy

(TEM) techniques. The XRD analyses were carried out by the XRD Analytical and Consulting cc in Pretoria while the microscopic analyses were carried out in the Central Analytical Facilities at Stellenbosch University.

The furnace dust and the slag samples were prepared using a backloading preparation method for the XRD analysis. Such samples were analysed with an addition of 20% silicon standard. An addition of such silicon standard made it possible to quantify the amorphous content within the samples and to help with micronizing in a McCrone micronizing mill. The samples were analysed using a PANalytical Empyrean diffractometer. The diffractometer was fitted with a PIXcel detector and fixed slits with Fe filtered Co-Kα radiation. The mineral phases within the samples were identified through the use of the X'Pert Highscore plus software while the quantification was estimated through the use of the Rietveld method.

Prior to the SEM analyses, the furnace dust, slag and metallic iron samples were prepared into block mounts by embedding them in an epoxy resin that was made of a mixture of 2.5 g SpeciFix resin and 1.0 g SpeciFix-40 curing agent. The embedded samples were subsequently left in an oven that was operated at 40˚C for at least twelve hours in order to set. The surfaces of the hardened block mounts were ground and finally polished with the use of Struers Rotopol-35 polisher in conjunction with the Struers DP Diamond pastes in order to enhance the flatness and smoothness. The polished block mounts were further coated with a thin layer of gold to enhance the conductivity such that the incident electrons that were thermionically emitted from the SEM gun could not be repelled by the otherwise accumulating electrons on the samples.

The z-contrast images, which were produced from the backscattered electrons (BSE) and spot analyses of different phases were achieved with the use of a Zeiss EVO® MA15 Scanning Electron Microscope that was coupled with an energy dispersive spectroscopy (EDS). This instrument could perform high-resolution imaging concurrently with quantitative analysis of elements with errors ranging from 0.6wt% to 0.01wt% for major elements. An Oxford Instruments® X-Max 20 mm^2 detector and an Oxford INCA software were used to identify the mineral phases and to quantify the compositions of such phases. During the analyses, the beam conditions were kept at 20 kV and approximately 1.0 A, with a working distance of 8.5 mm and a specimen beam current of -20.00 nA. The Astimex Microanalysis Standards were used for

standardization and verification of the analyses. Pure Co was periodically used to correct for the detector drift.

The TEM micrographs were accomplished with the use of a JEOL 1200-EX II Transmission Electron Microscope. These micrographs were generated for the furnace dust only. During an analysis, the beam conditions were 120 kV, an objective aperture setting of 150 microns and a spot size of 3 µm were also set. The furnace dust sample was imaged with the digital imaging acquisition using an Orius™ SC 200 CCD Camera with Gatan Microscopic software. The largest resolution of 1376 x 1032 with an exposure time of 2 seconds was employed.

3.3.2. Reduction test work

The reduction test work was divided into three stages namely furnace preparation, simulation modelling and experimental reduction tests. The furnace preparation stage involved calibration of the vertical tube furnace, assessment of the performance of such furnace and the determination of the hot zone within the alumina tube of such vertical tube furnace. The simulation modelling stage involved characterization of the carbothermic reduction process of the furnace dust at different conditions and determination of the feasible experimental reduction conditions with the use of FactSage® 6.4 software package. Finally, the experimental reduction tests involved production of both a titania slag and metallic iron from the briquetted furnace dust samples at the feasible conditions that were determined by using FactSage® 6.4.

(a) Furnace preparation

An external R-type thermocouple (TC-1) that was connected to the HE701 thermocouple data-logging thermometer was inserted on top of the furnace through the gas outlet ceramic pipe. The programmable external temperature controllers were finally switched on. The temperature value of 1650˚C was set on the Eurotherm 2416 main controller while a set point of 1665˚C was set on the Eurotherm 2132 overtemperature controller. The furnace was subsequently allowed to heat up. The furnace performance before and after calibration is depicted in Figure A.2 and Figure A.3 respectively.

After the furnace had attained a thermal equilibrium at 1650˚C, the other two R-type thermocouples (TC-2 and TC-3) were used to locate the hot zone within the alumina tube. The

set-up in Figure A.4 within the appendix section was used to achieve this. The hot zone within the alumina tube was located at 500 mm from the furnace top and this hot zone was used as a placement point for crucibles that contained the briquetted furnace dust samples throughout the experimental reduction tests.

(b) Simulation modelling

The chemical composition of the furnace dust that was obtained from the XRF analysis served as an input to the FactSage® 6.4 software models. FactSage® incorporates eleven different solution models, but it uses a modified quasichemical model for titania slags and a two sub-lattice model for the PSB phase (Bale et al., 2002; Pistorius, 2003; Pistorius, 2004; Fourie et al., 2005).

There are also several FACT (Facility for the Analysis of Chemical Thermodynamics) databases that are incorporated within FactSage®. However, only the FACT databases that were used in this study are presented.

FactPS: This database provides a list of all compound species that are available within the FactSage® thermodynamic databank. It is a new name for Fact53, which is found in FactSage® 6.2 and older versions.

FTmisc: This database was used for the metallic phase. It is a miscellaneous database for several systems such as matte systems, non-ideal aqueous solutions and liquid alloys. An alloy of liquid iron with dilute solutes of Ag, Al, B, Ba, C, Ca, Ce, Co, Cr, Cu, H, Hf, La, Mg, Mn, Mo, N, Nb, Nd, Ni, O, P, Pb, Pd, S, Si, Sn, Ta, Th, Ti, U, V, W, Zr (FTmisc-FeLQ) is highly recommended for calculations that involve iron-rich solutions such as in iron- and steel-making processes. This database is not selected simultaneously with any other liquid metallic solution database.

FToxid: This database was used for the slag phase. It is generally a database for solutions such as slags, glasses, ceramics and refractories. It contains data for oxides and oxide solutions of the following components; Al_2O_3, As_2O_3, B_2O_3, CaO, CoO, CrO, Cr_2O_3, Cu_2O, FeO, Fe_2O_3, GeO_2, K_2O, MgO, MnO, Na_2O, NiO, PbO, SiO_2, SnO, TiO_2, Ti_2O_3, ZnO, ZrO_2 (Bale et al., 2009). The dilute solutes of S-SO_4-PO_4-CO_3-F-Cl-I-OH-H_2O are also included (Bale et al., 2002; Bale et al., 2009).

After defining the inputs to the models and the above-mentioned databases, the possible product phases were selected as ideal gas and pure liquids. The possible solution species that were selected included Fe-liq, ASlag-liq all oxides + S, solution oxides (ASpinel, Titania spinel, Melilite and AOlivine), Amonoxide, Corundum (M_2O_3), Rutile, AIlmenite, Pseudobrookite, Perovskite ($CaTiO_x$) and Rhodonite ($(Mn, Ca, Fe, Mg)SiO_3$). Pressure was left at 1atm and the normal equilibrium simulations were executed.

The simulation runs were performed at different Ore-C ratios ($\frac{Mass\ furnace\ dust\ excluding\ loss\ on\ ignition\ (g)}{Mass\ carbon\ (g)}$) and each Ore-C ratio was tested at different temperatures (1500˚C, 1550˚C, 1600˚C, 1650˚C, 1680˚C and 1700˚C) in order to understand the product chemistry at those different conditions. A total of 20 g of the feed per each run was used and the amounts of each oxide that were used during such FactSage modelling are summarized in Table 3.1. This data was calculated from the XRF data that is presented in Table 4.1 using the Equations A.1 to A.3.

Table 3.1: The amounts of reactants that were used in FactSage modelling.

Species	Mass (g)											
Al_2O_3	0.238	0.236	0.235	0.234	0.232	0.231	0.230	0.229	0.227	0.226	0.225	0.223
CaO	0.031	0.030	0.030	0.030	0.030	0.030	0.030	0.029	0.029	0.029	0.029	0.029
Cr_2O_3	0.021	0.021	0.021	0.021	0.021	0.020	0.020	0.020	0.020	0.020	0.020	0.020
Fe_2O_3	5.539	5.509	5.479	5.448	5.421	5.391	5.361	5.334	5.305	5.272	5.242	5.211
K_2O	0.296	0.294	0.293	0.291	0.289	0.288	0.286	0.285	0.283	0.281	0.280	0.278
MgO	0.154	0.153	0.152	0.151	0.150	0.149	0.149	0.148	0.147	0.146	0.145	0.144
MnO	0.623	0.620	0.616	0.613	0.610	0.606	0.603	0.600	0.597	0.593	0.590	0.586
Na_2O	0.144	0.143	0.142	0.142	0.141	0.140	0.139	0.139	0.138	0.137	0.136	0.136
P_2O_5	0.035	0.035	0.035	0.035	0.035	0.034	0.034	0.034	0.034	0.034	0.033	0.033
SiO_2	1.969	1.958	1.948	1.937	1.927	1.916	1.906	1.896	1.886	1.874	1.864	1.852
TiO_2	9.269	9.218	9.168	9.116	9.071	9.020	8.971	8.926	8.876	8.821	8.772	8.719
Zn	0.362	0.360	0.358	0.356	0.354	0.352	0.350	0.349	0.347	0.345	0.343	0.341
Total C	1.262	1.366	1.466	1.570	1.662	1.765	1.864	1.955	2.056	2.168	2.267	2.375
Ore-C ratio	14.8	13.6	12.6	11.7	11.0	10.3	9.7	9.2	8.7	8.2	7.8	7.4

(c) Experimental reduction tests

From the simulation modelling test work, the Ore-C ratio of 9.7 provided the maximum achievable $TiO_2{}^{eq}$ content in the slag phase with the minimum deportment of titanium into the metallic phase. This Ore-C ratio was therefore selected for the experimental reduction tests. The liquidus of the system with such Ore-C ratio was firstly calculated with FactSage® 6.4. The heating process from 1000˚C to 1700˚C was simulated and only the transitions were calculated during such simulation process. The liquidus of the system was found to be 1624.83˚C. Most experimental reduction tests were therefore carried out at 1650˚C, which was almost 25˚C above the liquidus of the system.

Approximately 20 g of the briquetted mixture of the furnace dust and anthracite was charged per each run and the experimental reduction tests were performed at 1650˚C with the reduction times ranging from 2 minutes to 10 minutes. The reduction of iron oxides from the slag phase was found to be almost complete after the reduction time of 6 minutes as it is depicted in Figure A.5 within the appendix section. Further experimental runs were performed at 1600˚C and 1500˚C for the reduction time of 10 minutes.

The experimental reduction test procedure was initiated by heating up both the vertical tube furnace and the copper tube furnace. The temperature controllers on the vertical tube furnace were run in an auto mode. A desired temperature value was set on the Eurotherm 2416 main controller and a temperature value that was 15˚C higher was set on the Eurotherm 2132 overtemperature controller. The ramp rate to the required set-point was set at 35˚C/min. Temperature on the copper tube furnace was set at 550˚C. This temperature value was within 500˚C (Pesl, 1997) and 600˚C (Darken and Gurry, 1945). Both furnaces were subsequently allowed to reach to the set temperature values.

After the furnaces had attained the required temperature, the Eurotherm 2416 main controller was put on a hold mode. A graphite crucible that was filled with a briquetted mixture of the furnace dust and anthracite was placed on an alumina pedestal. This pedestal was 1.01 m long and it was fitted with a 50 mm outer diameter disc on top for placement of a crucible. The pedestal was placed in a bucket that was filled with water and it was introduced into the furnace from the bottom.

The furnace was slowly lowered using the hydraulic pallet lifter release pedal until the crucible was just above the purge gas inlet. At this point, the hydraulic pallet lifter was stopped. The AFROX high purity argon gas was opened from the gas cylinder at a flow rate of 2 L/min, de-moisturized by passing through the crystallized silica gel and de-oxidized by passing through a packing of the copper turnings within the copper tube furnace. The gas was finally introduced into the vertical tube furnace. This purified argon gas served to inert the reduction system and to enhance the reducing efficiency of the reductant within such system. The off-gas extractive system was also turned on at this juncture.

The vertical tube furnace was further slowly lowered until the aluminum tube was submerged approximately 5 mm under the water bath. On average, eight minutes were taken to lower the furnace in order to avoid or minimize the crack-development or breakage of both the crucible and the pedestal due to thermal shock. After the crucible was within the proximity of the hot zone, the Eurotherm 2416 main controller was put back to the run mode, the purge rate was reduced to approximately 500 mL/min and the samples were left inside the furnace for the designated times.

The furnace products were immediately taken out of the furnace after the designated reduction times and they were allowed to cool under an inert atmosphere. The cooled samples were separated into the slag and metallic phases after which they were characterised according to the method that is presented in part (b) and (c) of section 3.3.1.

4. Results and discussion

4.1. Characteristics of the furnace dust

4.1.1. Particle size distribution

The PSD of the furnace dust is depicted in Figure 4.1 after the analysis using the Saturn DigiSizer 5200 V1.10. The data are provided in Table A.3 within the appendix section.

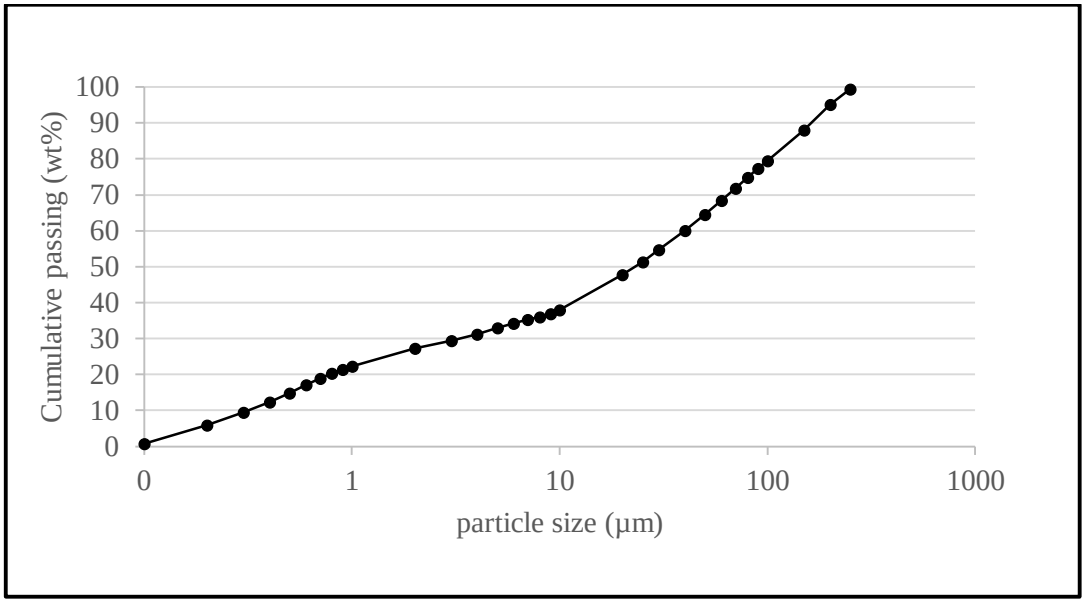

Figure 4.1: A size distribution of a population of particles within the furnace dust on a logarithmic abscissa.

It can be seen from Figure 4.1 that 80% of the particles within the furnace dust had a size less than 100 µm and this indicated that the furnace dust was mainly made up of fines (Sivamohan, 1990; Ansari, 1997). Almost half of such particles within the furnace dust had a size less than 25 µm. To further note from the particle size distribution, 22% of the furnace dust was colloidal (<1 µm) in nature. The arithmetic mean particle size of the interior frequency distribution (+250 µm size range omitted) was calculated from Table A.3 to be 51.20 µm.

A multimodal frequency distribution of particles was also observed from Table A.3. The particles in the size classes 0.1-0.2 µm, 1.0-2.0 µm, 10-20 µm, 30-40 µm and 100-150 µm

exhibited relatively higher frequencies with the particles in the 10-20 µm size class having the highest frequency. This multimodal frequency distribution was attributed to the variations in the extent of production of fumes (both metallic and oxidic) and particulate matter during the smelting cycle inside the electric arc furnaces. Upon condensation and solidification, these fumes often constitute the finer fraction of the furnace dust (Rughubir and Bessinger, 2007). Furthermore, the extent of agglomeration of the particulate matter as the furnace dust was rapidly cooled and settled in the thickener tanks within the Theisen off-gas plant could explain such observed multimodal frequency distribution especially in the relatively larger size classes.

The approximate shape of the particles was examined by use of the TEM technique and the images are depicted in Figure 4.2. The majority of particles appeared to have rounded shape.

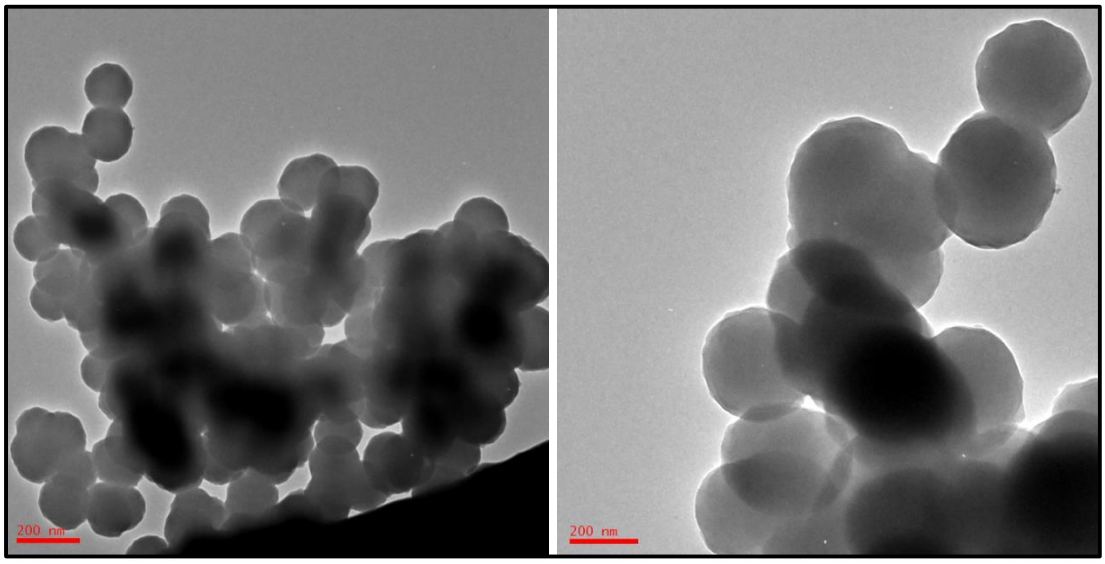

Figure 4.2: The TEM micrographs of the furnace dust highlighting the approximate shape of the particles.

Sometimes bridges were identified at the particles contact points and these bridges consolidated such particles into lumpy structures. The observations from these TEM micrographs further provided some evidence about the possible agglomeration of the particulate matter, which could ultimately explain the observed multimodal frequency distribution of particles.

The fineness of this furnace dust was highly expected because only the small-sized particles and vaporized species have a propensity to be entrained by the escaping furnace off-gas. This

fineness has once again been proven after the work of some previous authors (Cyr, et al., 2000; Rughubir and Bessinger, 2007). It can further be noted that the fineness of this furnace dust was below the optimum size range of most conventional beneficiation techniques (Littler, 1986; Ansari, 1997; Wills, 2006). For this reason, an enrichment of this furnace dust by some conventional physical beneficiation techniques such as electrostatic separators and spiral concentrators may be exceedingly challenging.

4.1.2. Chemical characteristics

The chemical composition of the furnace dust was achieved mainly by the XRF technique and such composition is presented in Table 4.1. The abundance of each element was calculated from the respective oxide abundance. This chemical analysis showed that the furnace dust was dominant in the oxides of titanium (49.39wt% TiO_2) and iron (29.51wt% Fe_2O_3). The impurity oxides explained almost 19wt% of this furnace dust with silica (10.49wt%) and manganese oxide (3.32wt%) contributing the larger fractions.

A comparison of the compositions in Table 4.1 and Table 4.2 shows that the titanium dioxide content of this furnace dust was comparable with that of natural ilmenite. However, a significant difference was observed in the case of the contents of iron and the impurity oxides. The iron content of the furnace dust was relatively lower than that of natural ilmenite by almost 40% while the content of the impurity oxides was much higher within the furnace dust. The amount of both titanium and iron within this furnace dust highlighted the potential of this furnace dust to serve as a supplement feedstock for the production of a titania slag and a metallic iron. The relatively comparable chemical composition of this furnace dust with the previously determined composition by some authors (Cyr et al., 2000; Kudryavskii, 2004; Rughubir and Bessinger, 2007) further provided the consistency of the richness of such furnace dust in the oxides of titanium and iron.

The high content of the impurity oxides within the furnace dust could be directly linked with their abundance in the smelter charge and their behaviour during the reductive smelting. The inefficiencies in the upstream mineral separation processes can inevitably find some amount of the impurity oxides in the smelter charge and Steenkamp (2003) showed that such smelter charge can consist of almost 2wt% of silica as the largest gangue component.

Table 4.1: The chemical composition of the furnace dust as determined by the XRF technique. C was further determined by LECO analysis. L.O.I. refers to loss on ignition.

Species	Chemical composition (wt%)				Element abundance (wt%)			
	Replicate 1	Replicate 2	Mean	STDEV	Replicate 1	Replicate 2	Mean	STDEV
Al_2O_3	1.28	1.25	1.27	0.02	0.68	0.66	0.67	0.01
CaO	0.16	0.16	0.16	0.00	0.12	0.12	0.12	0.00
Cr_2O_3	0.11	0.11	0.11	0.00	0.08	0.08	0.08	0.00
Fe_2O_3	29.44	29.59	29.51	0.11	20.59	20.70	20.64	0.08
K_2O	1.58	1.57	1.58	0.01	1.32	1.30	1.31	0.01
MgO	0.82	0.81	0.82	0.01	0.50	0.49	0.49	0.00
MnO	3.30	3.34	3.32	0.03	2.56	2.58	2.57	0.02
Na_2O	0.78	0.75	0.77	0.02	0.58	0.56	0.57	0.02
P_2O_5	0.18	0.19	0.19	0.01	0.08	0.08	0.08	0.00
SiO_2	10.43	10.55	10.49	0.08	4.88	4.93	4.90	0.04
TiO_2	49.28	49.49	49.39	0.15	29.53	29.66	29.60	0.09
Zn	2.00	1.86	1.93	0.10	2.00	1.86	1.93	0.10
C	0.16	0.16	0.16	0.00	0.16	0.16	0.16	0.00
L.O.I.	0.46	0.15	0.31	0.22	-	-	-	-

Table 4.2: The chemical composition of natural ilmenite from different deposits in the Republic of South Africa (Steenkamp, 2003).

Location	Composition (wt%)			
	TiO_2	Total Fe	Cr_2O_3	V_2O_5
St Lucia	49.00	35.26	0.38	-
Richards Bay	49.70	36.21	0.19	0.29
Umgababa	46.60	37.07	0.10	2.76
Sandy Point	50.30	36.00	0.07	-
Morgan Bay	50.00	38.70	0.05	-
West Coast	41.60	40.28	0.00	0.92
Furnace dust from Table 4.1	49.39	20.64	0.11	-

It was observed that some forms of these impurity oxides such as SiO and Mn are characterized by high vapour pressures (Pesl and Eric, 2002) and they report significantly into the off-gas

stream according to the reactions in Equations 2.4 and 2.5 during the reductive smelting process. The amount of SiO in the off-gas stream is further affected by high temperatures. Between 1527˚C and 1717˚C, the dissociation of silica into SiO and O is very optimal (Bondar et al., 2005). The high vapour pressure of SiO and Mn could therefore explain the relatively larger fractions of SiO_2 and MnO within the furnace dust. Some other impurity oxides together with the oxides of titanium and iron could also report into the off-gas stream as vaporized species and fine particles that were broken due to thermal shock upon entering the hot electric arc attachment zone.

4.1.3. Mineralogical characteristics

An observation from the XRD analysis is illustrated in Figure 4.3. The furnace dust was mainly amorphous and such amorphous content explained 71.0wt% of the furnace dust. The amorphousness of this furnace dust made it very challenging to accurately qualify and quantify the mineral phases that could be present within this furnace dust. However, the identified crystalline mineral phases included ilmenite (20.5wt%), rutile (7.0wt%), quartz (1.0wt%) and iron (0.5wt%). The significant amount of silica within this furnace dust (cf. Table 4.1) and the high temperature synthetic origin of this furnace dust might render the final matrix of such furnace dust vitreous. This vitreous matrix would of course, not satisfy the Bragg's law such that

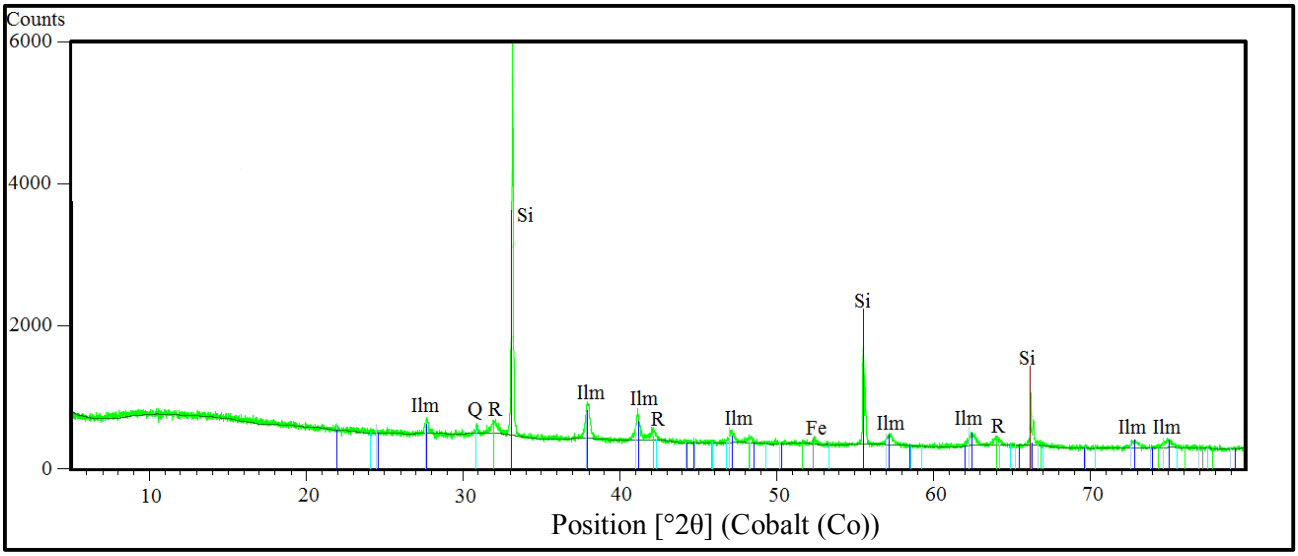

Figure 4.3: An XRD diffractogram of the furnace dust sample. Ilm refers to ilmenite, R refers to rutile, Q refers to quartz.

the mineral phases could be identified. Out of the identified crystalline mineral phases, ilmenite and rutile phases contributed the larger fractions, which corresponded to approximately 70wt% and 24wt% respectively. The remaining balance of such crystalline fraction was explained by small amounts of quartz and iron.

The textures of the mineral phases within the furnace dust were further studied under the scanning electron microscope and the images are shown in Figure 4.4. The Fe-and Ti-bearing ($FeTi$-oxide) grains dominated the matrix of the furnace dust. However, such grains seemed to be strongly affiliated with some impurity oxides. A solid solution of these $FeTi$-oxide grains with the Fe-rich grains was sometimes observed. This solid solution resulted in the $FeTi$-oxide grains occurring as dendrites within the Fe-rich grains and sometimes they were slightly exposed as rims of such Fe-rich grains. These Fe-rich grains also had inclusions of the impurity oxide bearing phases.

Apart from occurring as inclusions within the $FeTi$-oxide and Fe-rich grains, the impurity oxides also occurred interstitially as silicate phases among the $FeTi$-oxide grains and the Fe-rich grains. These silicate phases were rich in silica and some alkali components. However, a significant amount of iron and some amount of titanium was also identified within such silicate phases.

The elemental maps of this furnace dust are illustrated in Figure 4.5 where it can be seen that titanium was distributed at relatively higher amount throughout the sample. In some instances, both titanium and iron were strongly affiliated at higher concentrations. This strong association mostly explained the solid solution between the $FeTi$-oxide grains and the Fe-rich grains that is observed in Figure 4.4. Most impurity species such as silicon, phosphorous, chromium, manganese, potassium and magnesium were distributed evenly throughout the furnace dust sample and this distribution substantiated the observations from Figure 4.4, which highlighted that the impurity oxides occurred as inclusions within the $FeTi$-oxide grains.

The mineral assemblage within this furnace dust rendered such furnace dust a very complex material. This mineral assemblage could further bring to one's attention a challenge that can be associated with enriching this furnace dust with the use of some physical beneficiation

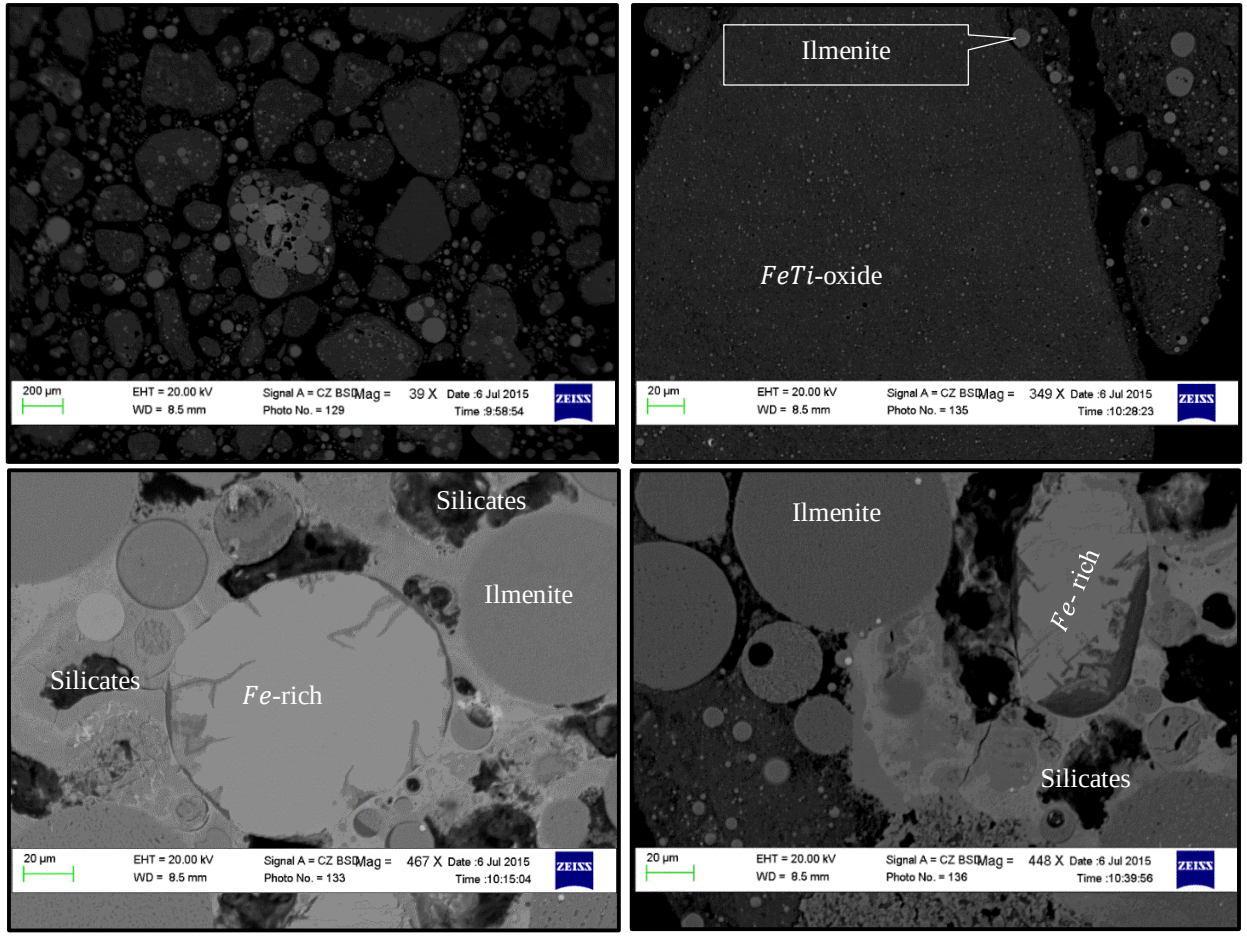

Mineral grain	Na	Mg	Al	Si	K	Ca	Ti	Mn	Fe	Zn	O
$FeTi$-oxide	0.00	0.39	0.58	4.36	1.27	0.00	29.19	2.57	23.59	2.50	35.56
Fe-rich	0.17	0.38	0.42	2.14	0.65	0.00	13.13	1.15	52.03	1.48	28.43
Silicates	0.00	4.37	2.44	18.74	1.86	0.00	1.73	0.00	32.98	0.00	37.87

Figure 4.4: The SEM micrographs of the furnace dust showing the spatial distribution of the mineral grains. The composition is in weight percent.

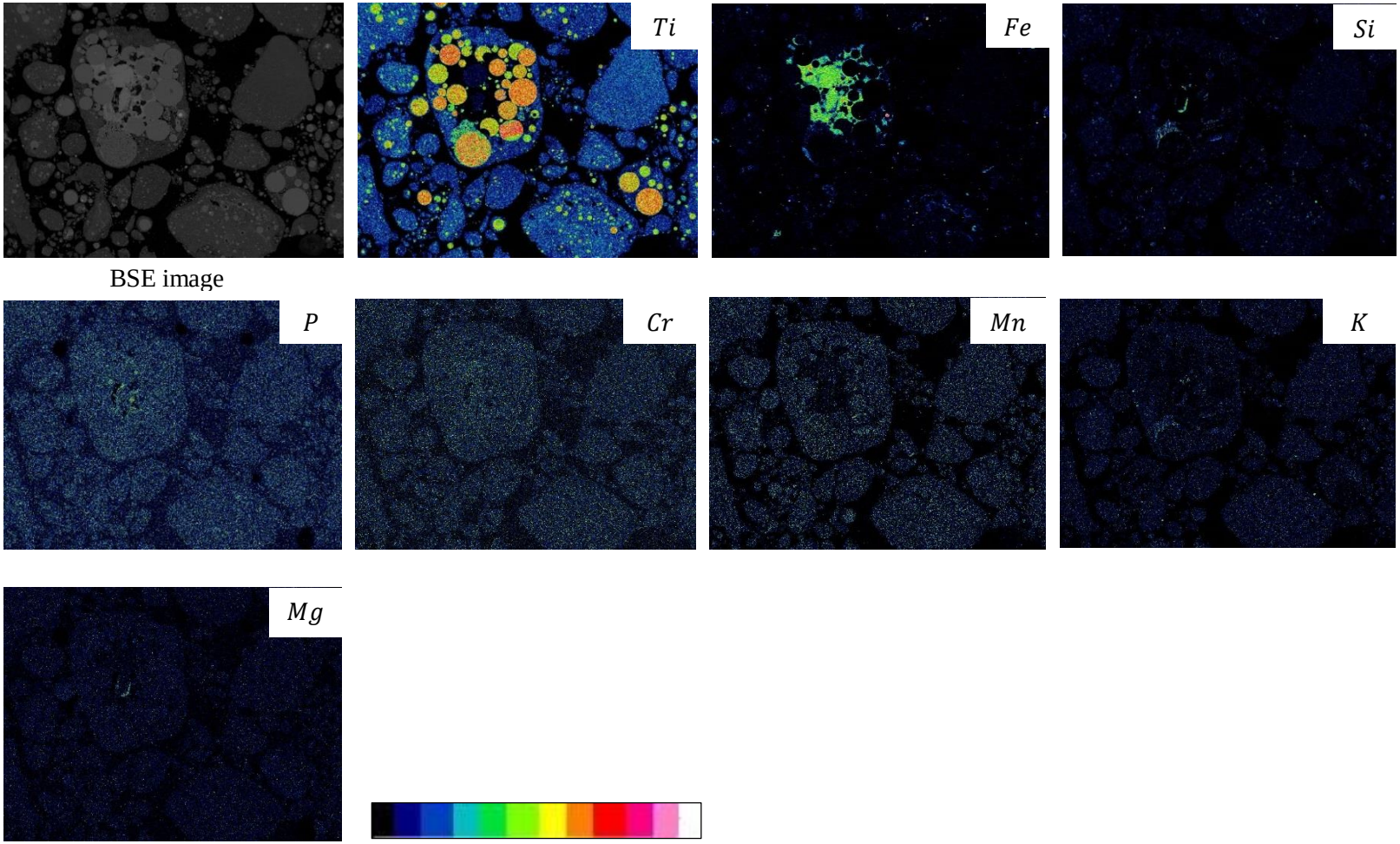

Figure 4.5: The elemental maps of the furnace dust sample. The relative abundance increases from a black to a white colour according to the coloured scale that is provided at the end of the maps. Some elements were distributed at very low abundance and such elements were omitted.

techniques such as the spiral concentrators and electrostatic separators.

4.2. Reduction test work

This section provides the results and discussion of such results for both the simulation modelling and the experimental reduction tests. The possibility of incorporating the furnace dust into the current industrial production of titania slag is also provided. Throughout this test work, it was assumed that titanium was present as only Ti^{3+} and Ti^{4+} within the slag. The impurity oxides were also assumed to occur at the fixed stoichiometry with oxygen. For this reason, some compounds that were predicted by FactSage® 6.4 such as $NaAlO_2$ and CrO were reconciled to the respective oxides of Na_2O, Al_2O_3 and Cr_2O_3. Iron was further assumed to exist as FeO within the slag phase.

4.2.1. Simulation modelling

The FactSage-calculated equilibrium compositions of the slag phase and the metallic phase were obtained and the behaviour of different chemical species during such simulated carbothermic reduction process is depicted in Figure 4.6 to Figure 4.18. The composition of the off-gas stream, from this simulation modelling work, was dominant in carbon monoxide.

(a) Titania in the slag phase

The content of the ${TiO_2}^{eq}$ within the slag phase increased linearly with a decrease of the Ore-C ratio (or an increase of the amount of carbon relative to the amount of the furnace dust). However, this content of the ${TiO_2}^{eq}$ was not significantly influenced by temperature especially from the Ore-C ratio of 15 down to the Ore-C ratio of approximately 9.5. From the Ore-C ratio of 9.5 and below, a significant decrease of the content of the ${TiO_2}^{eq}$ was observed (cf. Figure 4.6). An important observation from Figure 4.6 is that this significant decrease of the content of the ${TiO_2}^{eq}$ from the Ore-C ratio of 9.5 and below, started at relatively lower carbon additions at lower temperatures (1500˚C). However, the more than 85wt% content of the ${TiO_2}^{eq}$ was observed within the slag phase at relatively high carbon additions (Ore-C ratio of 8.7 and below) and at relatively higher temperatures (1650-1700˚C).

At such relatively high amount of carbon, the reduction of titania to metallic phase under the atmosphere that is characterized by the pO_2 below 10^{-8} atm and temperature between 1500˚C and

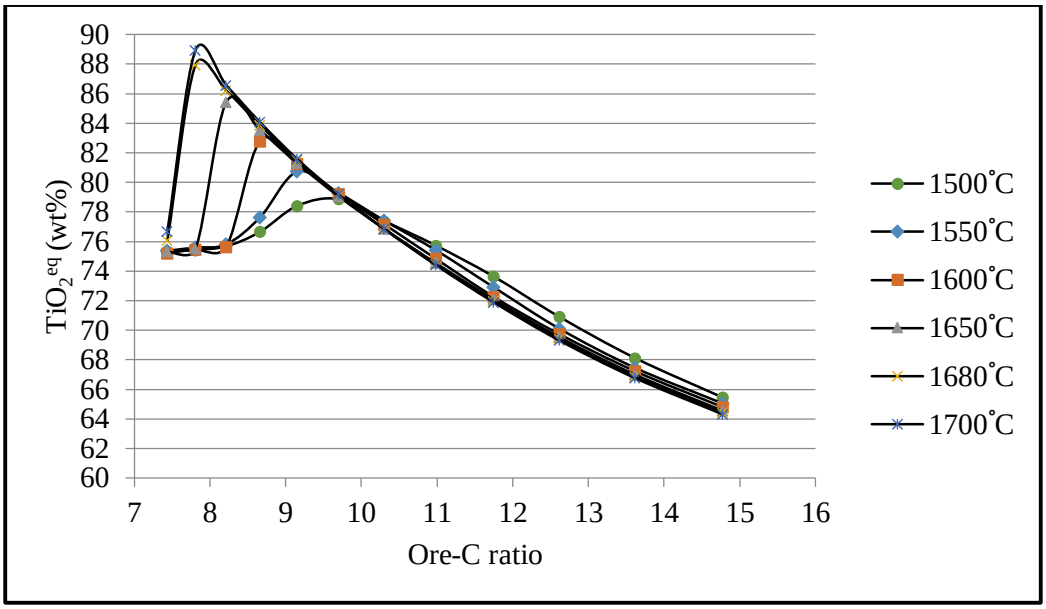

Figure 4.6: The dependence of the $TiO_2{}^{eq}$ content of the slag on the Ore-C ratio and temperature as calculated by FactSage® 6.4.

1700˚C is a very spontaneous and an endothermic process (Pesl and Eric, 1999; Pesl and Eric, 2002). Similar observations were observed in this current study where the decrease of the TiO^{eq} content from the slag phase corresponded to a deportment of titanium into the metallic phase as is depicted in Figure 4.7. It may be noted that this significant reduction of the oxides of titanium from the slag phase is undesirable during the production of titania slags. Pesl and Eric (2002) further highlighted that the gradual disappearance of such titanium oxides occur at slightly less carbon additions when temperature is relatively high because of a strong reduction potential that is exerted by a combined effect of carbon and temperature. In the case of this furnace dust, the relatively high deportment of titanium into the metallic phase at less carbon addition and at relatively lower temperatures, between the Ore-C ratio of 9.5 and 7, seemed to be inconsistent with the observations from Pesl and Eric (2002). Such inconsistency was believed to emanate from the significant amount of silica that was present within the furnace dust as is discussed in the subsequent paragraphs.

Carbon was consumed to reduce a substantial amount of silica to silicon prior to reduction of

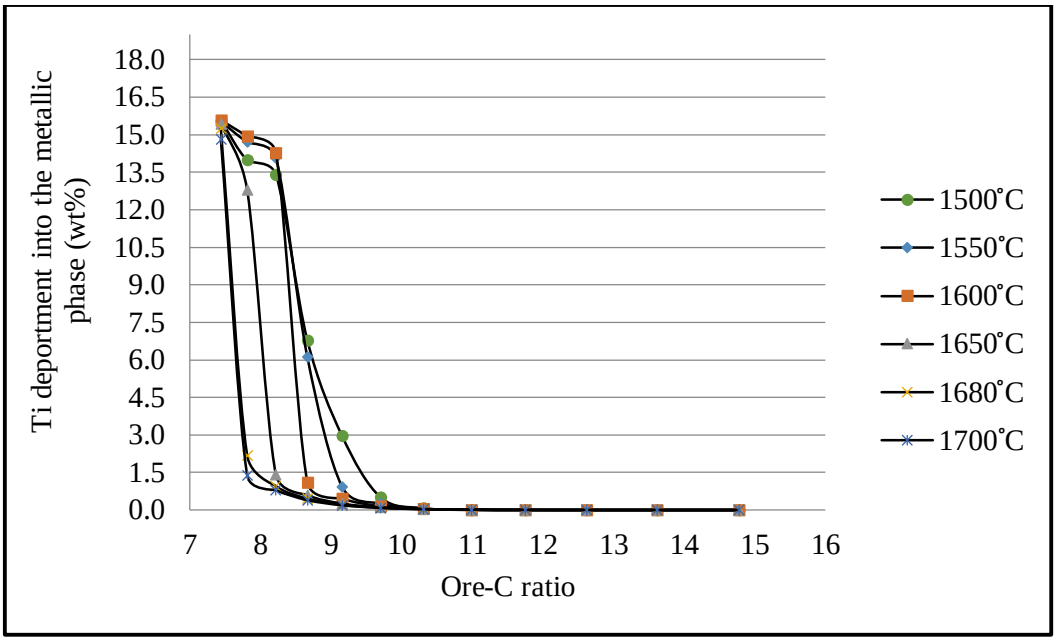

Figure 4.7: The deportment of feed titanium into the metallic phase at different conditions as calculated by FactSage® 6.4.

titania as is depicted in Figure 4.8 and Figure 4.9. It was further observed that a significant deportment of titanium into the metallic phase, which corresponded to the significant decrease of the $TiO_2{}^{eq}$ from such slag phase, resulted in an increase of the silica abundance again within the slag phase and a decrease of silicon abundance from the metallic phase. An increase of the silica abundance within the slag phase could possibly be due to a preferential reduction of titania over silica at those conditions. However, an analysis of the mass of silicon within both the metallic and slag phases showed that such mass decreased from the metallic phase and it increased into the slag phase. This observation was a direct indication of the silicothermic reduction reaction.

The silicothermic reduction reaction is characterized by large, negative enthalpy and an overall enthalpy of the reduction reaction of this furnace dust was found to be negative from the FactSage® 6.4 calculations. At relatively lower temperatures, such silicothermic reduction reaction was therefore thermodynamically favoured and hence the significant decrease of the content of the $TiO_2{}^{eq}$ from the slag phase at relatively lower carbon additions between the Ore-C of 9.5 and 7. A net result of these carbothermic and silicothermic reduction reactions provided a

further possible explanation to an insignificant reduction of silica from the titania slag system as has been reported by some previous authors (Pesl and Eric, 2002; Elstad et al., 2007).

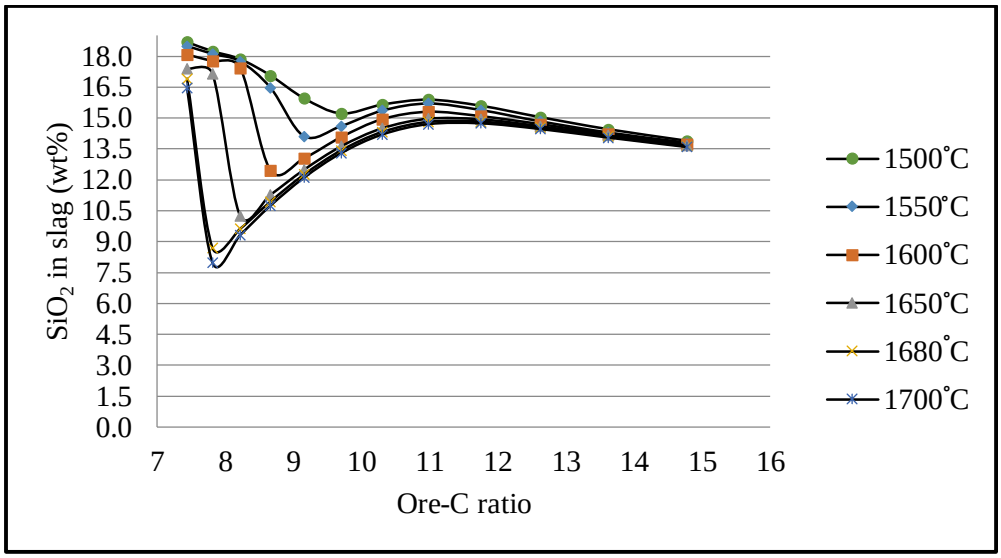

Figure 4.8: The abundance of SiO_2 within the slag phase at different conditions as calculated by FactSage® 6.4.

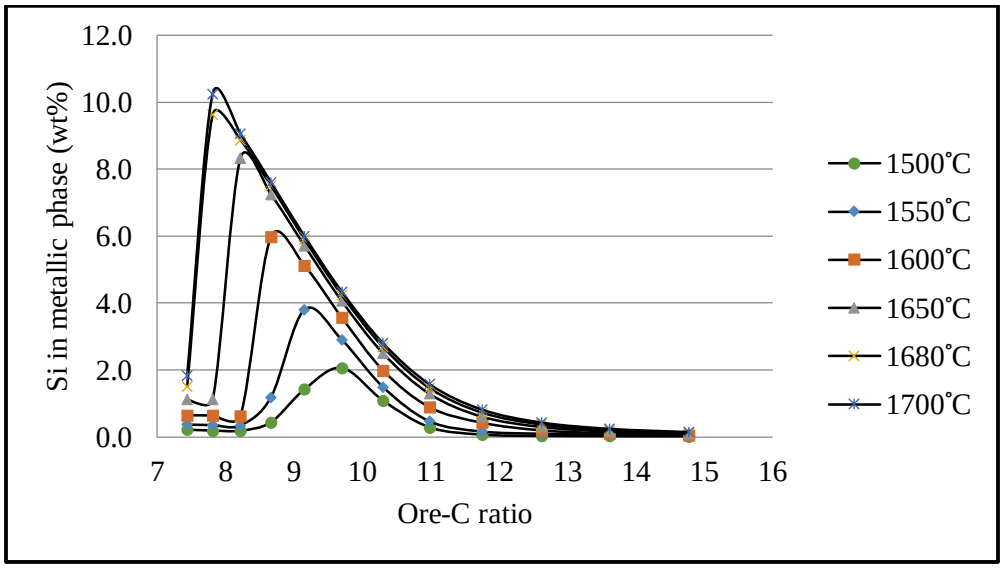

Figure 4.9: The abundance Si within the metallic phase at different conditions as calculated by FactSage® 6.4.

(b) Metallization of iron

The degree of iron metallization also exhibited a linear increase with a decrease of the Ore-C ratio at all temperatures (cf. Figure 4.10). This linear relationship prevailed down to the Ore-C ratio of around 11 when compared to the Ore-C ratio of 9.5 in the case of the $TiO_2{}^{eq}$. Below such Ore-C ratio of 11, the degree of iron metallization showed a slight curvature which ultimately flattened upon approaching a 100% metallization. Such flat region highlighted the maximum achievable metallization of iron from the slag. The dependence of such degree of iron metallization on the Ore-C ratio and temperature also correlated well with the decrease of the abundance of FeO from the slag phase at investigated conditions (cf. Figure 4.11). It was further observed that the Ore-C ratio contributed a larger influence on such degree of iron metallization than temperature.

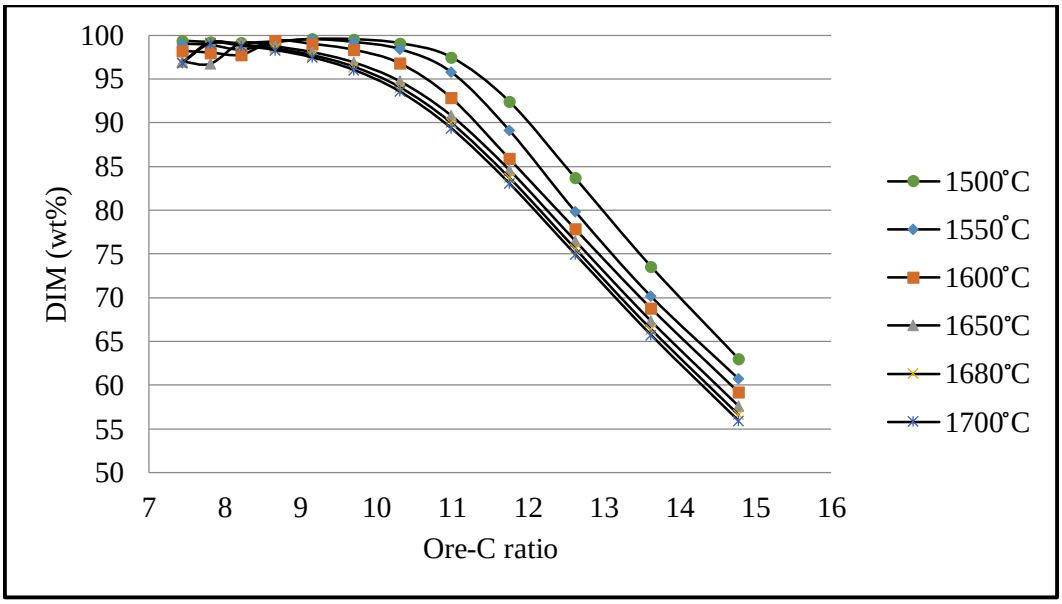

Figure 4.10: The dependence of the degree of iron metallization on the Ore-C ratio and temperature as calculated by FactSage® 6.4.

It was previously observed in section 2.1 that the reduction of iron oxide according to a reaction in Equation 2.1 is the most preferred and the relatively easy reaction to achieve during the upgrading of titania slags. The minor influence of temperature on the extent of reduction of FeO

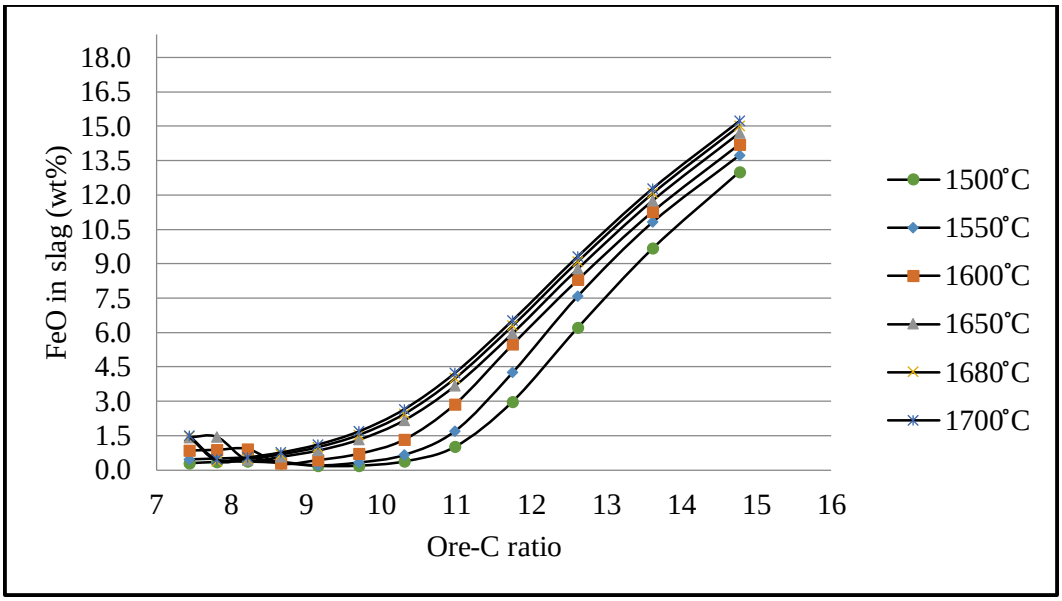

Figure 4.11: The abundance of FeO within the slag phase at different conditions as calculated by FactSage® 6.4.

from the slag phase was further proven after the observations from Pesl and Eric (2002). The reaction in Equation 2.1 is endothermic (Zietsman and Pistorius, 2004), which means that such reaction is more favourable at relatively high temperatures. However, Figure 4.11 highlights that such reduction was more favourable at relatively lower temperatures and this was attributed to the negative overall enthalpy of the carbothermic reduction reaction of the furnace dust.

(c) Impurity oxides in the slag phase

Most of other impurity oxides remained significantly within the slag phase and they occurred mainly as separate silicate phases. MnO and MgO were further incorporated within the PSB structure. Such distribution of the impurity oxides was found to be consistent with the previous observations (Pesl, 1997; Pistorius and Coetzee, 2033; Elstad et al., 2007). The dependence of the abundance of those other impurity oxides on temperature and the Ore-C ratio was found to differ from one oxide to another. However, some oxides showed relatively similar behaviour.

The oxides of alkali metals that were present within the furnace dust showed a similar behaviour to that of silica and the behaviour of such oxides is illustrated in Figure 4.12 and Figure 4.13.

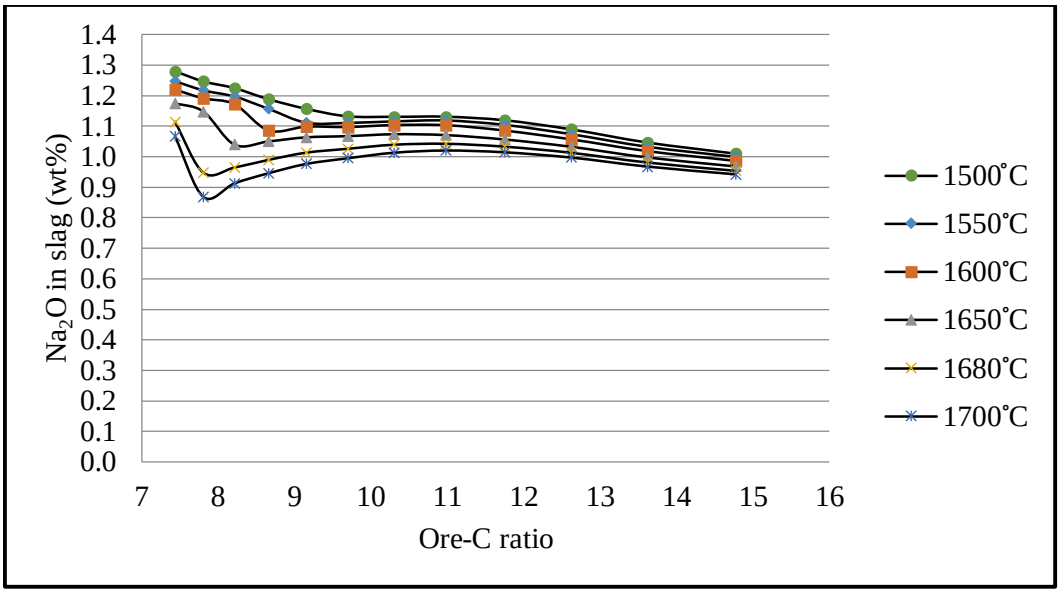

Figure 4.12: The abundance of Na_2O within the slag phase at different conditions as calculated by FactSage® 6.4.

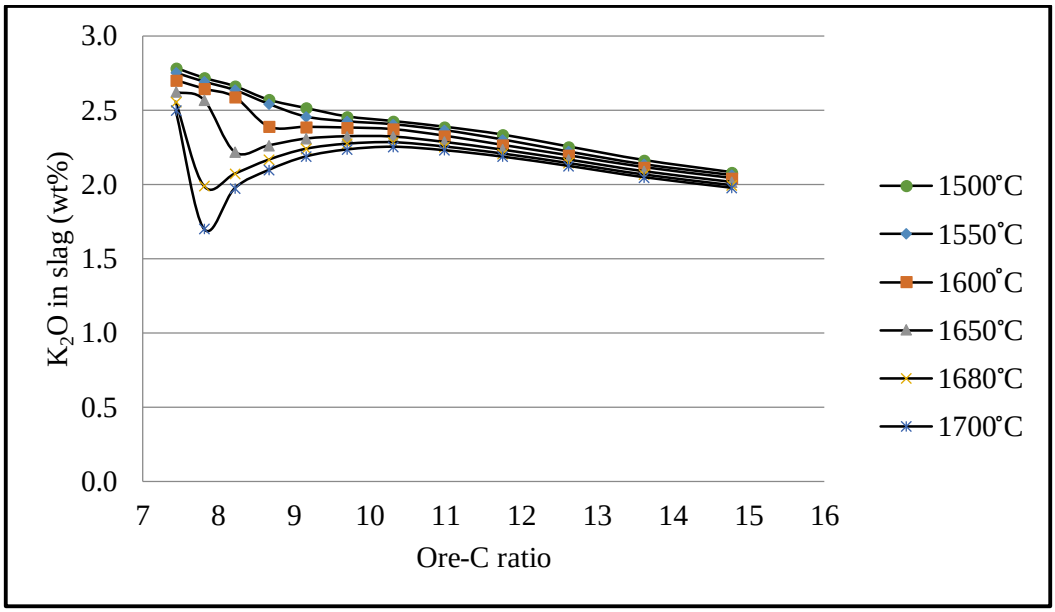

Figure 4.13: The abundance of K_2O within the slag phase at different conditions as calculated by FactSage® 6.4.

However, the reduced species of such oxides did not report into the metallic phase as silicon did. This was possibly because of their high vapour pressure and high reactivity. A possible reduction of such oxides resulted into the respective metals reporting into the off-gas stream. A further observation from Figure 4.12 and Figure 4.13 is that the reduction of sodium oxide and potassium oxide was more feasible at relatively higher carbon addition (Ore-C ratio = 10.3) than silica. An increase of the abundance of such oxides within the slag phase between the Ore-C ratio of 7 and 9.5 corresponded to a significant reduction of titanium oxides at those conditions.

The dependence of the abundances of chromium and manganese on the Ore-C ratio and temperature showed a further closely similar behaviour within both the slag phase and the metallic phase. The behaviour of such species is depicted in Figure 4.14 and Figure 4.15. The reduction of Cr_2O_3 from the slag phase resulted into chromium reporting mainly into the metallic phase as Cr, but insignificantly into the off-gas stream. Manganese also reported into the metallic phase and further into the off-gas stream.

Figure 4.14 and Figure 4.15 further show that the reduction of Cr_2O_3 started at relatively less carbon addition (Ore-C ratio = 12.6) than the reduction of MnO (Ore-C ratio = 11). In addition, the abundance of Cr_2O_3 within the slag seemed to decrease by a larger fraction than that of MnO. These observations agreed well with the ideal thermodynamic ease of reducing Cr_2O_3 relative to reducing MnO (Lee, 1999). However, it can be recalled from section 2.1.4 that the experimental observations show a preferable reduction of MnO over Cr_2O_3 mainly because of the higher vapour pressure of manganese between 1600˚C and 1700˚C (Pesl and Eric, 2002).

A slight decrease of the abundances of Cr and Mn within the metallic phase and the corresponding increase of the abundance of the Cr_2O_3 and MnO within the slag phase between the Ore-C ratios of 7 and 9.5 was mainly due to a significant deportment of titanium into the metallic phase as was seen in Figure 4.7. The masses of Cr and Mn within the metallic phase did not decrease as opposed to that of silicon. This was a further indication that silicothermic reduction reaction might have been the only dominant reaction apart from the carbothermic reduction reaction.

The oxides of calcium, magnesium and aluminium also showed a closely similar behaviour

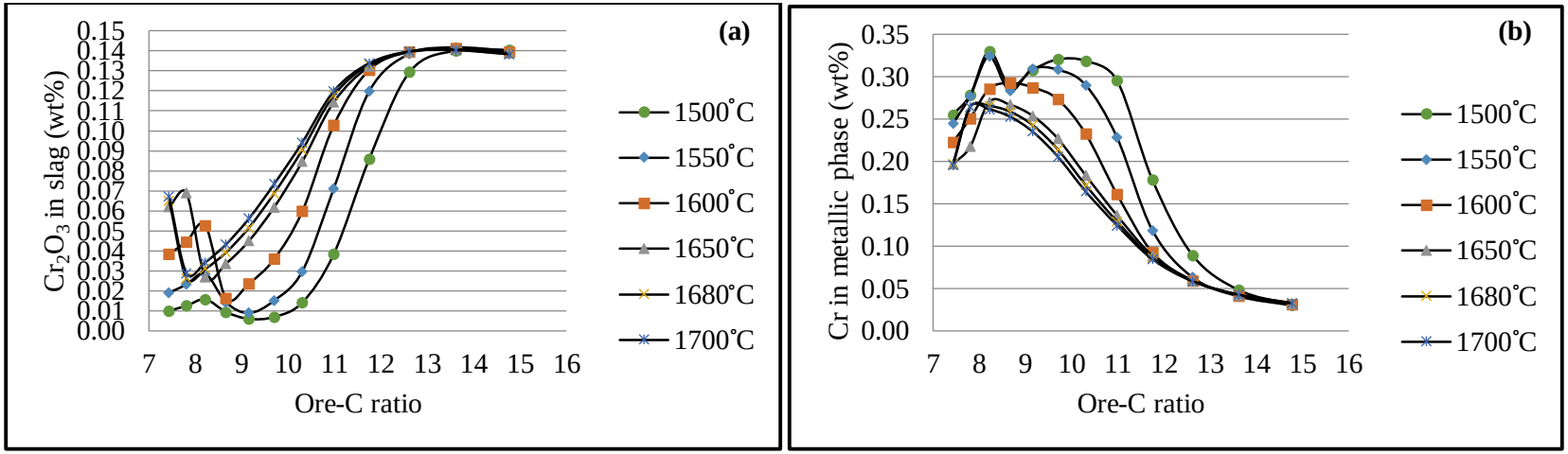

Figure 4.14: The abundance of Cr_2O_3 within the slag phase **(a)** and the abundance of Cr in the metallic phase **(b)** as calculated by FactSage® 6.4.

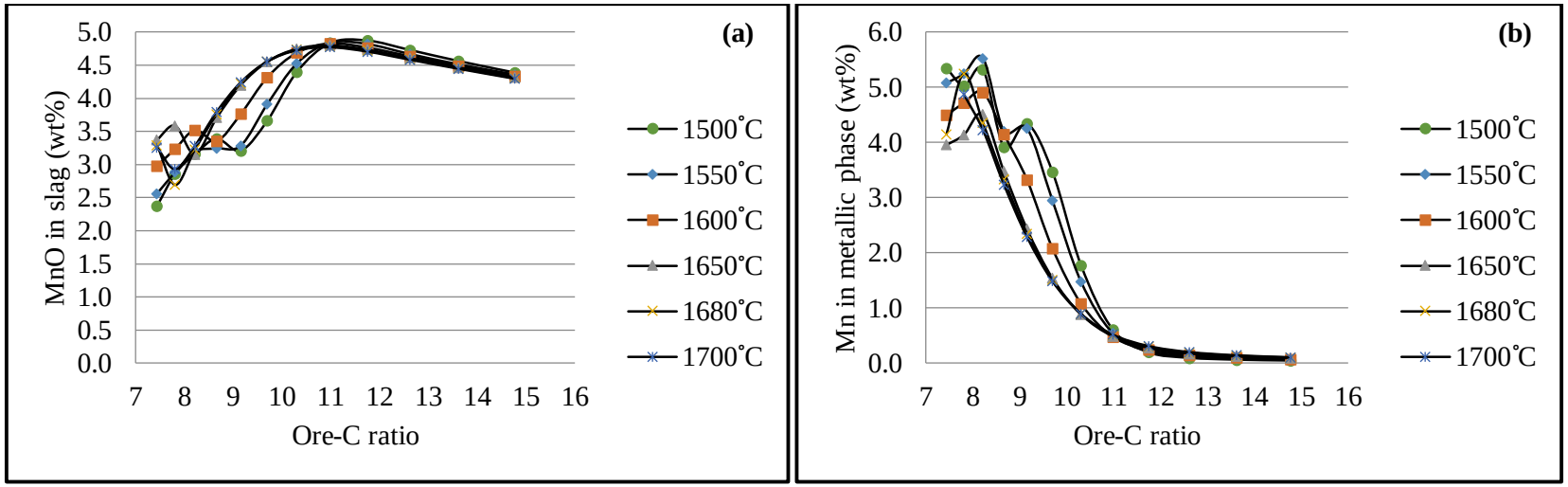

Figure 4.15: The abundance of MnO within the slag phase **(a)** and the abundance of Mn in the metallic phase **(b)** as calculated by FactSage® 6.4.

within the slag phase and the behaviour of such oxides is shown in Figure 4.16 to Figure 4.18. The reduction of such oxides seemed to be insignificant as the abundances of Ca, Mg and Al in either the metallic phase or in the off-gas stream were insignificant. The abundances of such species in the metallic phase or the off-gas stream were in the orders of 10^{-4} wt% and smaller.

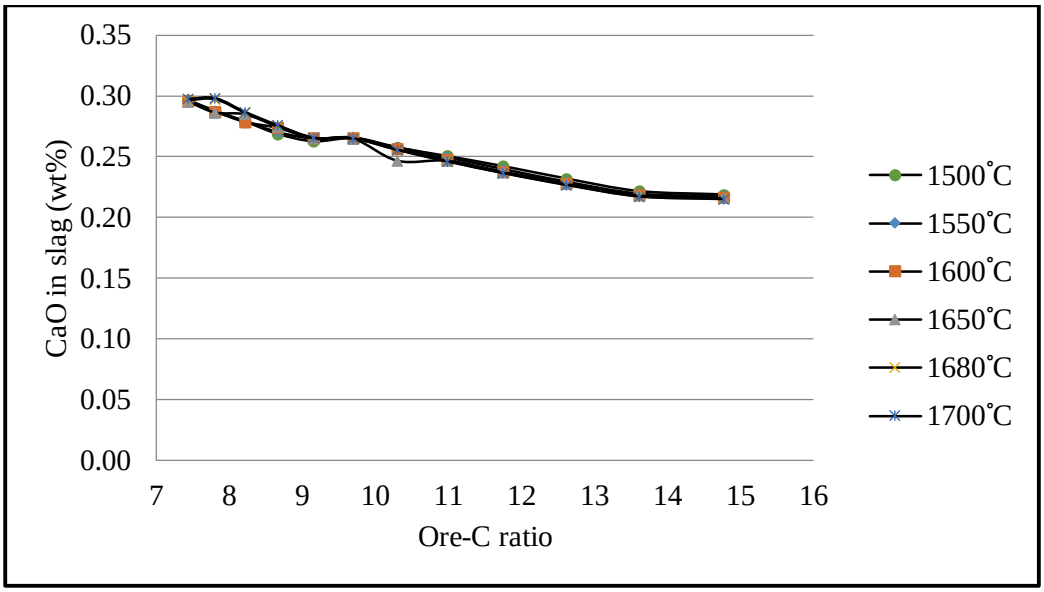

Figure 4.16: The abundance of CaO within the slag phase at different conditions as calculated by FactSage® 6.4.

The abundance of CaO, MgO and Al_2O_3 slightly increased with a decrease of the Ore-C ratio, but temperature seemed to have the least influence on those oxides. The challenge that is associated with removing these oxides from the titania slags during the reduction process is mainly due to the formation of phases that are difficult to reduce (Pesl and Eric, 2002; Elstad et al., 2007; Seim and Kolbeinsen, 2009). The oxides of magnesium and aluminium often interact with the oxides of titanium and iron to form Al-Mg spinel phases that are challenging to reduce (Sommerville and Bell, 1982; Pesl, 1997; Pesl and Eric, 2002). On the other hand, the oxides of calcium interact with titanium oxides to form very stable perovskite phases (Pesl, 1997).

Generally, the simulation work demonstrated the thermodynamic potential of obtaining a titania slag and a metallic iron from the furnace dust. The more than 85wt% content of the ${TiO_2}^{eq}$ was

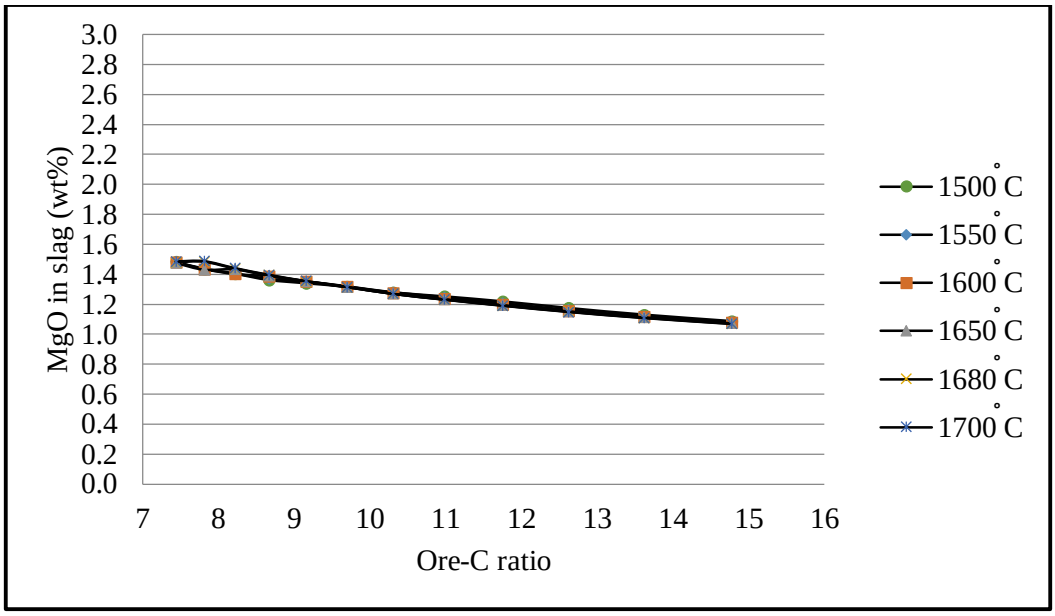

Figure 4.17: The abundance of MgO within the slag phase at different conditions as calculated by FactSage® 6.4.

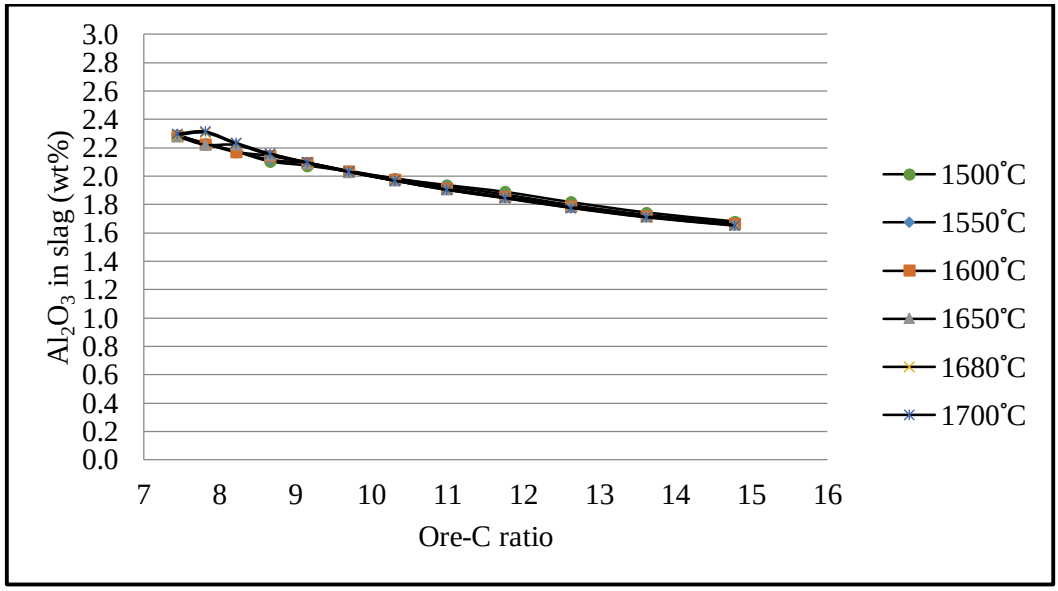

Figure 4.18: The abundance of Al_2O_3 within the slag phase at different conditions as calculated by FactSage® 6.4.

also achieved under high carbon additions (from the Ore-C ratio of 8.7 and below) and at temperatures from 1650˚C to 1700˚C, but it can be noted that the loss of titanium from the slag phase at such strongly reducing conditions was favourable. The feasibility of significantly removing some of the impurity oxides from the slag phase even under such strongly reducing conditions was very low. Such impurity oxides remained mostly within the bulk slag structure as separate silicate phases and sometimes incorporated within the PSB phase.

The more than 90% degree of iron metallization was also achieved at relatively lower carbon additions (Ore-C ratio =11) and this highlighted that the recovery of iron from such furnace dust could be relatively easy. The Ore-C ratio of 9.7 showed the potential of producing a slag with the $TiO_2{}^{eq}$ content that was close to 80wt% with the minimum loss of titanium from the slag phase at all investigated temperatures. This Ore-C ratio was therefore selected and it was used to investigate the experimental production of both a titania slag and a metallic iron from the furnace dust. The results from such experimental reduction tests are provided in the subsequent section.

4.2.2. Experimental reduction tests

The characteristics of the slag phase are initially provided while those of the metallic phase are provided later.

(a) Slag phase

The SEM micrographs that show the spatial distribution of mineral phases within the slag samples and the composition of such mineral phases are shown in Figure 4.19 to Figure 4.26. Magnification of the images that were taken at different sites of the mounted samples was maintained at 900X throughout the analyses. All the micrographs revealed that both the Ti-rich phases and the silicate phases co-existed within the bulk slag structure, but an immiscibility was observed among such phases as was calculated by FactSage® 6.4 and observed by some authors (Pesl, 1997; Pistorius and Coetzee, 2003; Elstad et al., 2007; Pistorius, 2008). Furthermore, the metal globules were identified within the slag samples. Those metal globules appeared relatively brighter within the slag phase due to their higher average atomic number (AAN).

The presence of metal globules within the slag phase is sometimes inevitable because of an occlusion of such metal globules by a viscous slag and an in-situ formation of metallic iron

within the slag phase. Pesl (1997) argued that an in-situ formation of metallic iron within the titania slags is the dominant mechanism and the development of such metallic iron occurs mainly during solidification of slags. This argument was further substantiated by some authors (Pesl and Eric, 1999; Bessinger et al., 2001; Pistorius and Coetzee, 2003; Elstad et al., 2007; Pistorius, 2008), who observed that a co-existence of divalent iron and trivalent titanium is very unstable at below 1350˚C. This instability favours the formation of metallic iron and tetravalent titanium according to the reaction in Equation 2.3, however, in the solid state. In this present study, the size of occluded metal globules were found to be relatively larger than that of the metallic iron globules that formed in-situ within the slag phase.

A conversion of the composition of the Ti-rich and the silicate phases from elemental abundances to oxide abundances was achieved with the use of Equations A.6 to A.8. Such equations were applied to the data that was generated by the SEM-EDS only because of the ability of such analytical technique to measure the oxygen concentration independently. The relative abundances of such oxides are presented in Table 4.3 to Table 4.9 and they are compared to the calculations from FactSage® 6.4.

A slag sample that was produced at 1650˚C for a reduction time of 2 minutes showed that the Ti-rich phases were mainly elongated and the silicate phases occurred interstitially among such Ti-rich phases (cf. Figure 4.19). Sometimes such Ti-rich phases were associated with white speckles that suggested the presence of a solid solution of a metallic phase with the Ti-rich phases. This observation seemed to be similar to the observation in Figure 4.4 and it highlighted an incomplete exsolution between the metallic phase and the Ti-rich phases.

An interesting feature was the manner in which the small metallic iron globules that formed in-situ within such slag sample were distributed. Those small metallic iron globules had the maximum diameter of 20 µm and they existed in the middle of the Ti-rich phases or at the grain boundaries of such Ti-rich phases and the silicate phases. This distribution seemed to be consistent with the observations from Gueguin and Cardarelli (2007) and Bessinger (2000).

The composition of the Ti-rich phases in Table 4.3 shows that such phases were made up of mainly trivalent titanium and less of tetravalent titanium. An equivalent titanium dioxide content

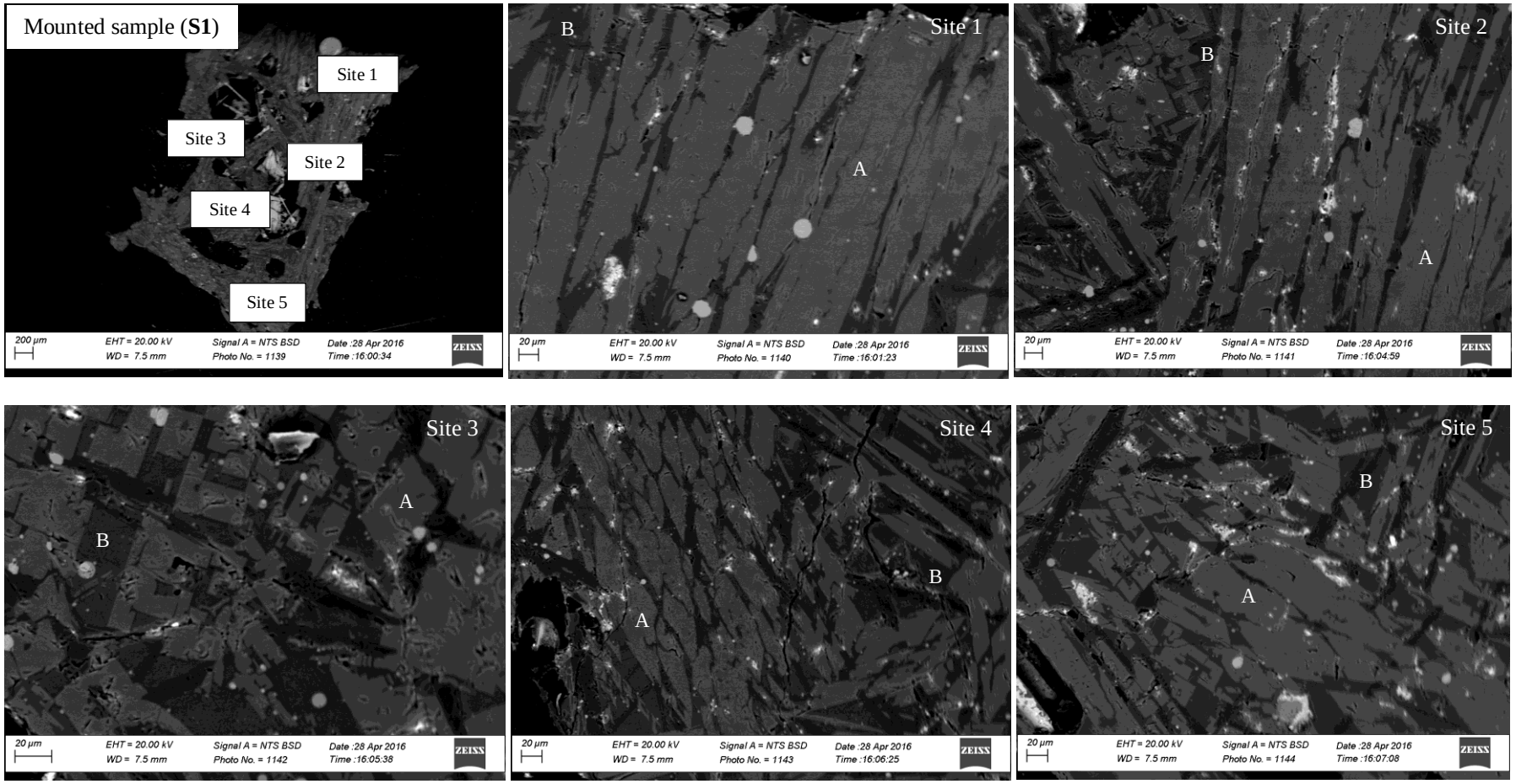

Phase	Na	Mg	Al	Si	P	K	Ca	Ti	Cr	Mn	Fe	Zn	O	C
Ti-rich (A)	0.00	0.05	9.22	0.00	0.00	0.00	0.00	49.46	0.00	0.00	0.00	0.00	41.27	-
Silicates (B)	0.62	1.48	14.82	19.57	0.00	4.12	0.59	4.48	0.08	10.41	0.34	0.00	43.78	-
Metal globules (white)	0.00	0.00	0.00	0.62	0.00	0.00	0.00	1.53	1.04	1.55	94.29	0.00	0.75	0.22

Figure 4.19: The SEM micrographs of titania slag, **S1**, sample that was produced from the furnace dust at 1650˚C for 2 min. The Ore-C ratio was 9.7 and the composition is in weight percent.

of 82.5wt% was observed in such Ti-rich phases. The iron oxide and other impurity oxides, except alumina, were insignificant within such Ti-rich phases. However, such oxides of iron and other impurity species were identified within the silicate phases. The impurity oxides explained almost 92.7wt% within such silicate phases.

Table 4.3: The composition of the **S1** sample that was produced at 1650˚C for 2 min as determined by the SEM-EDS and XRF techniques. The composition is in weight percent.

Phase	Na_2O	MgO	Al_2O_3	SiO_2	P_2O_5	K_2O	CaO	Ti_2O_3	TiO_2	Cr_2O_3	MnO	FeO	$TiO_2{}^{eq}$
Ti-rich	0.00	0.09	17.42	0.00	0.00	0.00	0.00	55.74	20.57	0.00	0.00	0.00	82.52
FactSage	0.81	1.50	0.88	4.71	0.00	0.62	0.30	58.21	26.15	0.07	5.22	1.52	90.84
Silicates	1.11	2.79	27.73	40.50	0.00	5.25	0.83	5.31	1.56	0.23	15.61	0.52	7.47
FactSage	2.75	0.11	9.48	71.55	0.00	13.41	0.00	0.00	2.48	0.00	0.21	0.01	2.48
Bulk sample	0.24	1.28	2.05	16.79	0.01	1.90	0.33	47.87	17.67	0.09	4.78	6.99	70.87
FactSage	1.07	1.31	2.03	13.62	0.00	2.32	0.26	50.45	22.99	0.06	4.56	1.32	79.06

Alumina exhibited a significant abundance in both the Ti-rich and the silicate phases. A raw data for the bulk composition of such slag sample further confirmed the high amount of alumina within the **S1** sample (cf. Table A.6) and it was ultimately identified that the source of such alumina was the gas outlet ceramic pipe that was attacked by the slag (cf. Figure A.6). This amount of alumina falsely underestimated the abundance of other oxides within the **S1** sample. The reconciled and normalized bulk composition of such **S1** sample was therefore achieved and it is included in Table 4.3. The details regarding such reconciliation of bulk compositions are provided within the appendix section along with Table A.6.

A comparison of the experimental compositions of the Ti-rich and silicate phases to the FactSage® 6.4 calculations shows significant differences in terms of most oxides, but the comparable abundances in terms of Ti_2O_3 and TiO_2 in the Ti-rich phases were observed. The reconciled and normalized bulk composition of the **S1** sample was comparable with the composition that was calculated by FactSage® 6.4. However, the abundances of silica and iron oxide were relatively higher than the FactSage-calculated values. This resulted in the achievable equivalent titanium dioxide content of only 70.87wt% as opposed to the 79.06wt% that was calculated by FactSage® 6.4. The relatively higher amount of bulk iron within such slag sample

was in line with the possible solid solution between a metallic phase and the Ti-rich phases that was observed in the micrographs.

The micrographs of a slag sample that was produced at a slightly longer reduction time than the **S1** sample, still at 1650˚C, are illustrated in Figure 4.20. The abundances of the oxides within such slag sample are presented in Table 4.4. The occluded metal globules were identified within this **S2** sample and the maximum diameter of such occluded globules reached approximately 800 µm (0.8 mm). The relatively higher amount of bulk FeO within this **S2** sample and other slag samples as determined by the XRF technique (cf. Table A.6) was therefore attributed to such occluded metal globules. The maximum size of the small metallic iron globules that formed in-situ within the slag phase was 40 µm, which was almost twice the maximum size of the metallic iron globules within the **S1** sample. Of interest to note was that the white speckles that were mostly affiliated with the Ti-rich phases within the **S1** sample were no longer dominant within the **S2** sample. These observations highlighted the progressive growth of the metal globules with increasing reduction time and hence an exsolution between the slag and the metallic phases.

The mineral textures within this **S2** sample showed a deviation from the textures that were observed within the **S1** sample. The Ti-rich phases showed an elongated shape in some sites, which was not as dominant as was observed within the **S1** sample. The shape of such Ti-rich phases was becoming more rounded and the silicate phases were interruptedly dispersed within such Ti-rich phases. A prolonged mixing that was possibly initiated by the escaping gas and the transfer of the chemical species between the Ti-rich and silicate phases provided a possible explanation to such spatial distribution of the mineral phases that was different from those within the **S1** sample.

The composition of such Ti-rich phases was richer in titanium than the Ti-rich phases within the **S1** sample (cf. Table 4.3 and Table 4.4). The presence of FeO in the Ti-rich phases within the **S2** sample was still insignificant as was the case with the Ti-rich phases within the **S1** sample. However, the oxides of magnesium and manganese were identified and the abundances of such oxides were very close to the FactSage-calculated abundances. Apart from the oxides of MgO and MnO, most impurity oxides were insignificantly distributed in such Ti-rich phases, but those

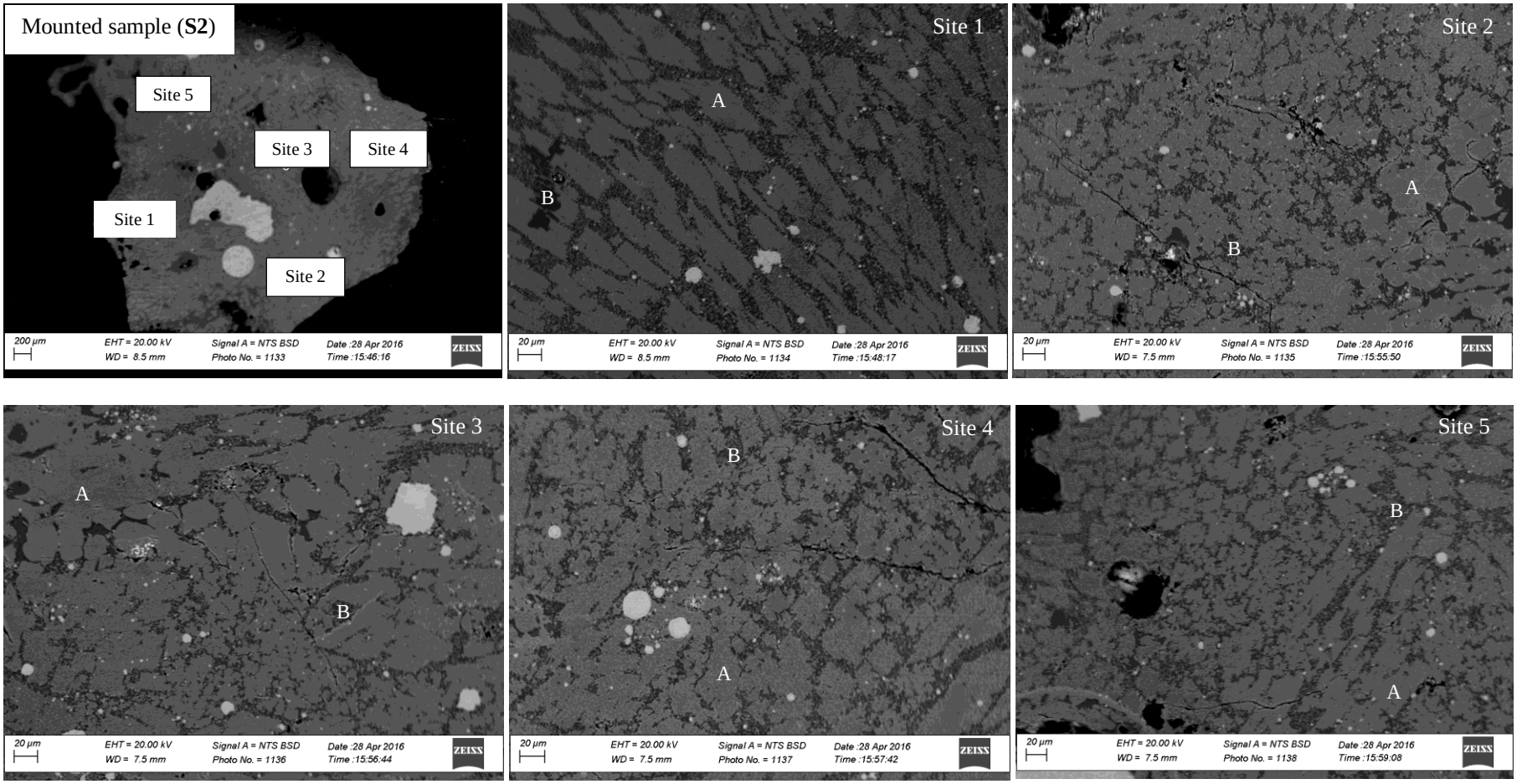

Phase	Na	Mg	Al	Si	P	K	Ca	Ti	Cr	Mn	Fe	Zn	O	C
Ti-rich (A)	0.00	0.93	0.19	0.00	0.00	0.00	0.00	56.82	0.00	2.57	0.00	0.00	39.49	-
Silicates (B)	0.64	1.03	4.45	27.92	0.00	4.01	1.27	5.91	0.00	9.60	0.33	0.00	44.84	-
Metal globules (white)	0.00	0.00	0.00	3.33	0.00	0.00	0.00	3.46	0.24	2.04	90.31	0.00	0.41	0.21

Figure 4.20: The SEM micrographs of titania slag, **S2**, sample that was produced from the furnace dust at 1650˚C for 4 min. The Ore-C ratio was 9.7 and the composition is in weight percent.

impurity oxides significantly remained in the silicate phases with their fraction being around 90.4wt% in such silicate phases.

Table 4.4: The composition of the **S2** sample that was produced at 1650˚C for 4 min as determined by the SEM-EDS and XRF techniques. The composition is in weight percent.

Phase	Na_2O	MgO	Al_2O_3	SiO_2	P_2O_5	K_2O	CaO	Ti_2O_3	TiO_2	Cr_2O_3	MnO	FeO	$TiO_2{}^{eq}$
Ti-rich	0.00	1.54	0.37	0.00	0.00	0.00	0.00	64.04	23.63	0.00	3.31	0.00	94.80
FactSage	0.81	1.50	0.88	4.71	0.00	0.62	0.30	58.21	26.15	0.07	5.22	1.52	90.84
Silicates	0.86	1.71	8.41	59.73	0.00	4.83	1.77	6.67	2.45	0.26	12.40	0.43	9.87
FactSage	2.75	0.11	9.48	71.55	0.00	13.41	0.00	0.00	2.48	0.00	0.21	0.01	2.48
Bulk sample	0.16	1.34	2.80	15.69	0.06	1.53	0.32	51.92	19.17	0.14	4.75	2.11	76.87
FactSage	1.07	1.31	2.03	13.62	0.00	2.32	0.26	50.45	22.99	0.06	4.56	1.32	79.06

The experimentally observed composition of such Ti-rich and silicate phases further showed significant differences when compared to the FactSage® 6.4 calculations, but that was not the case with the bulk composition of the slag sample. The bulk composition of the **S2** sample was comparable to the FactSage-calculated composition. The content of the equivalent titanium dioxide within the **S2** sample was 76.87wt%, which was relatively higher than the 70.87wt% content of the equivalent titanium dioxide that was observed within the **S1** sample. Such increase of the content of the equivalent titanium dioxide within the **S2** sample corresponded to a decrease of the abundances of FeO, SiO_2 and MnO when compared to the **S1** sample. The decrease of the abundances of SiO_2 and MnO from the slag phase corresponded to an increase of the abundances of Si and Mn within the metallic phase as will be seen later in Table 4.11

An elongated shape of the Ti-rich phases was once again observed for the slag sample that was produced at 1650˚C for 6 minutes after the **S1** sample (cf. Figure 4.19 and Figure 4.21). However, the Ti-rich phases within the **S3** sample were thinner than those within the **S1** sample. A further observation regarding the mineral textures within the **S3** sample was that the maximum size of the metallic iron globules that formed in-situ within the slag phase was 40 µm. Such size was comparable to the maximum size within the **S2** sample, but larger than the maximum size within the **S1** sample. The white speckles that were associated with the Ti-rich phases within the

S1 sample were also no longer noticeable.

The Ti-rich phases within the **S3** sample showed the comparable content of the equivalent titanium dioxide with those within the **S2** sample, but higher than those within the **S1** sample. The FeO and SiO_2 made the first appearance in the Ti-rich phases within such **S3** sample and such transfer of FeO and SiO_2, together with some Al_2O_3, resulted into a slight decrease of the MgO and MnO abundances when compared to the **S2** sample. The silicate phases, on the other hand, were made up of 88.2% impurity oxides and such fraction was comparable with the 92.7% within the **S1** sample and 90.4% within the **S2** sample. However, it is worth noting that there had been a gradual decrease of such fraction of the impurity oxides in those silicate phases with increasing reduction time. This gradual decrease of the fraction of such impurity oxides was found to correspond to the gradual increase of the abundance of the total titanium dioxide in such phases. Another possible reason behind this gradual decrease of the fraction of such impurity oxides was a reduction into the metallic phase and volatilization of some impurity species such as K, Na, Mn and SiO into the off-gas stream.

Table 4.5: The composition of the **S3** sample that was produced at 1650˚C for 6 min as determined by the SEM-EDS and XRF techniques. The composition is in weight percent.

Phase	Na_2O	MgO	Al_2O_3	SiO_2	P_2O_5	K_2O	CaO	Ti_2O_3	TiO_2	Cr_2O_3	MnO	FeO	${TiO_2}^{eq}$
Ti-rich	0.00	0.30	2.56	0.89	0.00	0.00	0.00	64.71	23.88	0.00	0.32	0.17	95.80
FactSage	0.81	1.50	0.88	4.71	0.00	0.62	0.30	58.21	26.15	0.07	5.22	1.52	90.84
Silicates	0.37	2.95	29.31	43.57	0.00	4.00	0.00	6.68	2.46	0.00	0.00	1.59	9.89
FactSage	2.75	0.11	9.48	71.55	0.00	13.41	0.00	0.00	2.48	0.00	0.21	0.01	2.48
Bulk sample	0.17	1.37	2.10	17.30	0.05	1.77	0.38	50.61	18.69	0.09	4.66	2.82	74.93
FactSage	1.07	1.31	2.03	13.62	0.00	2.32	0.26	50.45	22.99	0.06	4.56	1.32	79.06

The significantly high abundance of alumina was once again observed after the observations from the **S1** sample. However, most of alumina remained in the silicate phases as opposed to the observations within the **S1** sample. It was therefore inferred that an immiscibility between the Ti-rich phases and the silicate phases was more feasible at relatively longer reduction times.

The reconciliation of such alumina abundance, in a similar manner to the abundance within the

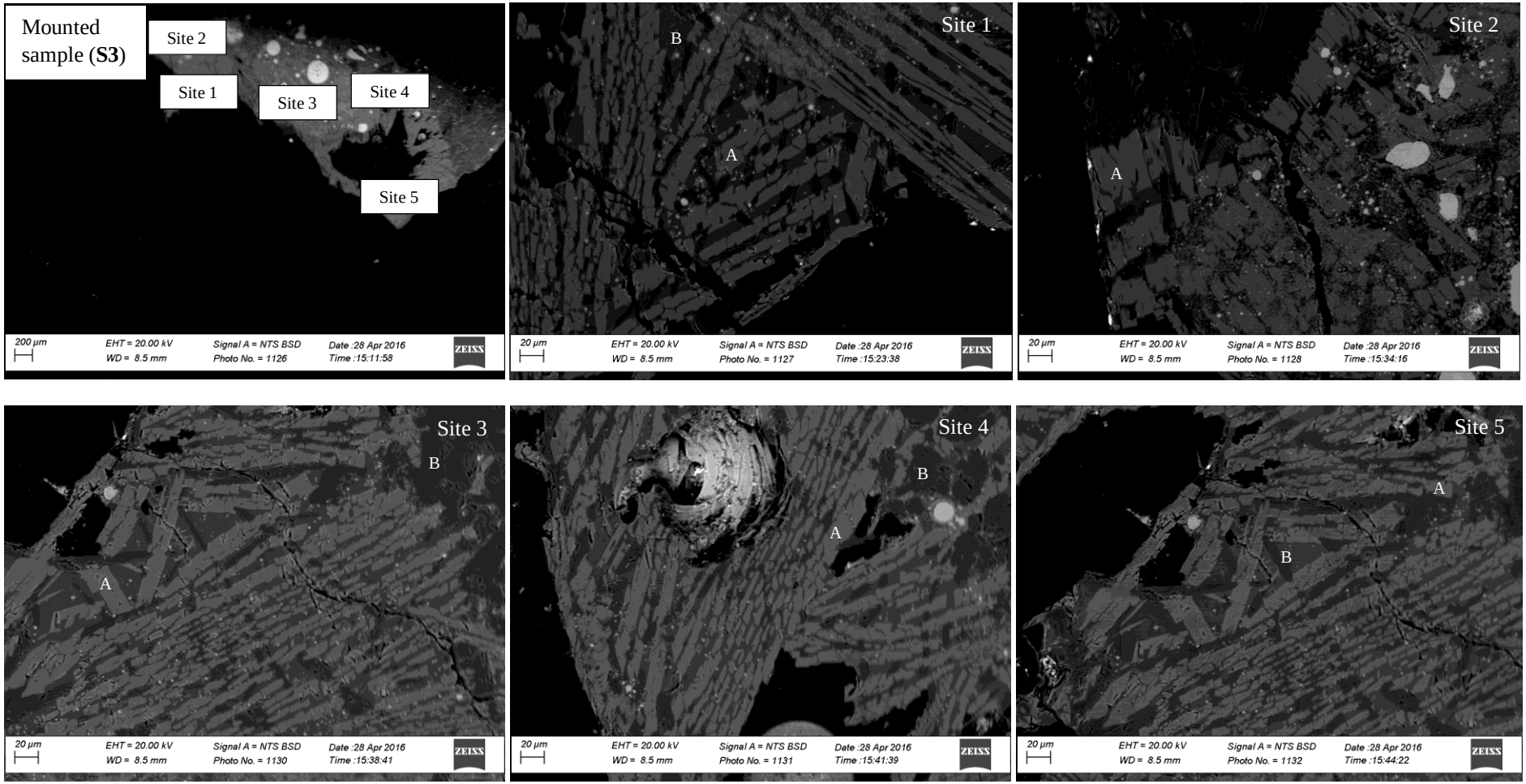

Phase	Na	Mg	Al	Si	P	K	Ca	Ti	Cr	Mn	Fe	Zn	O	C
Ti- rich (A)	0.00	0.18	1.35	0.42	0.00	0.00	0.00	57.41	0.00	0.25	0.13	0.00	40.26	-
Silicates (B)	0.27	1.78	15.51	20.37	0.00	3.32	0.00	5.93	0.00	7.68	0.00	0.00	45.14	-
Metal globules (white)	0.00	0.00	0.00	3.71	0.00	0.00	0.00	0.55	0.30	2.37	92.04	0.00	0.74	0.29

Figure 4.21: The SEM micrographs of titania slag, **S3**, sample that was produced from the furnace dust at 1650˚C for 6 min. The Ore-C ratio was 9.7 and the composition is in weight percent.

S1 sample, provided the normalized bulk composition of such **S3** sample with an equivalent titanium dioxide content of 74.93%. Such content of the equivalent dioxide was slightly lower than the 76.87wt% that was observed within the **S2** sample, but higher than the 70.87wt% that was observed within the **S1** sample. The decrease of the equivalent titanium dioxide content within this **S3** sample corresponded to a significant increase of the silica abundance again after the observations from the **S1** sample.

The slag samples that were produced for longer reduction times than 6 minutes showed a significant coalescence and enlargement of the Ti-rich phases as can be seen in Figure 4.22 and Figure 4.23. Such significant degree of coalescence and subsequent enlargement of the Ti-rich phases seemed to be consistent even at 1600˚C and 1500˚C (cf. Figure 4.25 and Figure 4.26).

A coalescence and hence an enlargement of particles of any material, is strongly affected by the surface or an interfacial tension of such material. The surface or interfacial tension is, in essence, the net cohesive force that is created by atoms within the bulk of a material on the atoms that are on the surface of such material. To be precise, a ‘‘surface’’ tension is a term that is used when one of the two phases is a gas and an ‘‘interfacial’’ tension is a term that is used when the phases are in liquid or solid states (Keene, 1995). For this reason, it might be correct to use an interfacial tension for metallurgical melts such as slags and molten metallic phases.

An interfacial tension of the titania-rich slags is assumed to lie between 250 mN/m and 400 mN/m (Keene, 1995; Pistorius and Coetzee, 2003). A significantly higher interfacial tension of such slags when compared to the 73 mN/m of water (Perry et al., 1997) provided a solid inference that the interfacial tension of the Ti-rich phases was the major driving force to consolidate such phases into larger grains. In addition, such coalescence occurred after the almost complete reduction of iron oxides from the slag phase (cf. Figure A.5) and this observation seemed to be consistent with the theoretical background from Keene (1995) who stated that such interfacial tension could approach zero during the progression of reactions or generally, when the system is not under equilibrium.

The consistent coalescence and hence enlargement of the Ti-rich phases even at relatively lower temperatures (cf. Figure 4.25 and Figure 4.26) indirectly indicated an insignificant dependence

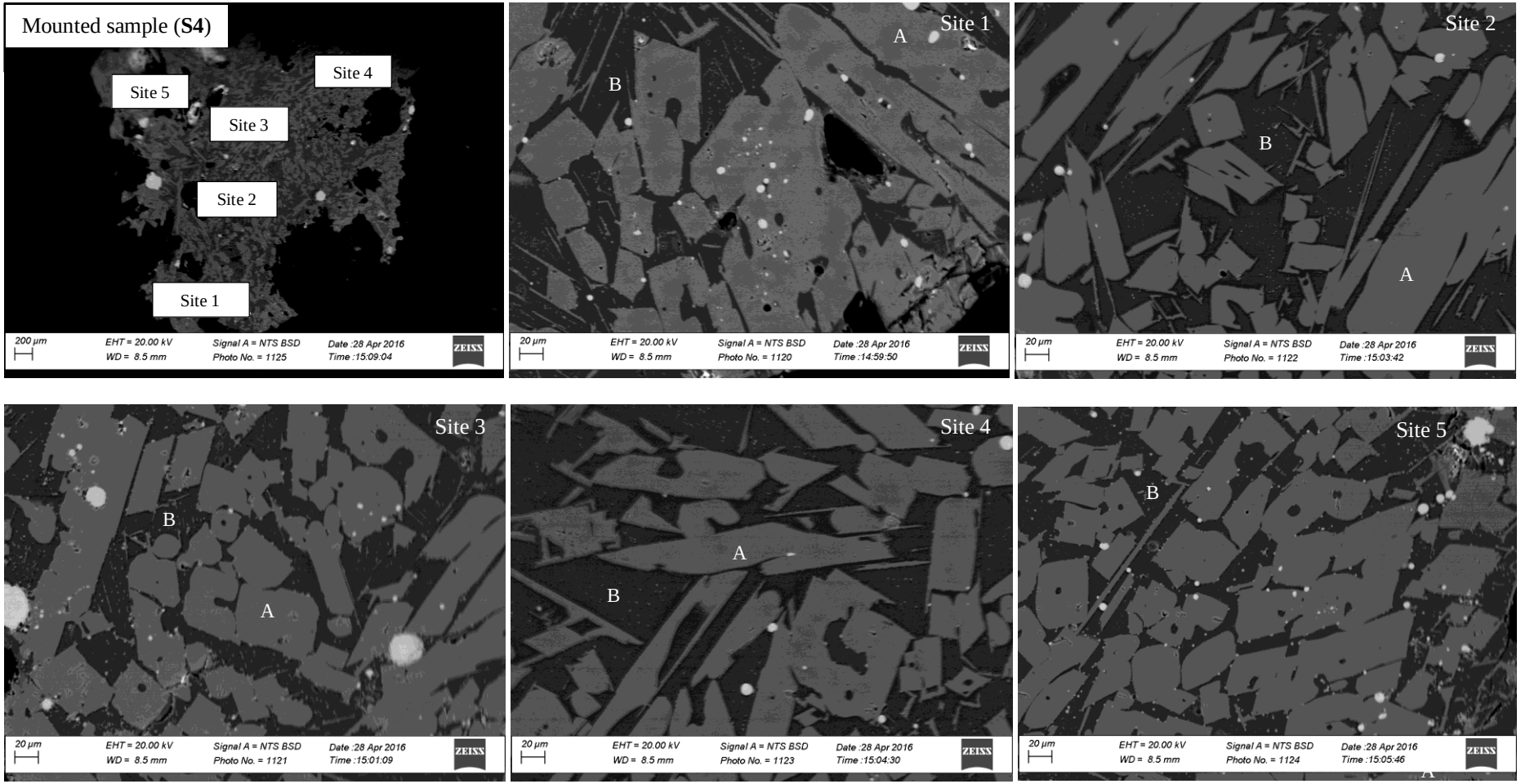

Phase	Na	Mg	Al	Si	P	K	Ca	Ti	Cr	Mn	Fe	Zn	O	C
Ti-rich (A)	0.00	0.65	0.44	0.48	0.00	0.34	0.00	56.57	0.00	1.58	0.18	0.00	39.74	-
Silicates (B)	1.09	1.32	4.02	27.29	0.00	8.48	0.59	6.12	0.00	6.73	0.34	0.00	44.03	-
Metal globules (white)	0.00	0.00	0.00	0.00	0.00	0.00	0.00	1.66	0.28	0.49	96.41	0.00	0.81	0.35

Figure 4.22: The SEM micrographs of the titania slag, **S4**, sample that was produced from the furnace dust at 1650˚C for 8 min. The Ore-C ratio was 9.7 and the composition is in weight percent.

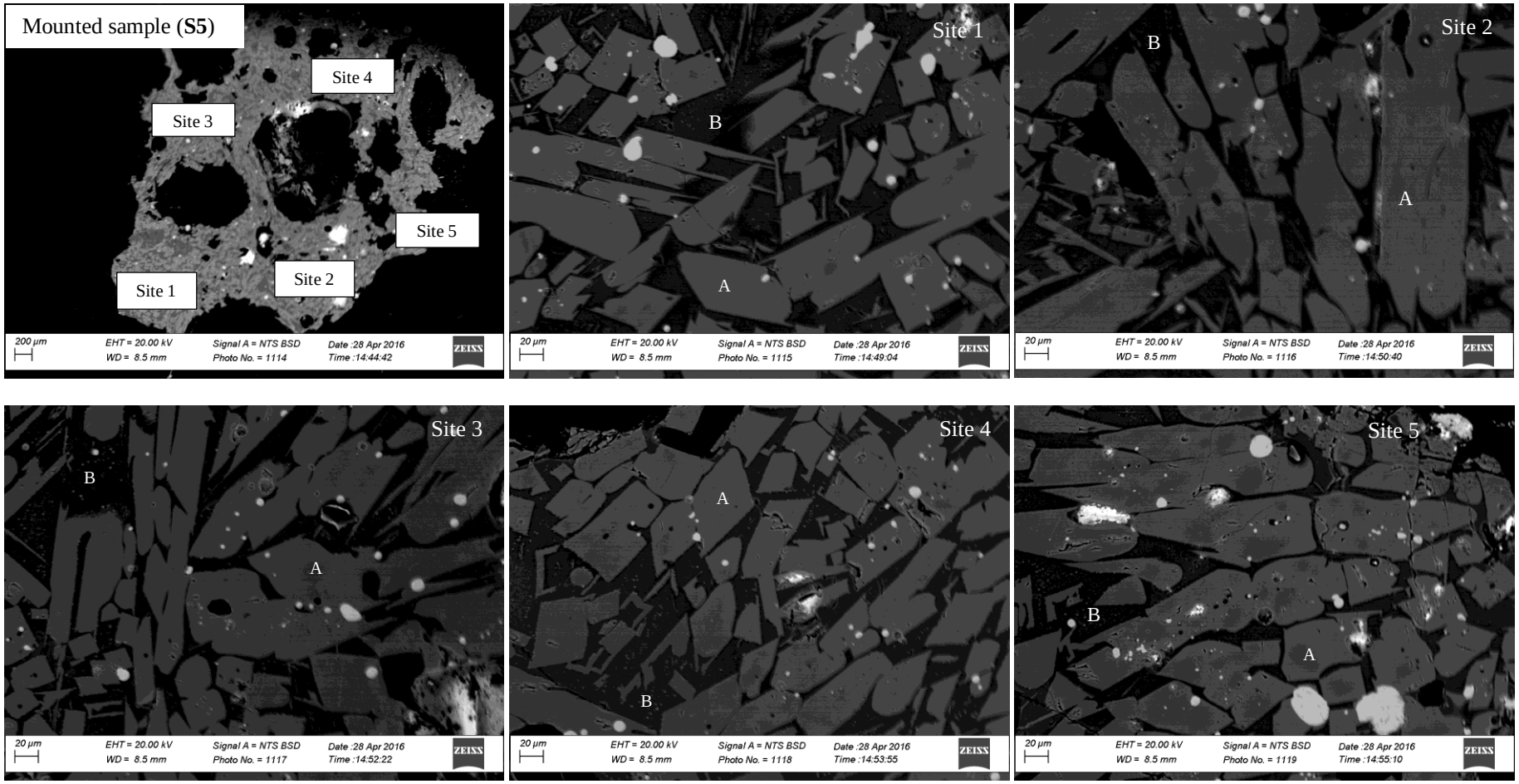

Phase	Na	Mg	Al	Si	P	K	Ca	Ti	Cr	Mn	Fe	Zn	O	C
Ti-rich (A)	0.00	0.40	0.48	0.00	0.00	0.09	0.06	57.75	0.00	1.14	0.35	0.00	39.74	-
Silicates (B)	1.45	1.06	3.17	26.29	0.00	7.81	0.77	6.20	0.00	9.48	0.76	0.00	43.01	-
Metal globules (white)	0.00	0.00	0.00	0.00	0.00	0.00	0.00	2.40	0.00	0.00	95.14	0.00	1.58	0.88

Figure 4.23: The SEM micrographs of the titania slag, **S5**, sample that was produced from the furnace dust at 1650˚C for 10 min. The Ore-C ratio was 9.7 and the composition is in weight percent.

of the interfacial tension of the Ti-rich phases on temperature even though it is known that an interfacial or surface tension of most materials, except silicates, increases with decreasing temperature (Keene, 1995).

A look into the composition of the coalesced Ti-rich phases within the **S4** and **S5** (cf. Table 4.6 and Table 4.7) samples shows that such phases were still consistent with the relatively high amount of trivalent titanium compared to the tetravalent titanium. The abundances of the Ti_2O_3 and TiO_2 within such phases were further comparable to those within the **S2** and **S3** samples and that led to relatively the same contents of the equivalent titanium dioxide in the Ti-rich phases of such four slag samples.

Table 4.6: The composition of the **S4** sample that was produced at 1650˚C for 8 min as determined by the SEM-EDS and XRF techniques. The composition is in weight percent.

Phase	Na_2O	MgO	Al_2O_3	SiO_2	P_2O_5	K_2O	CaO	Ti_2O_3	TiO_2	Cr_2O_3	MnO	FeO	$TiO_2{}^{eq}$
Ti-rich	0.00	1.08	0.84	1.02	0.00	0.41	0.00	63.77	23.53	0.00	2.04	0.24	94.39
FactSage	0.81	1.50	0.88	4.71	0.00	0.62	0.30	58.21	26.15	0.07	5.22	1.52	90.84
Silicates	1.47	2.19	7.60	58.38	0.00	10.22	0.82	6.90	2.54	0.00	8.68	0.44	10.20
FactSage	2.75	0.11	9.48	71.55	0.00	13.41	0.00	0.00	2.48	0.00	0.21	0.01	2.48
Bulk sample	0.84	1.47	4.03	14.32	0.04	3.16	0.33	50.42	18.61	0.10	5.26	1.42	74.64
FactSage	1.07	1.31	2.03	13.62	0.00	2.32	0.26	50.45	22.99	0.06	4.56	1.32	79.06

Nevertheless, the compositions of the Ti-rich phases within the **S4** and the **S2** samples were closely comparable and they were characterized by relatively higher abundances of MgO and MnO than the Ti-rich phases within the **S3** and **S5** samples. An incremental increase of FeO into the Ti-rich phases was further observed from the **S3** sample through to the **S5** sample. Such observation indicated an incremental approach to phase equilibria as has been reported that high titania slags solidify with the PSB phase which incorporates Fe, Mg, Mn and other minor cationic species that emanate from the impurity oxides (Pesl and Eric, 2002; Pistorius, 2002; Elstad et al., 2007).

The silicate phases were further rich in the impurity oxides, which claimed almost 90.1wt% and 89.4wt% within the **S4** and the **S5** samples respectively. However, it may be noted that an

Table 4.7: The composition of the **S5** sample that was produced at 1650˚C for 10 min as determined by the SEM-EDS and XRF techniques. The composition is in weight percent.

Phase	Na_2O	MgO	Al_2O_3	SiO_2	P_2O_5	K_2O	CaO	Ti_2O_3	TiO_2	Cr_2O_3	MnO	FeO	${TiO_2}^{eq}$
Ti-rich	0.00	0.67	0.90	0.00	0.00	0.11	0.09	65.09	24.02	0.00	1.47	0.45	96.35
FactSage	0.81	1.50	0.88	4.71	0.00	0.62	0.30	58.21	26.15	0.07	5.22	1.52	90.84
Silicates	1.95	1.76	5.99	56.25	0.00	9.41	1.07	6.99	2.57	0.00	12.24	0.97	10.35
FactSage	2.75	0.11	9.48	71.55	0.00	13.41	0.00	0.00	2.48	0.00	0.21	0.01	2.48
Bulk sample	0.63	1.34	2.95	13.71	0.02	2.54	0.31	51.29	18.94	0.11	5.13	3.03	75.94
FactSage	1.07	1.31	2.03	13.62	0.00	2.32	0.26	50.45	22.99	0.06	4.56	1.32	79.06

increase of the reduction time from 2 minutes to 10 minutes resulted in a gradual entrainment of total titanium into such silicate phases. The content of equivalent titanium dioxide in those silicate phases increased from 7.47wt% within the **S1** sample to 10.35wt% within the **S5** sample. A comparison with the slag samples that can contain a maximum of 5wt% impurity oxides showed that at most 5wt% of ${TiO_2}^{eq}$ can report into such silicate phases (Pesl and Eric, 2002). This degree of entrainment of the equivalent titanium dioxide into the silicate phases may indirectly highlight the degree of loss of such titanium during the production of the UGS according to the processes such as the one that is illustrated in Figure 2.3.

The equivalent titanium dioxide content within the bulk **S4** and **S5** samples were 74.64wt% and 75.94wt% respectively and these contents of equivalent titanium dioxide remained comparable with those that were observed within the **S2** and **S3** samples. However, the equivalent titanium dioxide content within the **S4** sample was more comparable with that within the **S3** sample while the equivalent titanium dioxide content within the **S5** and **S2** samples were closely comparable and slightly higher than those within the **S3** and **S4** samples. Both the **S4** and the **S5** samples had the significantly lower abundances of silica than the **S1**, **S2** and **S3** samples. Such silica abundance was closely comparable to the FactSage-calculated value at a reduction time of 10 minutes and this highlighted the potential of removing silica from the slag phase at such relatively higher reduction times.

The reaction kinetics data that is pertinent to production of titania slags is currently limited (Pistorius, 2002; Zietsman and Pistorius, 2004). Furthermore, very little has been done on the

ilmenite smelters furnace dust. For these reasons, it was challenging to compare and contrast the observations from the effects of reduction time on the slag composition with documented literature. However, the observed effects of the reduction time on the characteristics of the slag samples that were produced from the furnace dust are summarized in the next two subsequent paragraphs.

The reduction of the oxide of iron from the slag to the metallic phase was a very fast process that occurred mainly within the first two minutes of reaction. Beyond the reduction time of two minutes, the rate of the reaction decreased until the reaction was assumed to be complete after six minutes (cf. Figure A.5). An increase of the abundance of the equivalent titanium dioxide within the slag samples further increased with the reduction of the iron oxides from the slag phase until such equivalent titanium dioxide content remained around 75wt% (cf. Figure 4.24). Such significant reduction of iron oxide from the slag phase further resulted in a significant amount of trivalent titanium, which seemed to be in line with the inverse relationship of FeO and Ti_2O_3 that was reported previously (Pistorius, 2002).

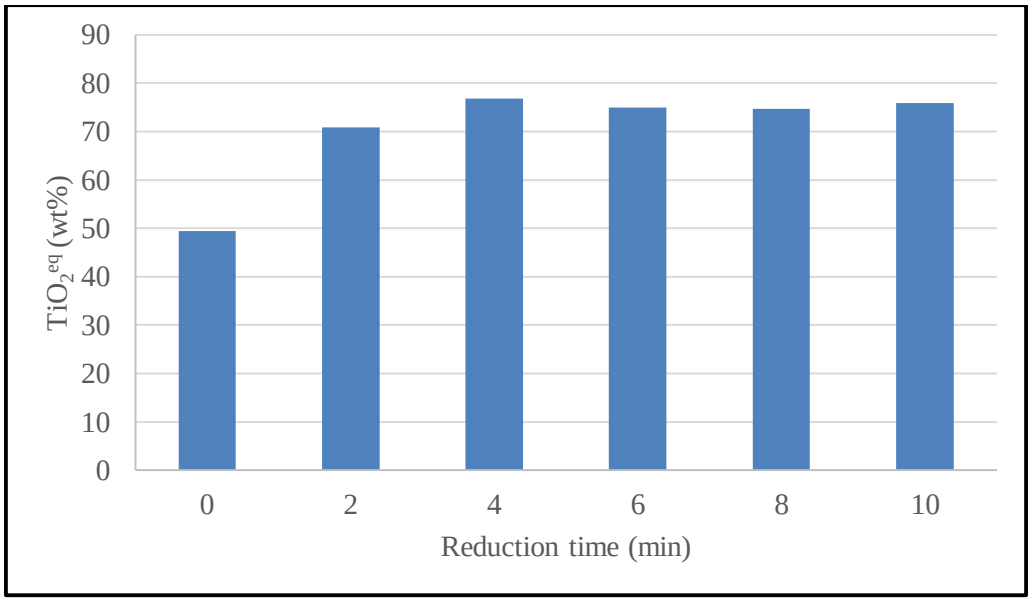

Figure 4.24: The dependence of the equivalent titanium dioxide content within the slag samples on reduction time at 1650˚C.

The mineral textures within the slag samples showed a gradual transformation from the textures

that were observed within the furnace dust with increasing reduction time until an exsolution among the different phases was significantly achieved. Such gradual transformation of the mineral textures with increasing reduction time was further associated with gradual increase of the size of metallic iron globules that formed in-situ within the slag samples. The maximum size of such metallic iron globules reached 40 µm, which fell within the 15-150 µm range that was reported by Bessinger (2000). It was also observed that an increase of the reduction time to beyond 6 minutes corresponded to a significant loss of silica from the slag phase.

An influence of temperature on the composition and mineral textures of the slag samples was investigated at a reduction time of 10 minutes and at 1600˚C and 1500˚C. The textures of mineral phases within the slag samples that were produced at such 1600˚C and 1500˚C did not show a significant deviation from the samples that were produced at 1650˚C for 10 minutes (cf. Figure 4.23, Figure 4.25 and Figure 4.26).

The bulk composition of the **S6** ample further showed the comparable results with the **S5** sample, but the **S6** sample exhibited a slightly lower equivalent titanium dioxide content of 72.65wt% and a relatively lower content of FeO than the **S5** sample. This slightly lower content of the equivalent titanium dioxide within the **S6** sample corresponded to the significantly higher abundance of silica within such sample (cf. Table 4.8). The relatively higher abundance of silica and the relatively lower abundance of FeO at 1600˚C than at 1650˚C were further consistent with the observations from Figure 4.8 and Figure 4.11.

Table 4.8: The composition of the **S6** sample that was produced at 1600˚C for 10 min as determined by the SEM-EDS technique. The composition is in weight percent.

Phase	Na_2O	MgO	Al_2O_3	SiO_2	P_2O_5	K_2O	CaO	Ti_2O_3	TiO_2	Cr_2O_3	MnO	FeO	$TiO_2{}^{eq}$
Ti-rich	0.00	0.58	0.83	0.00	0.00	0.04	0.00	66.00	24.36	0.00	0.77	0.10	97.71
FactSage	0.74	1.53	0.65	4.18	0.00	0.45	0.31	57.82	28.43	0.04	5.03	0.83	92.68
Silicates	1.48	2.19	7.10	61.40	0.00	8.39	0.97	5.40	1.99	0.04	10.31	0.16	7.99
FactSage	3.17	0.11	9.97	70.77	0.00	13.43	0.01	0.00	2.29	0.00	0.25	0.01	2.29
Bulk sample	0.61	1.28	2.70	18.49	0.00	2.18	0.21	49.07	18.12	0.06	5.25	2.03	72.65
FactSage	1.10	1.32	2.03	14.07	0.00	2.38	0.27	49.23	24.54	0.04	4.32	0.71	79.25

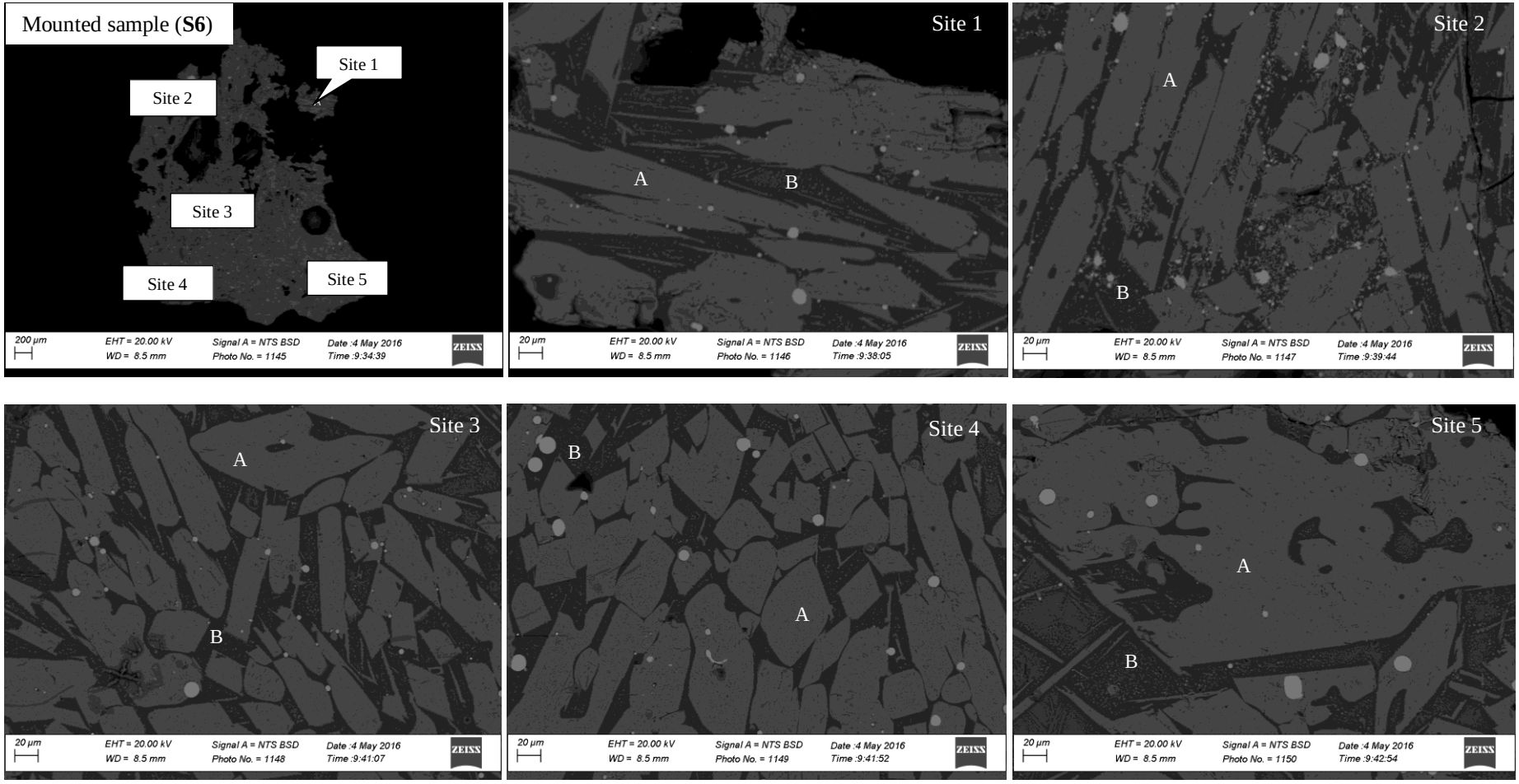

Phase	Na	Mg	Al	Si	P	K	Ca	Ti	Cr	Mn	Fe	Zn	O	C
Ti-rich (A)	0.00	0.35	0.44	0.00	0.00	0.04	0.00	58.56	0.00	0.59	0.08	0.00	39.94	-
Silicates (B)	1.10	1.32	3.76	28.70	0.00	6.96	0.69	4.79	0.03	7.98	0.12	0.00	44.56	-
Metal globules (white)	0.00	0.00	0.00	1.77	0.00	0.00	0.00	1.97	0.61	1.82	92.86	0.00	0.51	0.46

Figure 4.25: The SEM micrographs of titania slag, **S6**, sample that was produced from the furnace dust at 1600˚C for 10 min. The Ore-C ratio was 9.7 and the composition is in weight percent.

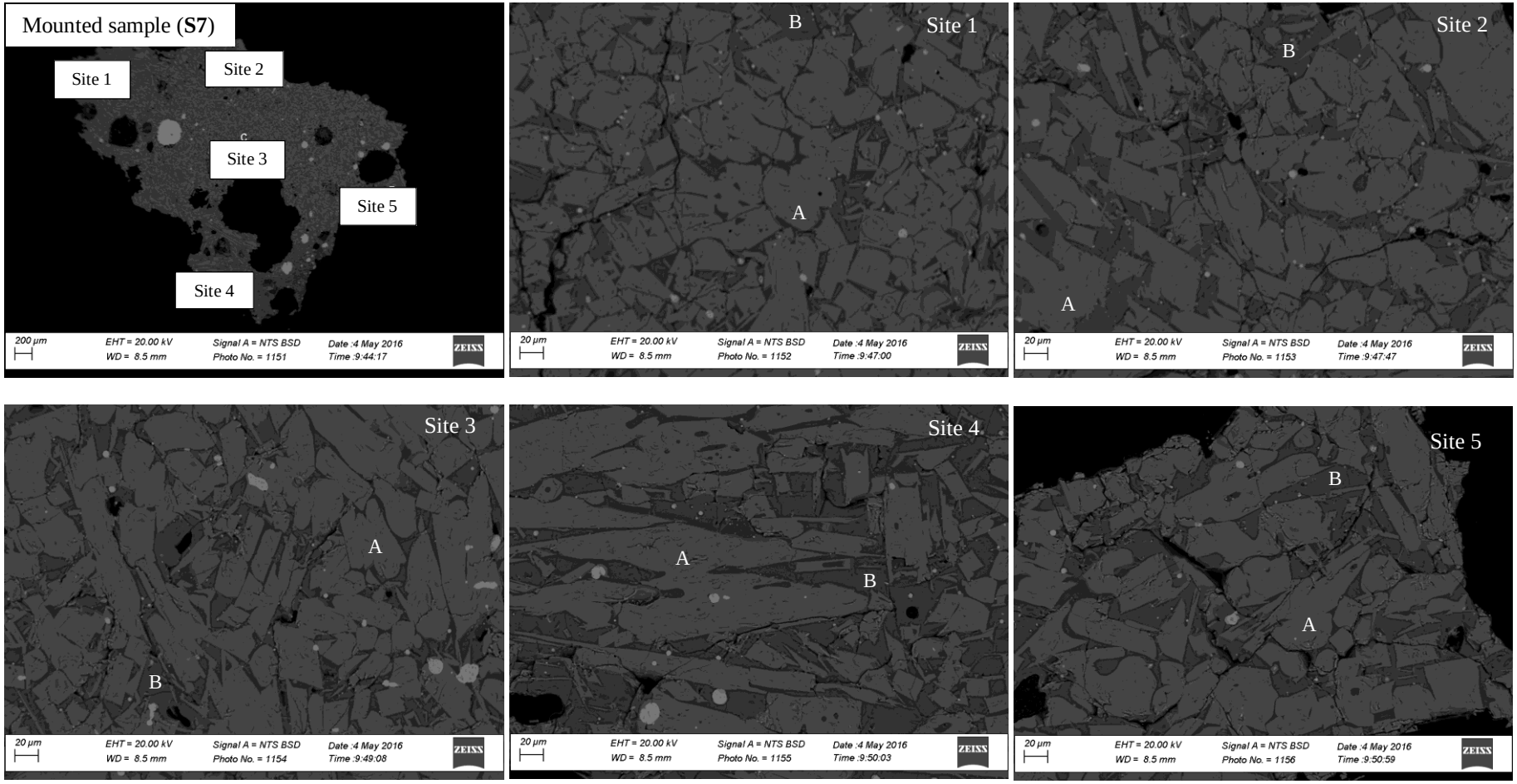

Phase	Na	Mg	Al	Si	P	K	Ca	Ti	Cr	Mn	Fe	Zn	O	C
Ti-rich (A)	0.00	0.65	0.51	0.05	0.00	0.00	0.00	51.80	0.21	1.36	7.30	0.00	38.13	-
Silicates (B)	1.16	0.33	2.95	26.73	0.00	6.16	0.92	6.77	0.00	6.60	5.14	0.00	43.24	-
Metal globules (white)	0.00	0.00	0.00	0.00	0.10	0.00	0.00	2.17	0.00	0.03	96.84	0.00	0.53	0.33

Figure 4.26: The SEM micrographs of titania slag, **S7**, sample that was produced from the furnace dust at 1500˚C for 10 min. The Ore-C ratio was 9.7 and the composition is in weight percent.

In the case of the bulk composition of the **S7** sample, the equivalent titanium dioxide content was only 65.87wt% (cf. Table 4.9). Such lower content of the equivalent titanium dioxide at 1500˚C was mainly because of the observed significant amount of both iron oxide and impurity oxides within such **S7** sample. It was observed that the slag phase was partially molten at 1500˚C and FactSage® 6.4 calculated that almost 63% of such slag was in the solid form. For this reason, a significant production of a molten metallic phase that could easily separate from the slag phase was not feasible. Even though it could be lessened by the mass transfer constraints of carbon to FeO sites and continuous stripping and loss of CO by a purge gas, a solid-state thermal reduction of FeO to Fe within the solid region of such partially molten slag was strongly believed to occur. However, an accurate quantification of such solid-state reduced iron product by the XRD technique was not possible because much of the slag samples were amorphous as will be seen in Table 4.10.

Table 4.9: The composition of the **S7** sample that was produced at 1500˚C for 10 min as determined by the SEM-EDS technique. The composition is in weight percent.

Phase	Na_2O	MgO	Al_2O_3	SiO_2	P_2O_5	K_2O	CaO	Ti_2O_3	TiO_2	Cr_2O_3	MnO	FeO	$TiO_2{}^{eq}$
Ti-rich	0.00	1.08	0.97	0.11	0.00	0.11	0.00	58.38	21.54	0.31	1.75	9.39	86.42
FactSage	0.50	1.57	0.30	3.60	0.00	0.18	0.32	56.09	32.83	0.01	4.37	0.23	95.16
Silicates	1.57	0.55	5.57	57.18	0.00	7.42	1.28	7.64	2.81	0.00	8.53	6.61	11.30
FactSage	4.12	0.12	10.21	70.21	0.00	13.23	0.01	0.00	1.78	0.00	0.31	0.00	1.78
Bulk sample	0.72	1.02	2.49	16.92	0.00	1.89	0.17	44.49	16.43	0.19	4.49	11.21	65.87
FactSage	1.13	1.32	2.03	15.22	0.00	2.46	0.27	46.30	27.41	0.01	3.66	0.19	78.87

From all these observations, it may be noted that there existed discrepancies between FactSage® 6.4 calculations and experimental observations in terms of the compositions of the Ti-rich and silicate phases. The continuous purging of argon during the experimental reduction tests, which was not employed during the simulation work, might have facilitated a loss of some impurity components (Mn and SiO) into the off-gas stream, as was mentioned earlier, thereby lowering the abundance of those species in the Ti-rich phases. Another important possibility for these discrepancies can be due to a total reduction time of samples. FactSage® 6.4 calculations assumed that equilibria (reaction and phase) were attained. However, from the experimental

point of view, a total reduction time of samples in the furnace might have not provided enough time for a complete mass transfer of all individual chemical species between the silicate and Ti-rich phases. This can be the case, as such phase equilibria has been reported to occur after approximately six hours of reduction (Pesl and Eric, 1999; Pesl and Eric, 2002).

The maximum achievable reduction of the oxides of iron from the slag phase was found to be more feasible at 1600˚C and 1650˚C and this was in agreement with the 1600-1700˚C temperature range that is used for the production of titania slags (Pesl, 1997; Zietsman, 2004). The equivalent titanium dioxide content of the slag samples at such 1600˚C and 1650˚C compared with the 75wt% that was observed by Rughubir and Bessinger (2007).

Furthermore, the consistently high levels of trivalent titanium rendered such slag samples unacceptable to serve as a direct feedstock into the chloride process (cf. Table 1.2). Not only did such high levels of trivalent titanium disqualify the slag samples to serve as direct feedstock to the chloride processes, but also the significant amount of the impurity oxides within such slag samples contributed towards such disqualification.

In order to compare the compositional location of the titania slag samples that were produced from the furnace dust with the compositional location of other industrial titania slags within the $FeO - TiO_2 - Ti_2O_3$ ternary system, the normalized abundances of FeO, TiO_2 and Ti_2O_3 were plotted as is shown in Figure 4.27. The impurity oxides were held constant during an assignment of such location.

The location of the composition of such slag samples within the FeO-TiO_2-Ti_2O_3 ternary system showed a significant deviation from the location of most industrial slags that are produced from ilmenite ores with less impurities (cf. Figure 2.1). The industrial slags often contain around 10wt% of iron oxide and relatively higher content of Ti^{4+} (TiO_2) than of Ti^{3+}(Ti_2O_3). However, in the case of this furnace dust, a significant extent of reduction was required in order to achieve the relatively higher content of the equivalent titanium dioxide because of the larger fraction of the impurity oxides.

A comparison of Figure 2.1, Figure 2.2 and Figure 4.27 shows that the relatively higher content of the trivalent titanium within the slag samples that were produced from the furnace dust was

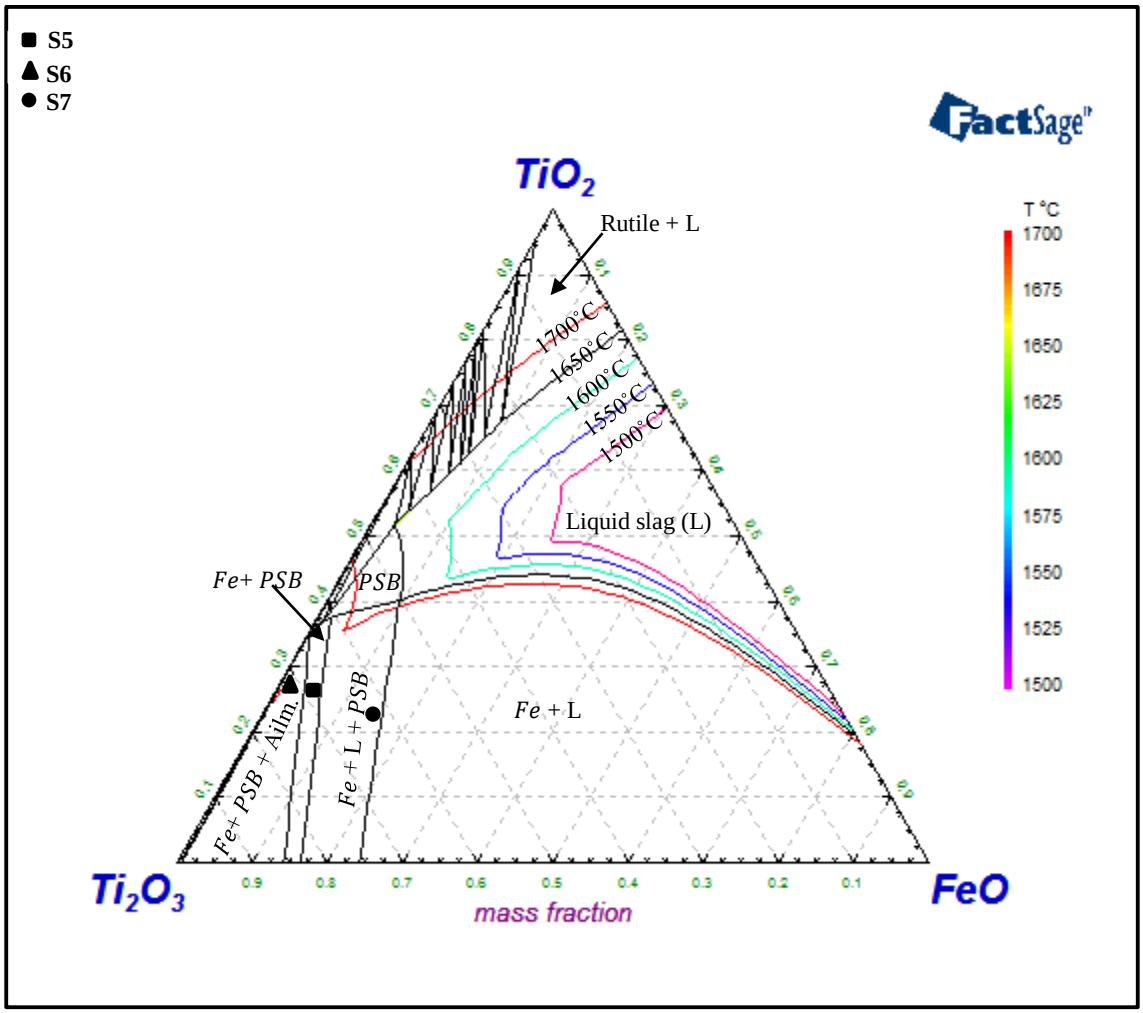

Figure 4.27: A polythermal liquidus projection within the FeO-TiO_2-Ti_2O_3 ternary system showing the location of the solidified slag samples that were produced from the furnace dust. The univariant curves were developed at 1650˚C and such univariant curves can shift accordingly depending on the temperature of interest. Ailm refers to AIlmenite and it is a solid solution of $FeTiO_3$-Ti_2O_3-$MgTiO_3$-$MnTiO_3$ (FactSage® 6.4).

slightly more than it would be required by the M_3O_5 stoichiometry. This seemed to be an opposite of the industrial slags, which have slightly more tetravalent titanium and less trivalent titanium than it is required by the M_3O_5 stoichiometry (Pistorius, 2002; Pistorius and Coetzee, 2003; Pistorius, 2003; Pistorius, 2004).

The significant reduction of iron oxide from the current slag samples and a hence higher content

of the trivalent titanium within such slag samples resulted in the slag samples solidifying with the PSB phase, elemental iron and some solid solutions that have a structure resembling that of ilmenite as can be seen in Figure 4.27. Such mineral phases were further confirmed with the use of the XRD technique and the abundances of such mineral phases are summarized in Table 4.10.

The slag samples were found to be rich in the amorphous content just as the furnace dust was. The significant abundance of such amorphous content within the slag samples was influenced by the significant abundance of silicate phases that were not removed from the slag during the experimental reduction tests. Furthermore, the dependence of such amorphous content on the reduction time showed periodic fluctuations between 55wt% and 70wt%. Such content of the amorphous phase approached 70wt% as the reduction time increased and this 70wt% amorphousness was comparable with the 71wt% that was determined earlier within the furnace dust sample.

Table 4.10: The abundance of mineral phases within the slag samples as determined by the XRD technique. The abundance is in weight percent.

Mineral phase	1650˚C					1600˚C	1500˚C
	2 min (**S1**)	4 min (**S2**)	6 min (**S3**)	8 min (**S4**)	10 min (**S5**)	10 min (**S6**)	10 min (**S7**)
PSB (M_3O_5)	17.93	11.66	15.26	15.60	19.77	19.70	51.19
Ilmenite	7.83	5.69	5.51	5.54	6.03	4.89	3.53
Rutile	4.49	5.48	2.63	2.41	1.39	1.79	1.06
Anatase	0.21	0.11	0.13	0.09	0.10	0.16	0.09
Iron	0.15	0.20	0.29	0.45	0.43	0.69	1.86
Wustite (FeO)	0.63	3.94	2.12	2.20	1.00	1.88	0.38
Magnetite-Ulvospinel (M_3O_4)	0.28	0.43	0.00	0.44	0.21	0.54	0.38
Corundum (M_2O_3)	10.70	3.00	10.03	3.17	4.63	3.35	3.45
Amorphous	57.78	69.49	64.02	70.11	66.44	67.00	38.07
Total	100.00	100.00	99.99	100.01	100.00	100.00	100.01

This amorphous content seemed to be significantly lower for samples that were produced at 1500˚C than for samples that were produced at 1600˚C and 1650˚C. Such lower amorphous

content at 1500˚C further corresponded to a significant increase of the content of other crystalline phases including the PSB phase. At such 1500˚C, the molten region that co-existed with the solid region within the partially molten slag was undercooled. Crystallization and hence less formation of amorphous solids was therefore more dominant at 1500˚C than at 1600˚C and 1650˚C.

Among the identified crystalline phases, the PSB phase was the major phase and it explained more than almost 40wt% of such crystalline phases. The dependence of the content of such PSB phase on the reduction time at 1650˚C showed a decrease from 2 minutes to 4 minutes and a gradual increase from the reduction time of 6 minutes until such phase could explain almost 82wt% of the crystalline phases. The decrease of the content of the PSB phase at a reduction time of 4 minutes coincided with an increase of the rutile and wustite phases. The thermodynamic drive for the formation of such rutile and wustite phases at the reduction time of 4 minutes was not well understood. However, the gradual increase of the content of PSB phase from 6 minutes to 10 minutes as determined by the XRD technique coincided with a gradual increase of the abundance of iron oxide in the Ti-rich phases as determined by the SEM-EDS technique. Bickley et al. (1997) showed that the abundance of such PSB phase generally increases with an increase in the nominal abundance of iron oxide. Such increase of the PSB phase was also in line with the decrease of the other titanium bearing phases such as rutile.

Of further importance to note from Table 4.10 is the presence of ilmenite that seemed consistent with the stable phases that were observed in Figure 4.27. Even though the XRD technique generally identified such phases as ilmenite, it was clear from Figure 4.27 that a solid-solution of the oxides of iron, titanium, magnesium and manganese were responsible for such synthetic phases which resembled ilmenite in structure. Such ilmenite phase, as determined by the XRD technique, showed a slight decrease from the reduction time of 2 minutes to the reduction time of 4 minutes and it remained relatively constant beyond such reduction time of 4 minutes. The decrease of the ilmenite phases at the reduction time of 4 minutes seemed to be in line with the previously observed formation of rutile and wustite at such reduction time. An insignificant change of the abundance of such ilmenite phases beyond the reduction time of 4 minutes highlighted that the decrease of the abundances of rutile and wustite phases were in favour of the

formation of the PSB phase.

The other mineral phases such as corundum and ulvospinel showed a periodic infinitesimal fluctuation with increasing reduction time, which could be induced by the periodic transfer of the oxide components between the Ti-rich and silicate phases as was seen previously.

(b) Metallic phase

The SEM micrographs of the metallic iron samples that were produced from the furnace dust along with the titania slag samples are shown in Figure 4.28. The compositions of such metallic iron samples are further presented in Table 4.11 to Table 4.13.

It was observed that the metallic iron samples consisted of invariably two phases namely the major iron-rich phases and the possible oxycarbide phases. Such possible oxycarbide phases were dominant in titanium, chromium, manganese, iron and some silicon and they existed as minor inclusions within the major iron-rich phases. An experimental identification of these possible oxycarbide phases complemented the calculations from FactSage® 6.4, which identified titanium within the metallic phase as only elemental titanium. Furthermore, the significant abundance of titanium in those possible oxycarbide phases and the small abundance of elemental

Table 4.11: The composition of metallic iron samples that were produced at 1650˚C and at the Ore-C ratio of 9.7 as determined by the SEM-EDS technique. The composition is in weight percent.

Sample tag	Time (min)	Phase	Al	Si	P	Ti	Cr	Mn	Fe	C	O
M1	2	Iron-rich	0.00	1.08	0.00	0.00	0.42	0.45	97.07	0.23	0.75
		Possible oxycarbides	0.00	0.11	0.00	59.57	3.17	17.58	19.07	0.52	0.00
M2	4	Iron-rich	0.00	2.29	0.00	0.00	0.23	1.24	95.61	0.21	0.41
		Possible oxycarbides	0.00	0.81	0.00	4.03	0.95	47.65	45.69	0.32	0.56
M3	6	Iron-rich	0.00	2.27	0.00	0.15	0.06	0.66	95.83	0.29	0.75
		Possible oxycarbides	0.00	0.27	0.00	55.12	1.44	24.84	16.66	0.74	0.93
M4	8	Iron-rich	0.01	0.47	0.04	0.20	0.16	0.35	97.13	0.59	1.04
		Possible oxycarbides	0.05	0.03	0.00	1.09	0.89	59.64	37.86	0.31	0.13
M5	10	Iron-rich	0.00	1.33	1.68	0.02	0.08	0.33	93.96	0.89	1.62
		Possible oxycarbides	0.00	0.67	0.00	31.90	2.56	2.85	58.43	2.51	1.09
FactSage® 6.4		Metallic iron	0.00	4.06	0.38	0.15	0.23	1.54	93.09	0.55	0.00

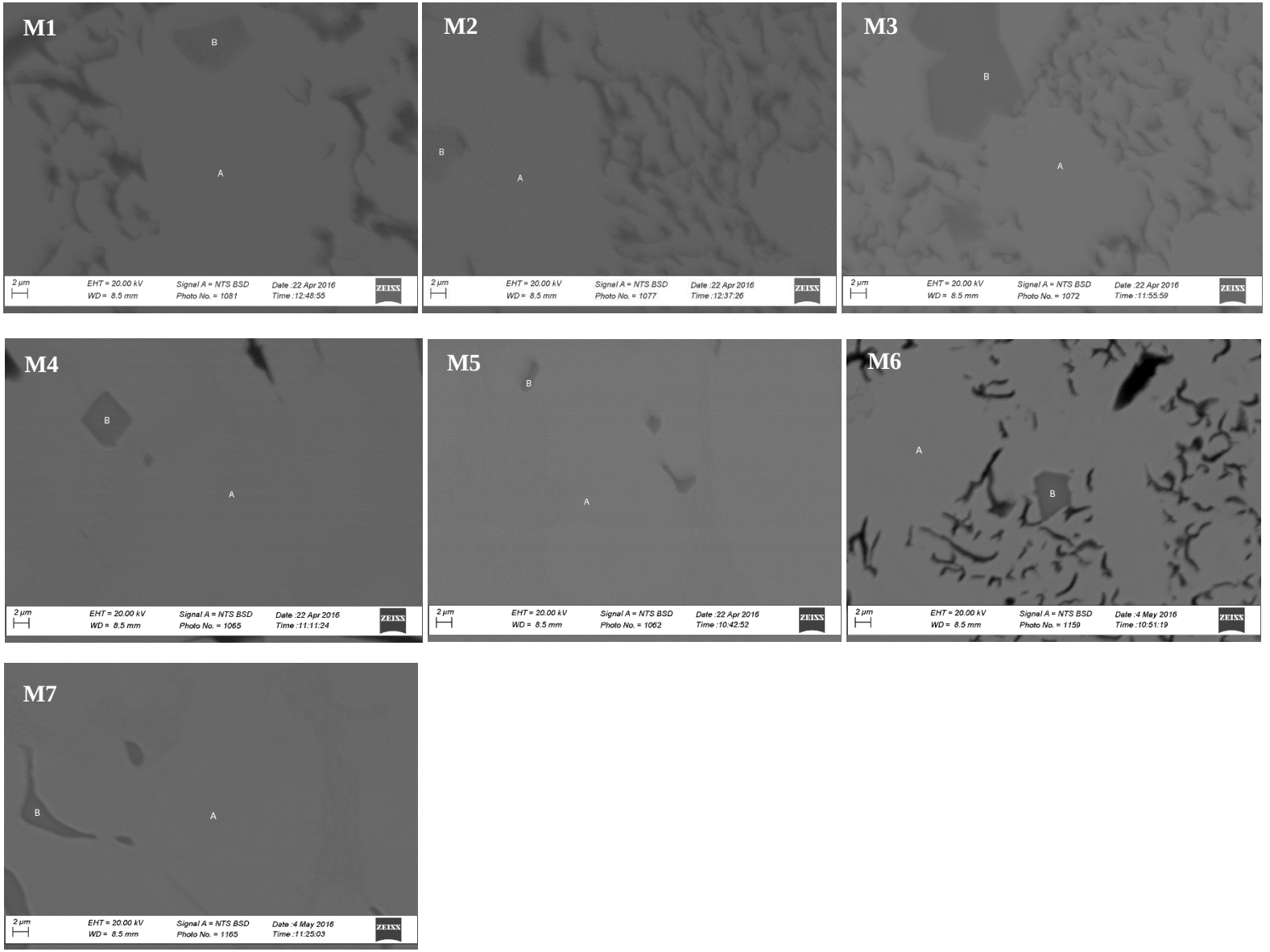

Figure 4.28: The SEM micrographs of metallic iron samples. A = iron rich and B = possible oxycarbides. Magnification was 7000X.

titanium in the iron- rich phases were consistent with the suggestions that titanium mainly reports into the metallic phase as carbide or oxycarbide phases (Galgali et al., 1998; Pesl and Eric, 2002).

The iron-rich phases within the metallic iron samples that were produced within the first 8 minutes of reduction exhibited the Fe content that was above 95wt% (cf. **M1** to **M4**). Such content of Fe fell within the acceptable marketable value of greater than 95wt% (Gomes et al., 1974). However, the iron-rich phases within the metallic iron sample that was produced at the reduction time of 10 minutes (cf. **M5**) exhibited the Fe content of 93.96wt% and such Fe content approached the FactSage-calculated value of 93.09wt%. The decrease of the Fe content within the **M5** sample was due to a significant deportment of phosphorus together with silicon into the metallic phase. It was observed that such phosphorus started to report into the metallic phase only after the reduction time of 8 minutes while silicon had been periodically partitioned between the slag and the metallic phase. However, the decrease of the abundance of silicon from the iron-rich and the possible oxycarbide phases in conjunction with the decrease of the silica abundance from the slag phase at a reduction time of 8 minutes indicated a possible loss of Si, possibly as SiO, into the off-gas stream as has been mentioned previously.

The abundance of titanium was significantly low in such iron-rich phases except at the reduction times of 6 minutes and 8 minutes, when such abundance was comparable with the FactSage-calculated abundance. However, a further decrease of the titanium abundance was observed at the reduction time of 10 minutes. On the other hand, the abundance of Cr showed a gradual decrease from the iron-rich phases with an increase in the reduction time from 2 minutes to 6 minutes and slight fluctuations of such Cr abundance were noticeable beyond 6 minutes of reduction. To further note from Table 4.11, the abundance of Mn in the iron-rich phases showed a gradual increase from 2 minutes to the reduction time of 4 minutes, but a decrease of such Mn abundance from the iron-rich phases at a reduction time of 6 minutes to 10 minutes was observed.

From these observations, it was inferred that Ti, Cr and Mn were mainly partitioned between the slag phase and the possible oxycarbide phases. Within such possible oxycarbide phases, the abundances of Ti and Cr were observed to increase and decrease simultaneously while those of

Mn and Fe further showed a similar increase and decrease with an increase in reduction time. It was only at the reduction time of 10 minutes when the abundance of Mn was significantly low while the abundance of Fe remained high together with the abundances of Ti and Cr in such oxycarbide phases.

Such periodic increase and decrease of the Cr abundance correlated well with the fluctuating abundance of Cr_2O_3 within the slag phase. Furthermore, the increase of the abundance of Mn into the metallic phase, together with the possible loss of such Mn into the off-gas stream, corresponded to a gradual decrease of the abundance of MnO from the slag phase from the reduction time of 2 minutes to 6 minutes. The loss of Mn into the off-gas stream was inferred at a reduction time of 6 minutes where it was observed that the decrease of the Mn abundance from both the iron-rich and the possible oxycarbides corresponded to the decrease of the MnO abundance from the slag phase.

The iron-rich phases of the metallic iron sample that was produced at 1600˚C for 10 minutes (cf. **M6** and Table 4.12) exhibited the Fe content of 93.03wt% and this Fe content was comparable to the 92.65wt% that was calculated by FactSage® 6.4. Both the FactSage® 6.4 calculations and the experimental reduction tests were in agreement with the slightly lower content of Fe within the iron-rich phase that was produced at 1600˚C than the iron-rich phase that was produced at 1650˚C for 10 minutes.

Table 4.12: The composition of a metallic iron sample that was produced at 1600˚C and at the Ore-C ratio of 9.7 as determined by the SEM-EDS technique. The composition is in weight percent.

Sample tag	Time (min)	Phase	Al	Si	P	Ti	Cr	Mn	Fe	C	O
M6	10	Iron-rich	0.03	3.91	0.00	0.00	0.22	1.97	93.03	0.33	0.53
		Possible oxycarbides	0.00	0.17	0.00	46.34	4.49	38.23	9.05	1.57	0.14
FactSage® 6.4		Metallic iron	0.00	3.57	0.37	0.20	0.27	2.08	92.65	0.84	0.00

A look into Table 4.11 and Table 4.12 shows that such decrease was due to relatively higher abundances of Cr and Mn into the metallic phase at 1600˚C than at 1650˚C. The experimental composition of the iron-rich phases showed a further higher abundance of silicon at 1600˚C than

at 1650˚C even though it was observed from FactSage® 6.4 calculations that silicon was relatively lower within the metallic phase at lower temperatures (cf. Figure 4.9). The relatively high abundance of Si within the iron-rich phases that were produced at 1600˚C than those that were produced at 1650˚C was possibly due to a significant transfer of any silicon that would be present within the possible oxycarbide phases into the iron-rich phases.

The composition of a metallic iron sample that was produced at 1500˚C for 10minutes showed a significant difference from the composition of the samples that were produced at 1600˚C and 1650˚C (cf. **M7** and Table 4.13). Both the iron-rich and the possible oxycarbide phases within the **M7** sample were significantly richer in Fe and less associated with other elemental components than the samples that were produced at 1600˚C and at 1650˚C. Such richness in Fe was further found to be more than it was calculated by FactSage® 6.4.

Table 4.13: The composition of a metallic iron sample that was produced at 1500˚C and at the Ore-C ratio of 9.7 as determined by the SEM-EDS technique. The composition is in weight percent.

Sample tag	Time (min)	Phase	Al	Si	P	Ti	Cr	Mn	Fe	C	O
M7	10	Iron-rich	0.00	0.03	0.27	0.00	0.00	0.00	98.47	0.47	0.76
		Possible oxycarbides	0.00	0.00	0.63	0.00	0.54	1.24	97.23	0.29	0.07
FactSage® 6.4		Metallic iron	0.00	2.06	0.36	0.67	0.32	3.47	91.15	1.97	0.00

At a temperature of 1500˚C, it was observed that the slag phase was partially molten and a significant amount of such slag was in the solid state. Within the molten region of such partially molten slag, the preferential reduction of FeO to Fe was believed to be dominant. In addition, the preferential diffusion of elemental iron, which was produced from the solid-state thermal reduction within the solid region of the partially molten slag, into the molten region was considered to provide a possible explanation to the richness of such metallic iron sample in Fe.

The deportment of different elements into the metallic phase as was observed from both the experimental reduction tests and FactSage® 6.4 calculations are summarized in Table 4.14. The data in Table 4.14 is further depicted in Figure 4.29 and Figure 4.30.

Table 4.14: Percentage deportment of different elements into the iron-rich phases.

Elements	Experimental			FactSage		
	1500˚C	1600˚C	1650˚C	1500˚C	1600˚C	1650˚C
Fe	44.64	74.42	75.42	99.54	98.31	96.86
Al	0.00	0.74	0.00	0.00	0.00	0.00
C	0.43	0.53	1.44	4.33	1.80	1.16
Ca	0.00	0.00	0.00	0.00	0.00	0.00
Cr	0.00	47.48	17.32	94.48	78.38	63.85
Mn	0.00	12.66	2.13	30.39	17.71	12.85
Si	0.06	13.17	4.49	9.48	15.94	17.78
Ti	0.00	0.00	0.01	0.51	0.15	0.11
Mg	0.00	0.00	3.02	0.00	0.00	0.00

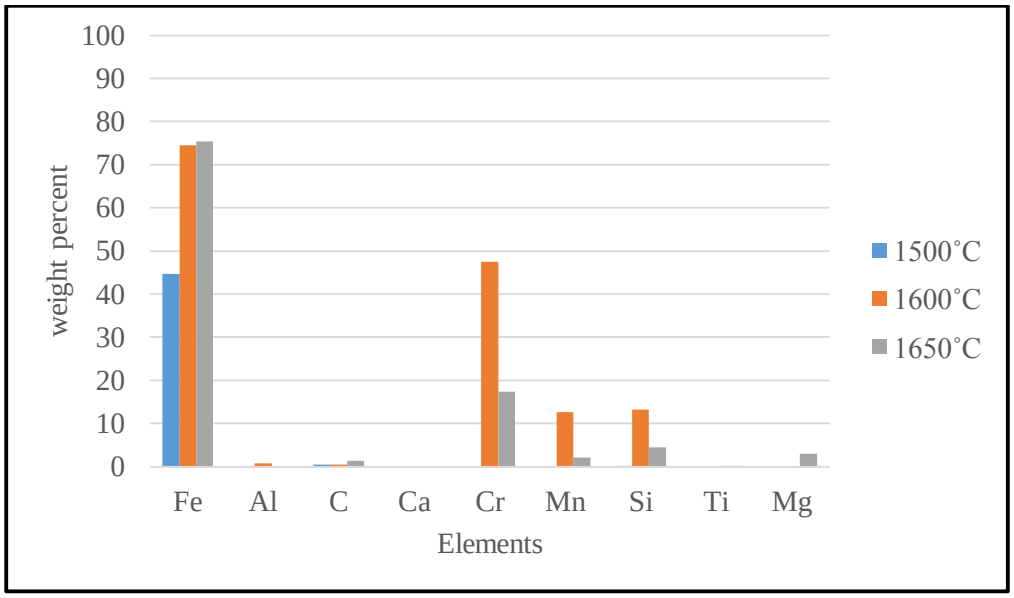

Figure 4.29: Deportment of elements into the iron-rich phases at a reduction time of 10 min as observed from experimental tests.

An insignificant deportment of Al, Ca, Mg and Ti are observed in Figure 4.29 and Figure 4.30. A further observation from experimental reduction tests was an insignificant deportment of most elements at 1500˚C and this was consistent with the lower $TiO_2{}^{eq}$ content that was observed within the **S7** sample.

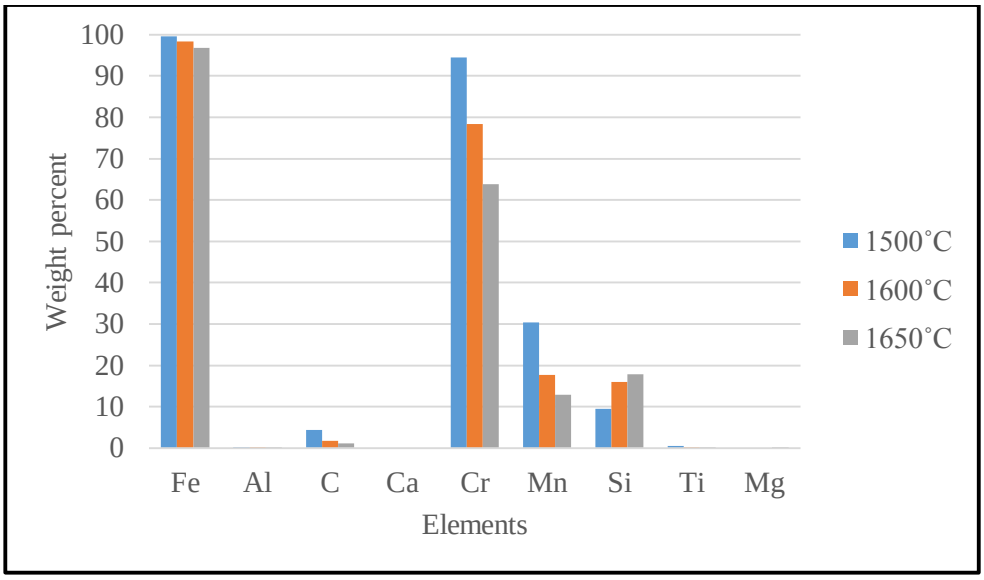

Figure 4.30: Deportment of elements into the metallic phase as observed from FactSage® 6.4 calculations.

It may also be noted that FactSage® 6.4 calculations showed relatively higher deportment of elements into the metallic phase than the experimental reduction tests. This difference was attributed to the previously mentioned gas stripping effect that was encountered during experimental work. As was observed during the discussion of titania slags, this gas stripping significantly removes CO, which could further contribute towards reduction process. Furthermore, a continuous loss of Mn and Si as SiO, which would otherwise report into the metallic phase, was enhanced under such gas stripping conditions.

This gas stripping effect, together with the temperature dependence of the Boudouard reaction, can further explain the higher carbon content in iron-rich phases within the **M6** and **M7** samples as calculated by FactSage® 6.4 than as was observed from experimental reduction tests. An increase of carbon content in the metallic phase with decreasing temperature as calculated by FactSage® 6.4 could possibly stem from the Boudouard reaction, which favours the production of C and CO_2 at those cooler temperatures. Within the closed system where there is no removal of CO (FactSage), a carbon content within the system would increase and hence higher carbon dissolution into the metal.

4.2.3. Possible integration of the furnace dust into the current industrial production of titania slag

An incorporation of the furnace dust into the currently employed processes for the production of a titania slag and a metallic iron can be twofold. Firstly, the furnace dust can be carbothermically reduced as a separate stream, as was done in this current study, to recover both a titania slag and a metallic iron. This process route can require mixing the furnace dust with the reductant after which the mixture is pelletized in order to avoid any loss of the furnace dust into the off-gas stream. It may be noted that the direct use of the furnace dust as a feedstock for the production of a titania slag resulted in a significant amount of impurity oxides within such slag phase, which was in agreement with the observations from Rughubir and Bessinger (2007). A development of a hydrometallurgical flowsheet that may be based on the proposal of Borowiec et al. (1998) and a modification of such process (Lasheen, 2008; Dong et al., 2012), can be considered in order to upgrade such titania slag. A typical flowsheet that summarizes this proposed route is illustrated in Figure 4.31(a).

Secondly, the furnace dust may be recycled and blended with fresh ilmenite feed after which such consolidated feed is charged into the electric arc furnaces as is shown in Figure 4.31(b). To avoid any loss of the fine furnace dust into the off-gas stream during the reductive smelting, the production of pellets, either from the furnace dust or the blended feed, can be considered. The production of such pellets from the blended feed can be more advantageous than when such pellets are produced solely from the furnace dust because the loss of fresh ilmenite fines can also be minimized.

The compositions of the slag and metallic phases that were obtained from the blended feed of the furnace dust and ilmenite are presented in Table 4.15 to Table 4.17. Such compositions were obtained from the FactSage® 6.4 calculations at 1650˚C and at varying ilmenite to furnace dust mass ratios.

It was observed that an increase of the ilmenite to furnace dust ratio from 3 to 5 corresponded to a decrease of the abundance of the impurity oxides from the slag phase. The carbothermic reduction of the feed streams that were blended at the ilmenite to furnace dust ratios of 4 and 5 resulted in the slag samples with the impurity oxides that were below the specified upper limits

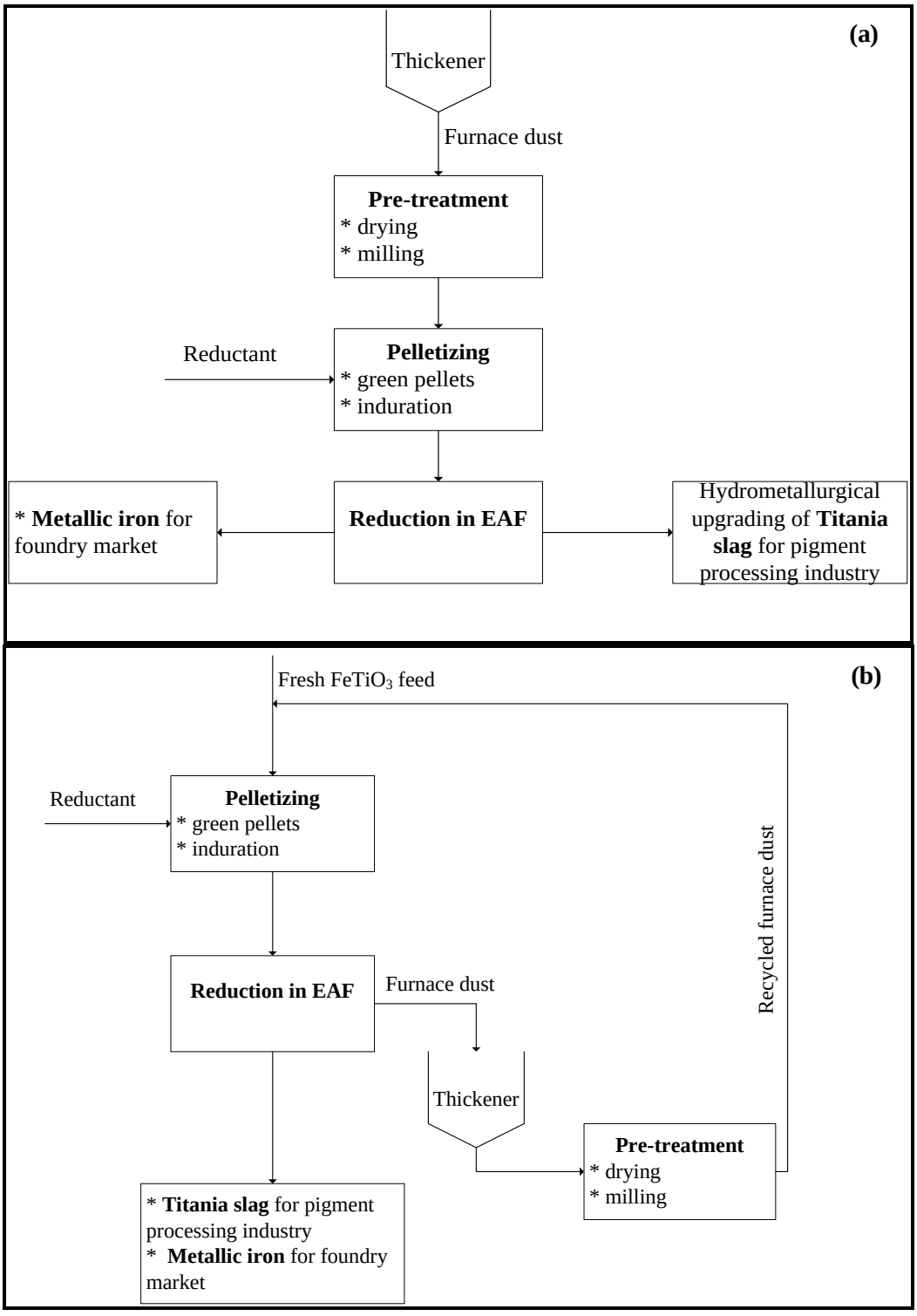

Figure 4.31: The proposed flowsheets for the production of a titania slag and a metallic iron from the furnace dust. A route for treating the furnace dust as a separate stream **(a)** and a route for recycling of the furnace dust **(b)**.

(cf. Table 1.2) throughout the possible Feed/C ratios of 12, 11, 10 and 9 that may be employed in an industry. However, the titania slag product that was produced from the feed that was blended at the ilmenite to furnace dust ratio of 3 showed that silica was still above the specified 4wt% for Feed/C ratios that were above 10. For this reason, the recycling and blending of 0.2 ton furnace dust with 0.8 ton fresh ilmenite feed and at the Feed/C ratio of approximately 11 may have a potential of producing a titania slag that can qualify as a feedstock to the downstream chloride process.

The recycling and blending of this furnace dust with fresh ilmenite feed further showed the potential of producing the metallic phase with, on average, 98.0wt% of Fe as opposed to the approximately 93.1wt% of Fe that was observed when the furnace dust was considered as the only feed at 1650˚C.

Table 4.15: The composition of the products at the ilmenite to furnace dust ratio of 3 as calculated by FactSage® 6.4 at 1650˚C.

Feed/C Ratio	Slag phase												Metallic phase							
	Na_2O	K_2O	Al_2O_3	SiO_2	CaO	FeO	MgO	MnO	Cr_2O_3	TiO_2	Ti_2O_3	${TiO_2}^{eq}$	Fe	C	Cr	Mn	O	P	Si	Ti
12.0	0.29	0.57	0.51	4.06	0.07	14.03	0.33	1.32	0.04	37.51	41.26	83.37	99.55	0.14	0.01	0.03	0.01	0.08	0.17	0.00
11.0	0.30	0.61	0.54	4.04	0.06	9.69	0.35	1.38	0.04	36.12	46.86	88.20	99.26	0.19	0.01	0.05	0.01	0.08	0.39	0.00
10.0	0.31	0.62	0.58	3.50	0.07	5.05	0.37	1.42	0.03	34.14	53.89	94.04	98.49	0.30	0.02	0.11	0.01	0.07	0.99	0.01
9.7	0.30	0.62	0.59	3.26	0.07	3.27	0.38	1.41	0.02	33.88	56.18	96.31	98.18	0.33	0.03	0.16	0.00	0.07	1.21	0.02

Table 4.16: The composition of the products at the ilmenite to furnace dust ratio of 4 as calculated by FactSage® 6.4 at 1650˚C.

Feed/C ratio	Slag phase												Metallic phase							
	Na_2O	K_2O	Al_2O_3	SiO_2	CaO	FeO	MgO	MnO	Cr_2O_3	TiO_2	Ti_2O_3	${TiO_2}^{eq}$	Fe	C	Cr	Mn	O	P	Si	Ti
12.0	0.23	0.46	0.41	3.27	0.05	14.45	0.26	1.06	0.03	38.41	41.36	84.37	99.62	0.13	0.01	0.03	0.01	0.06	0.14	0.00
11.0	0.24	0.47	0.44	3.19	0.06	10.22	0.28	1.11	0.03	36.82	47.14	89.20	99.33	0.19	0.01	0.04	0.01	0.06	0.36	0.00
10.0	0.25	0.49	0.46	2.68	0.06	5.34	0.30	1.15	0.03	34.93	54.31	95.29	98.66	0.28	0.02	0.08	0.01	0.05	0.89	0.01
9.7	0.24	0.48	0.48	2.48	0.06	3.40	0.31	1.15	0.02	34.67	56.72	97.70	98.41	0.31	0.02	0.12	0.00	0.05	1.06	0.01

Table 4.17: The composition of the products at the ilmenite to furnace dust ratio of 5 as calculated by FactSage® 6.4 at 1650˚C.

Feed/C ratio	Slag phase												Metallic phase							
	Na_2O	K_2O	Al_2O_3	SiO_2	CaO	FeO	MgO	MnO	Cr_2O_3	TiO_2	Ti_2O_3	${TiO_2}^{eq}$	Fe	C	Cr	Mn	O	P	Si	Ti
12.0	0.20	0.39	0.34	2.74	0.04	14.69	0.22	0.90	0.02	39.06	41.38	85.05	99.66	0.13	0.00	0.02	0.01	0.05	0.12	0.00
11.0	0.21	0.40	0.37	2.66	0.05	10.42	0.24	0.94	0.02	37.45	47.25	89.96	99.40	0.18	0.01	0.03	0.01	0.05	0.31	0.00
10.0	0.21	0.40	0.40	2.11	0.05	5.54	0.25	0.97	0.02	35.45	54.61	96.14	98.76	0.27	0.01	0.07	0.01	0.04	0.83	0.01
9.7	0.20	0.39	0.40	1.95	0.05	3.48	0.26	0.97	0.02	35.19	57.10	98.65	98.56	0.30	0.02	0.10	0.01	0.04	0.96	0.01

5. Conclusions and recommendations

5.1. Conclusions

The main aims of this study were to better understand the characteristics of the furnace dust and to investigate the potential of transforming such a metallurgical waste stream into a valuable stream through the production of a titania slag within the context of ilmenite smelting. The conclusions from specific objectives of the study are provided as follows:

(i) **Investigation of the chemical and mineralogical characteristics of the furnace dust**

The chemical and mineralogical characteristics of the furnace dust showed that such furnace dust was rich in the oxides of titanium and iron. The content of total titanium, expressed as TiO_2, within such furnace dust totalled to 49.39wt% and this titanium dioxide content was comparable with the titanium dioxide content of natural ilmenite ores. The content of total iron, expressed as Fe_2O_3, was found to be 29.51wt% and this was found to be relatively lower than the content of iron in natural ilmenite ores from different deposits within the Republic of South Africa. However, such valuable components were found to be associated with significant amounts of the impurity oxides, with silica contributing the largest fraction.

The qualitative and quantitative analyses of the mineral phases showed that the furnace dust contained 71.0wt% amorphous phases, 20.5wt% ilmenite, 7.0wt% rutile, 1.0wt% quartz and 0.5wt% iron. The mineral assemblage within such furnace dust further revealed that the valuable oxides were intimately intergrown with the impurity oxides and this rendered such furnace dust a very complex material. Furthermore, the furnace dust was found to be mainly fine with 80% of particles having a size less than 100 µm. A combination of the mineral assemblage and the fineness of this furnace dust shed some light on the challenges that can be associated with enriching such furnace dust with the use of most physical beneficiation techniques such as spiral concentrators and electrostatic separators.

(ii) **Simulation of the carbothermic reduction process of the furnace dust**

The FactSage simulations revealed the thermodynamic potential of obtaining both a titania slag

and a metallic iron from the furnace dust. The equivalent titanium dioxide content of more than 85wt% was observed at temperatures between 1650˚C and 1700˚C and at relatively high carbon additions (from the Ore-C ratio of 8.7 and below). However, such strongly reducing conditions coincided with a significant loss of the oxides of titanium from the slag phase due to deportment of titanium into the metallic phase. The impurity oxides were not significantly reduced from the slag phase even under such strongly reducing conditions. On the other hand, the more than 90wt% degree of iron metallization was achieved at lower carbon additions (Ore-C ratio of 11) with less titanium loss from the slag phase. The simulation work further showed that the extent of reduction of FeO from the slag phase was mainly influenced by the amount of a reductant, but less by the operating temperature.

(iii) **Potential of experimentally producing a titania slag and a metallic iron from the furnace dust**

The experimental reduction tests further evidenced the potential of obtaining a titania slag and a metallic iron from the furnace dust. The impurity oxides existed as separate silicate phases within the bulk slag structure and their fraction in those silicate phases remained around 90wt%. The achievable equivalent titanium dioxide content of the slag samples that were produced at 1650˚C increased from 70.87wt% at the reduction time of 2 minutes to 76.87wt% at the reduction time of 4 minutes. Such content of the equivalent titanium dioxide remained invariably around 95wt% from the reduction time of 4 minutes to 10 minutes and it was slightly lower than the 79.06wt% that was calculated by FactSage® 6.4.

A slag sample that was produced at 1600˚C for 10 minutes had a relatively lower equivalent titanium dioxide content of 72.65wt%. A further low equivalent titanium dioxide content of 65.87wt% was observed for a slag sample that was produced at 1500˚C for 10 minutes. Such decrease of the equivalent titanium dioxide content with decreasing temperature was attributed to a relatively lower effectiveness of removing the impurity oxides and a further insignificant reduction of iron oxides at 1500˚C as the slag was partially molten. The feasible temperature for the reductive smelting of the furnace dust was therefore found to be 1600˚C and 1650˚C and such temperatures fell within the 1600-1700˚C temperature range that is recommended for the production of titania slags.

The metallic iron samples that were produced along with such slag samples consisted of invariably two phases namely the major iron-rich phases and minor inclusions of the possible oxycarbide phases. The Fe content of such iron-rich phases ranged within 95.61-97.13wt% during the first 8 minutes of reduction at 1650˚C. However, a decrease of the Fe content to 93.96wt% was observed after a reduction time of 10 minutes and such Fe content approached the FactSage-calculated value of 93.09wt%. The iron-rich phases within a metallic iron sample that was produced at 1600˚C for 10 minutes further exhibited the Fe content of 93.03wt%. Such Fe content was also comparable with the FactSage-calculated content of 92.65wt% Fe, but slightly lower than the Fe content that was observed within a sample that was produced at 1650˚C. The slightly lower content of Fe at 1600˚C than at 1650˚C was attributed to a relatively higher deportment of Cr and Mn into the metallic phase at 1600˚C. The metallic iron sample that was produced at 1500˚C for 10 minutes had the Fe content of 98.47wt%, which was significantly higher than the FactSage-calculated content of 91.15wt% Fe. Such high content of Fe at 1500˚C was attributed to the dominant preferential reduction of FeO to Fe in the molten region of the partially molten slag.

An incorporation of this furnace dust into the current industrial processes for the production of a titania slag and metallic iron was found to be twofold. Such furnace dust can serve as a sole feedstock for the production of a titania slag and a metallic iron after which the slag is further treated by hydrometallurgical processes to get an upgraded slag product. Alternatively, the furnace dust may be recycled and blended with a fresh ilmenite feed at the ilmenite-to-furnace dust mass ratio of not less than 4. Such blended feed can be charged into the electric arc furnaces to produce a titania slag with acceptable impurity levels and metallic iron.

5.2. Recommendations

In this current study, the masses and compositions of individual phases (slag and metal) were measured. Another interesting study can be to determine a combined assay of those phases in order to have a more rigorous amount of elements that report into the off-gas stream.

The high amount of the impurity oxides within the titania slag that was produced from the furnace dust made it imperative to consider means and techniques that can upgrade such slag. The potential of upgrading this titania slag through the hydrometallurgical processes, which may

be based on the proposal of Borowiec et al. (1998), can be investigated.

The compositions of the slag and metallic phases that were obtained from the recycling and blending of the furnace dust with the fresh ilmenite feed were obtained from FactSage modelling only. An experimental production of the titania slag and metallic iron from such blended feed can further be investigated.

References

Ansari, M.I. 1997. 'Fine particle processing- A difficult problem for mineral engineers', *Proceedings*: *PROF-97*, Jamshedpur: National Metallurgical Laboratory, pp 93-102.

Bale, C.W., Belisle, E., Chartrand P., Decterov, S.A., Eriksson, G., Hack, K., Jung, I.-H., Kang, Y.-B., Melancon, J., Pelton, A.D., Robelin, C. and Petersen, S. 2009. 'FactSage thermochemical sofware and databases-recent developments', *CALPHAD*: *Computer Coupling of Phase Diagrams and Thermochemistry*, Volume 33, pp 295-311.

Bale, C.W., Chartrand, P., Degterov, S.A., Eriksson, G., Hack, K., Ben Mahfoud, R., Melancon, J., Pelton, A.D. and Petersen, S. 2002. 'FactSage thermochemical sofware and databases', *Calphad*, Volume 26, pp 189-228.

Banda, W. 2001. *Pyrometallurgical recovery of cobalt from waste reverberatory furnace slag by DC plasma-arc furnace technology*, A Master's Degree dissertation in Extractive Metallurgy, University of Stellenbosch, The Republic of South Africa.

Bessinger, D. 2000. *Cooling characteristics of high titania slags*, A dissertation for the degree of Master of Science in Metallurgical Engineering, University of Pretoria, The Republic of South Africa.

Bessinger, D., Beukes, P. and Glenewinkel, R. 2007. 'Granulation of titania slag', *The 6th International Heavy Minerals Conference 'Back to Basics'*, Johannesburg: The Southern African Institute of Mining and Metallurgy, pp 159-162.

Bessinger, D., Geldenhuis, J.M.A., Pistorius, P.C., Mulaba, A. and Hearne, G. 2001. 'The decrepitation of solidified high titania slags', *Journal of Non-Crystalline Solids*, Volume 282, pp 132-142.

Bickley, R.I., Gonzalez-Carreno, T., Palmisano, L., Tilley, R.J.D. and Williams, J.M. 1997. 'Relative proportions of rutile and pseudo-brookite phases in the Fe(III)-TiO_2 system at elevated temperature', *Materials Chemistry and Physics*, Volume 51, pp 47-53.

Bondar, V.V., Lopatin, S.I. and Stolyarova, V.L. 2005. 'High-temperature thermodynamic properties of the Al_2O_3-SiO_2 system', *Inorganic Materials*, Volume 41, pp 362-369.

Borowiec, K., Grau, A.E., Gueguin, M. and Turgeon, J.F. 1998. *Method to upgrade titania slag and resulting product*, U.S. Patent 5830420, Filed November 21, 1995, Issued November 3, 1998.

Brent, A.D. 1987. *The smelting of ilmenite in a DC transferred-arc plasma furnace with a molten-anode configuration*: *Report No.M304*, Randburg: The Council for Mineral Technology.

Chernet, T. 1999. 'Applied mineralogical studies on Australian sand ilmenite concentrate with special reference to its behaviour in the sulphate process', *Minerals Engineering*, Volume 12, pp 485-495.

Cong, X.U., Zhangfu, Y. and Xiaoqiang, W. 2006. 'Preparation of $TiCl_4$ with titania slag containing magnesia and calcia in a combined fluidised bed', *Chinese Journal of Chemical Engineering*, Volume 14, pp 281- 288.

Cyr, M., Carles-Gibsergues, A. and Tagnit-Hamou, A. 2000. 'Titanium fume and ilmenite fines characterization for their use in cement-based materials', *Cement and Concrete Research*, Volume 30, pp 1097-1104.

Darken, L.S. and Gurry, R.W. 1945. 'The system iron-oxygen. I. The wustite field and related equilibria', *Journal of the American Chemical Society*, Volume 67, pp 1398-1412.

de Jong, A. and Mitchell, D. 2010. 'New TiO_2 slag plant for CYMCO using 30MW DC furnace', *The Twelfth International Ferroalloys Congress*: *Sustainable Future*, Helsinki: Engineering Aspects, pp 749-758.

Dong, H., Jiang, T., Guo, Y., Chen, J. and Fan, X. 2012. 'Upgrading a Ti-slag by a roast leach process', *Hydrometallurgy*, Volume 113-114, pp 119-121.

Elstad, H., Eriksen, J.M., Hildal, A., Rosenqvist, T. and Seim, S. 2007. 'Equilibrium between titania slags and metallic iron', *The 6th International Heavy Minerals Conference 'Back to Basics'*, Johannesburg: The Southern African Institute of Mining and Metallurgy, pp 35-42.

Force, E.R. 1991. *Geology of titanium-mineral deposits*, The Geological Society of America, Boulder.

Fourie, D.J., Eksteen, J.J. and Zietsman, J.H. 2005. 'Calculation of FeO-TiO_2-Ti_2O_3liquidus isotherms pertaining to high titania slags', *The Journal of The South African Institute of Mining and Metallurgy*, Volume 105, pp 695-710.

Francis, A.A. and El-Midany, A.A. 2008. 'An assessment of the carbothermic reduction of ilmenite ore by statistical design', *Journal of Materials Processing Technology*, Volume 199, pp 279-186.

Galgali, R.K., Ray, H.S. and Chakrabarti, A.K. 1998. 'A study on carbothermic reduction of ilmenite ore in a plasma reactor', *Metallurgical and Materials Transactions B*, Volume 29B, pp 1175-1180.

Gazquez, M.J., Bolivar, J.P., Garcia-Tenorio, R. and Vaca, F. 2014. 'A review of the production cycle of titanium dioxide pigment', *Materials Sciences and Applications*, Volume 5, pp 441-458.

Gomes, J.M., Reno, N. and Uchida, K. 1974. *Process for smelting ilmenite to produce pig iron and titania-containing slag*. U.S. Patent 3829309, Filed June 6, 1972, Issued August 13, 1974.

Gottschling, R. 2009. 'Theisen gas cleaning systems', *A South African Institute of Mining and Metallurgy Seminar presented at University of Pretoria*, Pretoria: The South African Institute of Mining and Metallurgy.

Gou, H.P., Guo, H.S. and Kuo, C.C. 2015. 'Phase evolution during the carbothermic reduction process of ilmenite concentrate', *Metallurgical and Materials Transactions B*, Volume 46B, pp 48-56.

Gous, M. 2006. 'An overview of the Namakwa Sands ilmenite smelting operations', *The Journal of The South African Institute of Mining and Metallurgy*, pp 379-384.

Gueguin, M. and Cardarelli, F. 2007. 'Chemistry and mineralogy of titania-rich slags. Part 1-Hemo-ilmenite, sulphate and upgraded titania slags', *Mineral Processing and Extractive Metallurgy Review*, Volume 28, pp 1-58.

Habashi, F. 2012. 'A review. Pollution problems of the metallurgical idustry', *Rev. del Instituto de Investigacion (RIIGEO), FIGMMG-UNMSM*, Volume 15, pp 49-60.

Jones, R.T., Curr, T.R. and Barcza, N.A. 1993. *Developments in plasma furnace technology, Mintek Paper No. 8229*, London: A paper submitted for publication in The Transactions of The Institution of Mining and Metallurgy.

Keene, B.J. 1995. 'Surface tension of slag systems', in V. D. Eisenhuttenleute (ed) *Slag Atlas, 2nd Edition*. Verlag Stahleisen GmbH, D-Dusseldorf, pp 403-462.

Koroznikova, L., Klutke, C., McKnight, S. and Hall, S. 2008. 'The use of low-toxic heavy suspensions in mineral sands evaluation and zircon fractionation', *The Journal of The Southern African Institute of Mining and Metallurgy*, Volume 108, pp 25-33.

Kotźe, H., Bessinger, D. and Beukes, J. 2006. 'Ilmenite smelting at Ticor SA', *Southern African Pyrometallurgy 2006 International Conference*, Johannesburg: South African Institute of Mining and Metallurgy, pp 203-214.

Kudryavskii, Y.P. 2004. 'Physicochemical principles and technology of processing and neutralization of titanium production wastes', *Russian Journal of Applied Chemistry*, Volume 77, pp 701-707.

Lasheen, T.A. 2008. 'Soda ash roasting of titania slag product from Rosetta ilmenite', *Hydrometallurgy*, Volume 93, pp 124-128.

Lee, H. G. 1999. *Chemical thermodynamics for metals and materials*, Imperial College Press and World Scientific Publishing Co. Pte. Ltd, London.

Littler, A. 1986. 'Automatic hindered-settling classifier for hydraulic sizing and mineral beneficiation', *Transactions of the Institution of Mining and Metallurgy*, Volume 95, pp C133-C138.

Muller, J. and Erwee, M. 2011. 'Blast furnace control using slag viscosities and liquidus temperatures with phase equilibria calculations', *Southern African Pyrometallurgy 2011*, Johannesburg: Southern African Institute of Mining and Metallurgy, pp 309-326.

Namakwa Sands. 2003. 'Namakwa Footprint 2003', in *Namakwa final 2003-Anglo American*, Accessed on 26 March 2015 from www.angloamerican.com/~/media/Files/A/.../br_2003-12-31f.pdf.

Park, J.W., Ahn, J.C., Song, H., Park, K., Shin, H. and Ahn, J.S. 2002. 'Reduction characteristics of oily hot rolling mill sludge by direct reduced iron method', *Resources, Conservation and Recycling*, Volume 34, pp 129-140.

Perry, H.R., Green, D.W. and Maloney, J.O. 1997. *Perry's Chemical Engineer's Handbook, 7th Edition*, The McGraw-Hill Companies, Inc, New York.

Pesl, J. 1997. *Thermodynamics and phase equilibrium in the* Fe-Ti-O *system at 1500˚C and 1600˚C and metal-slag-equilibria pertinent to ilmenite smelting*, A dissertation for the degree of Doctor of Philosophy, University of Witwatersrand, The Republic of South Africa.

Pesl, J. and Eric, R.H. 1999. 'High-temperature phase relations and thermodynamics in the iron-titanium-oxygen system', *Metallurgical and Materials Transactions B*, Volume 30B, pp 695-705.

Pesl, J. and Eric, R.H. 2002. 'High temperature carbothermic reduction of Fe_2O_3-TiO_2-M_xO_y oxide mixtures', *Minerals Engineering*, Volume 15, pp 971-984.

Pistorius, P.C. 2002. 'The relationship between FeO and Ti_2O_3 in ilmenite smelter slags', *Scandinavian Journal of Metallurgy*, Volume 31, pp 120-125.

Pistorius, P.C. 2003. 'Fundamentals of freeze lining behaviour in ilmenite smelting', *The Journal of The Southern African Instite of Mining and Metallurgy*, pp 509-514.

Pistorius, P.C. 2004. 'Equilibrium interactions between freeze lining and slag in ilmenite smelting', *VII International Conference on Molten Slags, Fluxes and Salts*, Cape Town: The South African Institute of Mining and Metallurgy, pp 237-242.

Pistorius, P.C. 2008. 'Ilmenite smelting: the basics', *The Journal of The Southern African Institute of Mining and Metallurgy*, Volume 108, pp 35-43.

Pistorius, P.C. and Coetzee, C. 2003. 'Physicochemical aspects of titanium slag production and solidification', *Metallurgical and Materials Transactions B*, Volume 34B, pp 581-588.

Pistorius, P.C., de Villiers, J.P.R., Grasser, P. and Venter, A. 2011. 'Partial slag solidification within ilmenite smelter', *Mineral Processing and Extractive Metallurgy (Trans. Inst. Min Metall. C)*, Volume 120, pp 211-217.

Rhodes, M. 2008. *Introduction to particle technology*, *2nd Edition*, John Wiley & Sons Ltd, Chichester.

Rughubir, N. and Bessinger, D. 2007. 'Furnace dust from Exxaro Sands KZN' *The 6th International Heavy Minerals Conference 'Back to Basics'*, Johannesburg: The Southern African Institute of Mining and Metallurgy, pp 43-48.

Samal, S., Mukherjee, P.S. and Mukherjee, T.K. 2010. 'Thermal plasma processing of ilmenite: a review', *Mineral Processing and Extracitve Metallurgy (Trans. Inst. Min Metall. C)*, Volume 000, pp 1-10.

Schubert, E.S. and Gottschling, R. 2011. 'Co-generation: A challenge for furnace off-gas cleaning systems', *South African Pyrometallurgy 2011*, Johannesburg: Southern African Institute of Mining and Metallurgy, pp 145-160.

Seim, S. and Kolbeinsen, L. 2009. 'Alternative approaches for high temperature investigation of high titania slags', *The 7th International Heavy Minerals Conference 'What next'*, Johannesburg: The Southern African Institute of mining and Metallurgy, pp 57-62.

Sivamohan, R. 1990. 'The problem of recovering very fine particles in mineral processing- a review', *International Journal of Mineral Processing*, Volume 28, pp 247-288.

Sommerville, I.D. and Bell, H.B. 1982. 'The behaviour of titania in metallurgical slags', *Canadian Metallurgical Quarterly*, Volume 21, pp 145-155.

Stadler, J.G. 2012. *Multi-objective optimisation using the cross-entropy method in* CO *gas management at a South African ilmenite smelter*, A Master's Degree dissertation in Extractive Metallurgical Enineering, Stellenbosch University, The Republic of South Africa.

Steenkamp, J.D. 2003. *Beneficiation of an ilmenite waste stream containing undesirable levels of chromite*, A Mster's Degree dissertation in Engineering, University of Pretoria, The Republic of South Africa.

Sunde, M. 2012. *Organic binder as a substitute for bentonite in ilmenite pelletization*, A project related to ROMA and Gasferrosil research projects, Norwegian University of Science and Technology, Tyssedal.

Thyse, E.L., Eksteen, J.J., Bepswa, P. and Deglon, D.A. 2007. 'An integrated mineral processing pilot plant practical programme designed for heavy mineral sands beneficiation', *The 6th International Heavy Minerals Conference 'Back to Basics'*, Johannesburg: The Southern African Institute of Mining and Metallurgy, pp 105-110.

Tronox. 2011. 'Exxaro Mineral Sands acquisition', in *Tronox and Exxaro Mineral Sands*, Accessed on 27 March 2015, from www.exxaro.com/pdf/2011/October/Oct_Investor_Pres_06112011.pdf.

Walklate, J.R. and Jeram, H. 2007. 'The development of a metallurgical flowsheet to treat tails', *The 6th International Heavy Minerals Conference 'Back to Basics'*, Johannesburg: The Southern African Institute of Mining and Metallurgy, pp 91-98.

Welham, N.J. and Williams, J.S. 1999. 'Carbothermic reduction of ilmenite ($FeTiO_3$) and rutile (TiO_2)', *Metallurgical and Materials Transactions B*, Volume 30B, pp 1075-1081.

Wills, B.A. 2006. *Mineral processing technology-An introduction to the practical aspects of ore treatment and mineral recovery*, *7th Edition*, Elsevier Science & Technology Books, Queensland.

Woollacott, L.C. and Eric, R.H. 1994. *Mineral and metal extration*: *An overview*, The South African Institute of Mining and Metallurgy, Johannesburg.

Zietsman, J.H. 2004. *Interactions between freeze lining and slag bath in ilmenite smelting*, Philosophiae Doctor dissertation in Metallurgical Engineering, University of Pretoria, The Republic of South Africa.

Zietsman, J.H. and Pistorius, P.C. 2004. 'Process mechanisms in ilmenite smelting', *The Journal of The South African Institute of Mining and Metallurgy*, pp 653-660.

Appendix

Appendix A: Characteristics of materials

Table A.1: An experimental data for the analysis of particle size distribution within anthracite.

Nominal aperture (mm)	Size class (mm)	Mass retained (g)	Wt% retained	Cumulative passing (wt%)
2.000	+2.000	0.01	0.01	99.99
1.700	1.700-2.000	0.14	0.15	99.84
1.400	1.400-1.700	5.83	6.15	93.69
1.180	1.180-1.400	15.97	16.85	76.84
1.000	1.000-1.180	10.45	11.03	65.81
0.850	0.850-1.000	7.09	7.48	58.33
0.710	0.710-0.850	6.99	7.38	50.95
0.600	0.600-0.710	6.57	6.93	44.02
0.500	0.500-0.600	5.58	5.89	38.13
0.425	0.425-0.500	4.53	4.78	33.35
0.355	0.355-0.425	5.09	5.37	27.98
0.300	0.300-0.355	2.23	2.35	25.63
0.250	0.250-0.300	5.46	5.76	19.87
0.212	0.212-0.250	1.72	1.81	18.05
0.150	0.150-0.212	5.35	5.65	12.41
0.000	0.000-0.150	11.76	12.41	0.00
Total		94.77	100.00	-

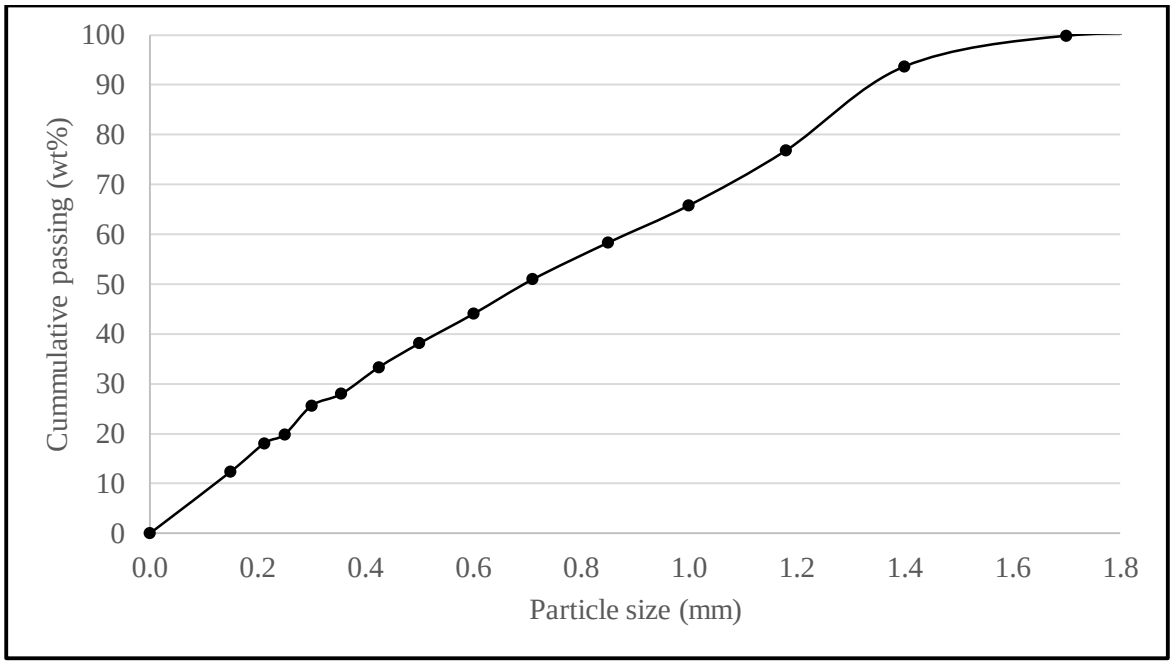

Figure A.1: A size distribution of a population of particles within anthracite.

Table A.2: The characteristics of anthracite that was used in this study.

Proximate analysis		CHN analysis	
Analyte	wt%, air dry basis	Analyte	wt%, air dry basis
Moisture content	2.88	N	2.05
Volatile matter	9.85	H	3.16
Ash content	12.30	C	77.82
Fixed carbon	74.95	-	-

Table A.3: An experimental data for the analysis of particle size distribution within the furnace dust.

Particle diameter (µm)	Size class	Nominal size- d	Frequency (wt%)- f	Cumulative undersize (wt%)	$\left(\frac{f}{100}\right) \times$ d
250.00	+250.00	-	0.68	99.32	-
200.00	200.00-250.00	225.00	4.14	95.19	9.31
150.00	150.00-200.00	175.00	7.25	87.94	12.69
100.00	100.00-150.00	125.00	8.51	79.43	10.63
90.00	90.00-100.00	95.00	2.14	77.30	2.03
80.00	80.00-90.00	85.00	2.51	74.78	2.14
70.00	70.00-80.00	75.00	2.99	71.80	2.24
60.00	60.00-70.00	65.00	3.47	68.33	2.26
50.00	50.00-60.00	55.00	3.89	64.44	2.14
40.00	40.00-50.00	45.00	4.35	60.09	1.96
30.00	30.00-40.00	35.00	5.38	54.70	1.88
25.00	25.00-30.00	27.50	3.33	51.37	0.92
20.00	20.00-25.00	22.50	3.65	47.73	0.82
10.00	10.00-20.00	15.00	9.70	38.03	1.45
9.00	9.00-10.00	9.50	1.10	36.93	0.10
8.00	8.00-9.00	8.50	0.89	36.04	0.08
7.00	7.00-8.00	7.50	0.80	35.23	0.06
6.00	6.00-7.00	6.50	0.99	34.24	0.06
5.00	5.00-6.00	5.50	1.37	32.87	0.08
4.00	4.00-5.00	4.50	1.68	31.19	0.08
3.00	3.00-4.00	3.50	1.79	29.40	0.06
2.00	2.00-3.00	2.50	2.19	27.22	0.05
1.00	1.00-2.00	1.50	4.93	22.29	0.07

Continuation of **Table A.3**: An experimental data for the analysis of particle size distribution within the furnace dust.

0.90	0.90-1.00	0.95	0.88	21.41	0.01
0.80	0.80-0.90	0.85	1.10	20.31	0.01
0.70	0.70-0.80	0.75	1.42	18.89	0.01
0.60	0.60-0.70	0.65	1.84	17.06	0.01
0.50	0.50-0.60	0.55	2.26	14.80	0.01
0.40	0.40-0.50	0.45	2.58	12.22	0.01
0.30	0.30-0.40	0.35	2.80	9.42	0.01
0.20	0.20-0.30	0.25	3.55	5.87	0.01
0.10	0.10-0.20	0.15	5.11	0.76	0.01
0.00	0.00-1.00	0.05	0.76	0.00	0.00
Total			100.00		51.20

Appendix B: Reduction test work

(a) Furnace preparation

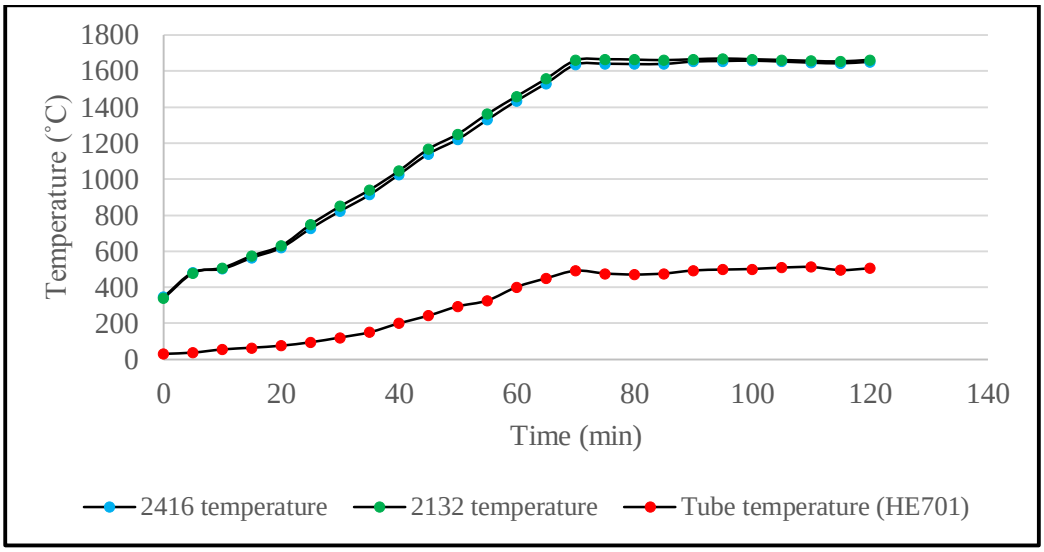

Figure A.2: An initial performance of the vertical tube furnace showing the maximum temperature of 500˚C when the 2416 and the 2132 controllers were set at 1650˚C and 1665˚C respectively.

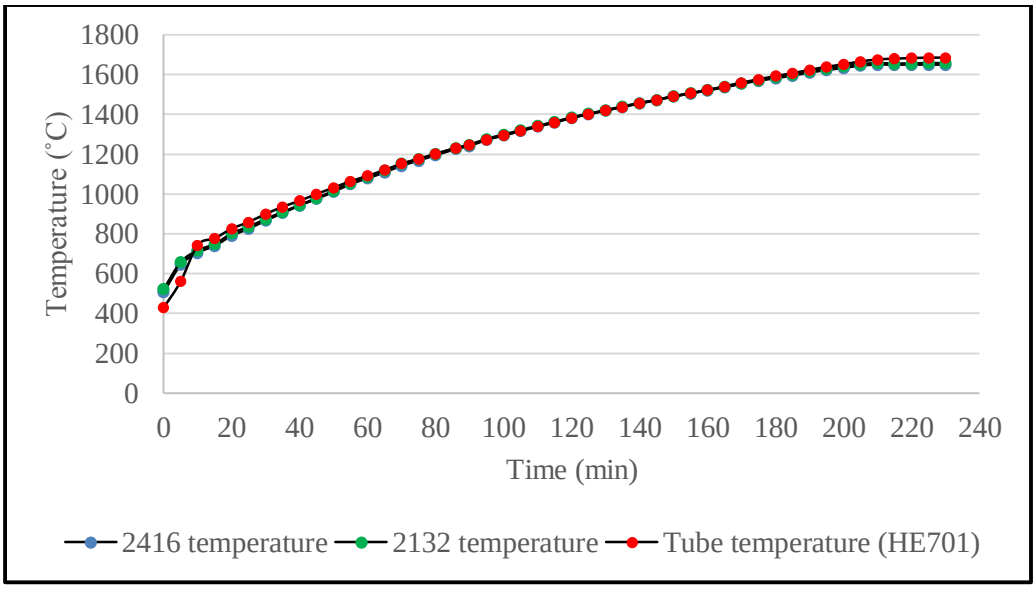

Figure A.3: The performance of the vertical tube furnace after calibration. The 2416 controller was set at 1650˚C while the 2132 controller was set at 1665˚C. The external thermocouple (TC-1) was located at approximately 500 mm from the furnace top.

A slight difference of temperature readings from the external thermocouple (TC-1) and the 2416 controller was identified when the furnace was heating up. For this reason, the hot zone was located with the use of two more R-type thermocouples, which are referred to as TC-2 and TC-3 for the sake of distinction. This hot zone was located after 20 min when the 2416 controller had attained a temperature of 1650˚C. A set-up in Figure A.4 was established in order to measure the voltage across these thermocouples because the cables of the TC-2 and TC-3 thermocouples did not have a mini plug that could fit into the HE701 thermometer.

Figure A.4: A set-up for determination of the hot zone within the alumina tube.

The cable ends of the thermocouples were connected to the HP 3466A digital multimeter. The multimeter was subsequently adjusted to measure the voltage in millivolts. The radiation shield was removed from the furnace top and the thermocouples were traversed from the top of the

furnace at different positions while recording the voltage across such thermocouples. Due to safety purposes, it was not possible to lower the thermocouples to a depth of more than 600 mm. The voltage readings were subsequently converted to temperature by using the National Institute of Standards and Technology (N.I.S.T.) thermocouple reference tables for R-type thermocouples. The results are presented in Table A.4.

Table A.4: The measured voltages and corresponding temperature readings during the determination of the hot zone within the alumina tube. Temp. refers to temperature.

Distance from the furnace top (mm)	TC-1		TC-2		TC-3		Average temp.(˚C)
	Voltage (mV)	Temp. (˚C)	Voltage (mV)	Temp. (˚C)	Voltage (mV)	Temp. (˚C)	
200	11.345	1063	9.041	887	8.927	878	944
300	16.684	1446	15.960	1394	16.296	1418	1419
400	19.658	1659	18.692	1589	19.302	1633	1627
500	19.900	1676	19.123	1620	19.883	1671	1656
550	19.900	1676	18.973	1609	19.837	1672	1652
600	19.900	1676	18.873	1602	19.511	1648	1642

(b) Simulation modelling

i. Calculations of the amounts of reactants.

From the chemical composition of the furnace dust in Table 4.1, it was found that 0.31wt% of this material was lost on ignition at 1000˚C and 0.16wt% was carbon, which would contribute to carbothermic reduction. Therefore, 99.53wt% of the dry furnace dust was considered to be available for reduction. By letting the total mass of dry furnace dust to be M_D, the mass fraction of carbon in the dry furnace dust to be c = 0.0016, the mass of additional carbon to be M_C and the mass of dry furnace dust when omitting the loss on ignition and carbon to be M_O, the following equations were established.

$$M_D + M_C = 20 \text{ g} \quad \text{..... (A.1)}$$

$$M_O = 0.9953 M_D \quad \text{..... (A.2)}$$

For the Ore-C ratio of 14.8 in Table 3.1, it follows that

$$M_O = 14.8(M_c + cM_D) \quad \text{..... (A.3)}$$

From substitution and rearrangement of these equations, it follows that

$$M_D = \frac{20(14.8)}{14.8+0.9953-(14.8\times0.0016)}\ \text{g} = \underline{18.768\ \text{g}}$$

$$M_C = \underline{1.232\ \text{g}}$$

And $M_O = \underline{18.680\ \text{g}}$

The mass of each chemical species was determined by multiplying the relative abundance of such species with M_D. The total amount of carbon was the sum of M_c and carbon that was identified within the furnace dust. The amounts of chemical species at different Ore-C ratios were calculated in the similar manner.

ii. Calculations pertaining to the equivalent titanium dioxide and the degree of iron metallization

$$\text{wt\% } Ti^{total} \text{ (in slag)} = \left(\frac{MW\ Ti}{MW\ TiO_2} \times \text{wt\%} TiO_2\right) + \left(\frac{2 \times MW\ Ti}{MW\ Ti_2O_3} \times \text{wt\% } Ti_2O_3\right) + (Fraction\ of\ Ti\ in\ M_3O_5 \times \text{wt\% } M_3O_5 \quad \text{..... (A.4)}$$

$$\text{wt\% } {TiO_2}^{eq} = \frac{MW\ TiO_2}{MW\ Ti} \times \text{wt\% } Ti^{total} \quad \text{..... (A.5)}$$

MW denotes molecular weight. The calculation of the degree of iron metallization was achieved with the use of Equation 1.4.

(c) Experimental reduction tests

i. Preliminary observations

The masses of the furnace products that were obtained at different runs are presented in Table A.5 and a depiction of some of such data is in Figure A.5. It may be noted that the mass of a slag at time = 0 min corresponded to the mass of the furnace dust (exclusive of the loss on ignition) and carbon.

It was observed that the decrease of the mass of the slag and the corresponding increase of the mass of metallic phase occurred quickly within the first 2 minutes of reduction. The masses of such two phases gradually decreased and increased respectively after 2 minutes until no

significant change in mass was observed after the reduction time of 6 minutes.

Table A.5: The masses of the furnace products that were obtained at different experimental runs.

Reduction time (min)	Temperature (˚C)	Metal (g)	Slag (g)
0	0	0	20
2	1650	2.53	11.36
4	1650	2.90	10.06
6	1650	3.07	9.78
8	1650	3.00	9.86
10	1650	3.01	10.11
10	1600	3.00	9.92
10	1500	1.70	13.28

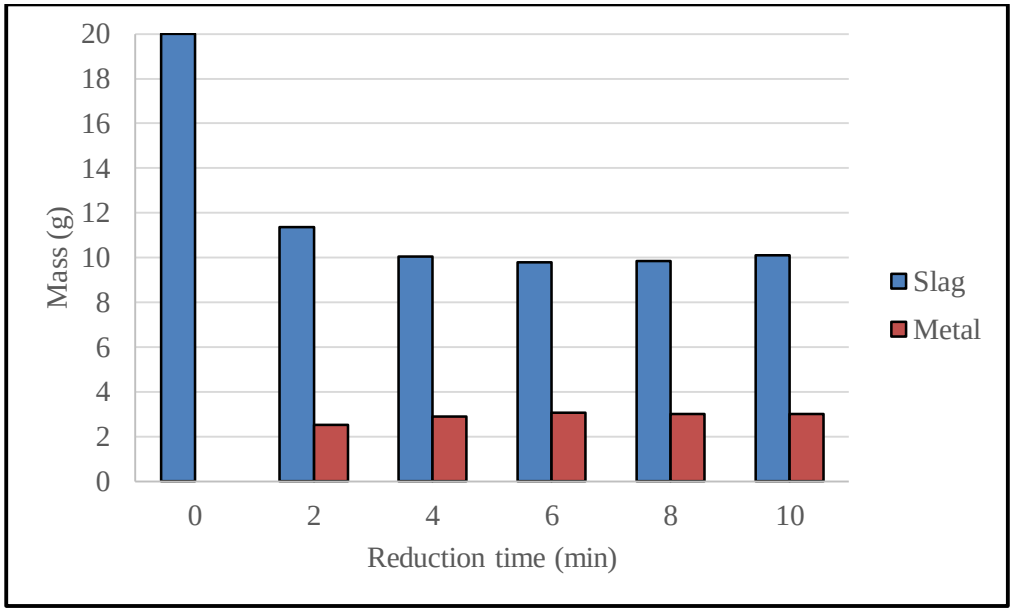

Figure A.5: The change of masses of the furnace products with reduction time at 1650˚C.

ii. Calculation of the oxide abundances from the SEM-EDS data

The SEM-EDS technique did not distinguish the oxidation states of titanium, but it reported out the total weight percent of such titanium. As such, the molar balance of Ti^{4+} and Ti^{3+} were achieved by using Equations A.6 and A.7. The symbols of the chemical elements represent the

abundance, in weight percent, of such elements as determined by the SEM-EDS.

$$\text{wt\%}Ti^{4+} = \left(\frac{MW_{Ti}}{2}\right)\left[\frac{O}{16.00} - \left(\frac{0.5Na}{22.99} + \frac{Mg}{24.31} + \frac{1.5Al}{26.98} + \frac{2Si}{28.09} + \frac{2.5P}{30.97} + \frac{0.5K}{39.10} + \frac{Ca}{40.08} + \frac{1.5Cr}{52.00} + \frac{Mn}{54.94} + \frac{Fe}{55.85} + \frac{Zn}{65.39} + \frac{1.5Ti}{47.87}\right)\right] \text{..... (A.6)}$$

$$\text{wt\%}Ti^{3+} = Ti - \text{wt\%}\,Ti^{4+} \text{ .... (A.7)}$$

The abundances of the different oxidation states of titanium and the abundances of other elements were subsequently converted to respective oxides abundances with the use of Equation A.8, where M denotes a cation.

$$\text{wt\%}\,MO_x = \left(\frac{MW_{MO_x}}{MW_M}\right)(\text{wt\%}\,M) \text{ ..... (A.8)}$$

iii. Raw data for the bulk composition of slag samples

The bulk composition of most slag samples was accomplished by both the XRF and the SEM-EDS techniques. An exception was in the case of the **S6** and **S7** samples where the fused beads of such samples consistently cracked after preparation. Only the SEM-EDS data was used for such samples.

The raw data from such analyses is summarized in Table A.6 and it can be seen that both the XRF and the SEM-EDS techniques delivered comparable results for the slag samples except sometimes in the case of FeO. The XRF technique sometimes provided significantly more FeO content than the SEM-EDS technique and this was attributed to the particles of the metal globules that were occluded within the slag phase. The actual abundance of FeO within the slag samples was therefore considered as that determined by the SEM-EDS technique because the areal analysis was done with exclusion of such occluded metal globules.

Furthermore, alumina seemed to be relatively high within the **S1** and **S3** samples and these high abundances underestimated the abundances of other oxides including the total oxides of titanium. The source of such alumina was ultimately identified as the gas outlet ceramic pipe of the vertical tube furnace. Such pipe was submerged within the crucible during an initial placement of

Table A.6: A raw data for the bulk composition of slag samples, in weight percent, as determined by the SEM-EDS and XRF techniques.

Sample tag	Analytical technique	Al_2O_3	CaO	Cr_2O_3	FeO	K_2O	MgO	MnO	Na_2O	P_2O_5	SiO_2	$TiO_2{}^{total}$	Total
S1	XRF	30.62	0.20	0.09	4.81	1.22	0.64	2.62	0.27	0.01	9.84	44.06	94.38
	SEM-EDS	27.15	0.21	0.02	4.32	1.13	0.95	3.30	0.03	0.00	10.93	43.60	91.62
S2	XRF	2.11	0.24	0.10	12.53	1.30	0.95	3.18	0.26	0.10	11.37	59.90	92.04
	SEM-EDS	2.45	0.28	0.13	1.72	1.19	1.24	4.56	0.00	0.00	14.20	65.39	91.17
S3	XRF	25.48	0.21	0.11	9.29	1.04	0.68	2.62	0.20	0.06	10.04	44.47	94.20
	SEM-EDS	27.01	0.25	0.00	1.71	1.10	0.97	3.01	0.00	0.00	10.88	46.18	91.12
S4	XRF	2.47	0.22	0.10	11.31	1.82	0.97	3.32	0.38	0.06	12.49	61.14	94.28
	SEM-EDS	4.23	0.33	0.06	1.18	3.43	1.48	5.43	1.01	0.00	11.30	62.90	91.35
S5	XRF	2.40	0.25	0.10	7.41	1.97	1.01	3.68	0.38	0.03	12.81	65.37	95.41
	SEM-EDS	2.73	0.29	0.09	2.63	2.44	1.31	5.21	0.72	0.00	10.98	66.39	92.75
S6	SEM-EDS	2.56	0.20	0.06	1.93	2.06	1.21	4.98	0.58	0.00	17.53	68.90	100.02
S7	SEM-EDS	2.37	0.16	0.18	10.68	1.80	0.97	4.28	0.69	0.00	16.13	62.77	100.02

a sample into the hot zone and hence a dissolution of some alumina into the slag sample. In some instances, the weakened pipe broke due to thermal shock and such breakage caused some alumina debris to fall into a crucible. This was more likely for the **S3** sample and for other samples in which such contamination was not significant. An image of such gas outlet ceramic pipe after being attacked by the titania slag is shown in Figure A.6.

Figure A.6: Images of the gas outlet ceramic pipe showing the tip that was attacked by the titania slag.

The raw bulk composition of the slag samples was therefore reconciled by the following summarized procedure and such bulk compositions are included in Table 4.3 to Table 4.9.

- The raw data in Table A.6 was averaged for each slag sample where both the SEM-EDS and the XRF technique were used.
- From such averaged data, the abundances of the oxides of trivalent and tetravalent titanium were estimated from the total titanium with the use of Equation A.7 and the $\frac{Ti^{3+}}{Ti^{4+}}$ ratio, which was found from the analysis of the Ti-rich and silicate phases, to remain invariably around 3.01.
- The abundance of alumina within the furnace dust (cf. Table 4.1) was taken into account and it was reconciled for the **S1** and **S3** samples. Such reconciliation was done with an assumption that alumina that was present within the furnace dust was not significantly removed from the slag phase during the reductive smelting process.
- The abundances of oxides within each slag sample were finally normalized to 100wt% in order to give the bulk compositions.